INTEGRATING INFLAMMATORY STIMULI WITH MACROMOLECULES FOR THERAPY AND SENSING OF VASCULAR DISEASES

BY

EUNICE LEONG JIAYU

DISSERTATION

Submitted in partial fulfillment of the requirements
for the degree of Doctor of Philosophy in Chemical Engineering
in the Graduate College of the
University of Illinois at Urbana-Champaign, 2018

Urbana, Illinois

Doctoral Committee:

Professor Hyunjoon Kong, Chair
Dr. Yi Yan Yang, Institute of Bioengineering and Nanotechnology, Singapore
Professor Charles Schroeder
Associate Professor Marni Boppart

ABSTRACT

Inflammation is a beneficial component for healing under normal homeostasis. However, excessive inflammation can also aggravate the patient's condition. Biochemical signals elicited under inflammatory conditions are considerably different from those under normal circumstances. Molecules such as pro-inflammatory mediator TNFα and reactive oxygen species are powerful triggers to several signaling mechanisms. In this regard, the overall goal of my research is to integrate inflammatory stimuli TNFα and ROS with macromolecules for therapy and sensing of vascular diseases. To do so, specific features of nanoparticles were studied in Chapter 2 to engineer solutions for the prevailing problems in ischemia and cancer. This thesis presents three approaches in investigating the combination of these potent inflammatory molecules with nanotechnology: (1) TNF-α-releasing liposomes were tethered on the surface of adipose-derived stem cells to enhance their secretory activities (Chapter 3). (2) Thioether-groups were incorporated into micelle-forming polymers to induce a reactive oxygen species-responsive drug release and swelling effect (Chapter 4). (3) Oxidizable chromophores were adsorbed onto support microparticles to form a hydrogen peroxide-sensing patch (Chapter 5). Overall, the results from these studies contribute to a deeper understanding of how to utilize disease biomolecules in the design of novel diagnostics and therapeutics.

ACKNOWLEDGEMENTS

Professor Hyunjoon Kong and Dr. Yi Yan Yang, thank you for having faith and supporting me as my research advisors. Thank you for all the opportunities to learn and your patience in guiding me along the way.

My thesis committee members, Professor Hong Yang during my preliminary examination, Professor Charles Schroeder during my final defense examination, for your thoughtful contributions and I am appreciative for your interests and time taken to recommend areas for improvements. Special mention to Professor Marni Boppart, who patiently provided valuable insights on muscle physiology.

Collaborators from South Korea, Korea Institute of Science and Technology, Dr. Hojeong Jeon and Dr. Kyeongsoo Kim and Yonsei University, Prof. Seung-Woo Cho and Eun Je Jeon. Collaborators in the United States, NASA, Dr. Cheol Park and Dr. Sang-Hyon Chu, and IBM, Dr. James Hedrick. Collaborators at UIUC, Yu-Fu Wu, Svyatoslav Dvoretskiy, Michael Munroe.

Life in Urbana-Champaign couldn't have been a more surprisingly stark contrast from my life in Singapore. However, the transition was smooth and pleasant because of the wonderfully supportive community. University housing provided a safe and comforting haven with the friendliest community aides and facility managers. Graduate program coordinators, who tirelessly facilitated the administrative issues with my unique AUIP program. Staff from the Division of Animal Resources, IGB Core Facilities, and MRL for the trainings and availability to come to my rescue. Professors, for your passionate efforts in imparting your knowledge through well-planned lectures and coursework. Classmates and friends, for generously sharing your notes and equipment for experiments.

My lab colleagues in both the Kong group and the Yang group. Thank you for sharing your time with me to show me techniques I didn't know but have become very useful in my work. But most importantly, your warm smiles, listening ears, and amusing stories and rants were especially precious when experiments didn't work out.

I am grateful for the financial support from the four-year scholarship by the Agency of Science, Technology and Research (A*STAR), Singapore and the continuous encouragement from my dearest family and friends in Singapore to have the courage to embrace the opportunity to live and study abroad for two and a half years at the University of Illinois, Urbana-Champaign.

Eunice Leong

July 2, 2018

TABLE OF CONTENTS

CHAPTER 1: Introduction

1.1 Inflammation

Everything in excess is opposed to nature. – Hippocrates.

Red hot and painful swellings are signs of inflammation that people associate with something bad and should be unwelcomed. However, inflammation is an important response to injury and microbial infections that calls immune molecules and cells to remove the offending species.[1] It is a natural and necessary event to eliminate cause of damage and allow the tissues to recover. Conversely, wounds would not heal and infections would be left unresolved in the absence of inflammation.

In general, inflammation is initiated by molecules produced from injured and dead cells or invaded microbes and are discharged from the tissues. Circulating leukocytes and plasma proteins consisting of antibodies and complement proteins in the blood recognize these molecules and are triggered to produce chemokines to attract more to the site of injury. Monocytes and granulocytes are activated to eliminate microbes and dead cells and ingest the unwanted materials from the site. In order for the recruitment and infiltration of immune cells to occur, surrounding tissues secrete pro-inflammatory cytokines to slow down blood flow by dilating the blood vessels and increasing the permeability of the vessel walls. Under normal circumstances, during these events, the level of chemokines are modulated to recruit only sufficient cells to resolve the problem. Thus, when the site is cleared of the offending agents, the immune cells are expected to leave the site to allow the tissues to regenerate and recover. If the engagement of immune cells were prolonged or inefficient, the injury would progress to the chronic state of inflammation. Chronic inflammation leads to non-healing wounds.

1.2 Pro-inflammatory mediator: TNFα

The role of pro-inflammatory cytokines such as tumor necrosis factor-alpha (TNFα) is to induce vasodilation and facilitate adhesion of leukocytes.[2] It also promotes repair processes in tissues.[3,4] TNFα is produced by leukocytes, endothelial cells, smooth muscle cells, fibroblasts and many more but the main producers are macrophages and T cells.

The biological effects of TNFα signaling are mediated by the binding of receptors, known as TNFR1 and TNFR2. TNFR1 is expressed on the surface of almost all human cell types except erythrocytes while TNFR2 is located mainly on immune and endothelial cells. Binding to TNFR1 activates either the cell survival or the apoptosis and cell death pathway.[5] The predominant pathway is promoted by several factors including signal strength and crosstalk with other cell signals. In the cell, TNFα signaling are mediated by mitogen-activated protein kinases which participate in the transcription and translation of numerous downstream genes to result in an inflamed environment.[6]

Higher temperature at the inflamed site is the result of vasodilation, where there is an increased blood flow to the injured site. This is to facilitate inflammatory mediators and cells to reach the inflamed tissue. TNFα promotes vasodilation by stimulating the activity of cyclooxygenase 2 to produce more prostanoids PGE_2, $PGF_{2\alpha}$, and PGI_2 that relax the blood vessel smooth muscles.[7] Another symptom of inflammation is swelling. This is caused by the higher vessel permeability to facilitate the transport of antibodies and proteins. TNFα contributes to edema by destabilizing the endothelial cell cytoskeleton and the formation of gaps at the endothelial gap junctions to open the paracellular passage of solutes and macromolecules.[8] At the same time, to increase the migration of leukocytes to the inflamed site, TNFα stimulates the

expression of adhesion molecules E- and P-selectins, intracellular adhesion molecule 1, and vascular cell adhesion molecule 1 on the endothelial surface.[9]

Besides engaging the host immune system, TNFα also function as stimuli to activate stem cells to orchestrate repair processes by secreting a large number of angiogenic growth factors and anti-apoptotic factors.[10] The increased secretion of angiogenic stem cell factors not only serves as an autocrine self-survival mechanism but also acts as a source of paracrine signaling molecules in stem cell-mediated angiogenesis and protection to improve regional blood flow.

TNFα is also a potent inducer for the production of reactive oxygen species to serve as secondary messengers to modulate downstream DNA transcription, cytokine production and cell survival.[5] It does so by increasing the expression and activity of proteins from the NADPH oxidase family or through the stimulation of respiratory bursts in polymorphonuclear leukocytes.

1.3 Reactive oxygen species (ROS)

Reactive oxygen species (ROS) are partially reduced metabolites of oxygen that possess strong oxidizing capabilities.[11] In biological systems, they function as signaling molecules that regulate cell adhesion, proliferation, differentiation, senescence and apoptosis.[12] However, these concentrations must be carefully controlled as high concentrations are deleterious to cells. They injure cells by oxidizing protein and lipid cellular constituents, and damaging DNA.

During inflammation, ROS are produced by immune cells such as polymorphonuclear neutrophils to kill pathogens. They are also produced by the injured tissues as early signals of damage to initiate redox signaling. One of the effects is in the regulating cell adhesion molecules to increase neutrophil adhesion to the endothelium and decrease leukocyte-rolling velocity.

Biologically relevant ROS are superoxide anion ($O_2^{\bullet-}$), hydroxyl radical ($OH^{\bullet}$), hydrogen peroxide (H_2O_2) and hypochlorous acid (HOCl). However, $O_2^{\bullet-}$ has a short half-life of 10 milliseconds because it undergoes spontaneous dismutation to H_2O_2. Similarly, $OH^{\bullet}$ is highly unstable and reacts within 1 to 5 molecular diameters of their site of formation.[13]

In contrast, H_2O_2 is more stable and can cross biological membranes through aquaporin channels. It can be an oxidizing agent to form more toxic oxidation products in the presence of chloride (Cl^-), bromide (Br^-), iodide (I^-) and pseudohalide thiocyanate (SCN^-). $H_2O_2 + Cl^- \rightarrow OX^- + H_2O$ ($X^- = Cl^-$, Br^-, I^- or SCN^-) where the concentrations of the halides in biological fluid are 100-140 mM Cl^-, 20-100 μM Br^-, < 1 μM I^-, 20-120 μM SCN^-.[14] This reaction is catalyzed by myeloperoxidase expressed by neutrophils, monocytes and macrophages. HOCl, the conjugate acid of OCl^-, leads to further formation of reactive nitrogen and oxygen species.

To prevent the deleterious effects by ROS, cellular antioxidant enzymes and exogenous reducing compounds function to scavenge the excess ROS. These enzymes include superoxide dismutase, catalase, glutathione peroxidase, thioredoxin reductase. For example, superoxide dismutase converts $O_2^{\bullet-}$ to H_2O_2 while catalase and glutathione peroxidase convert H_2O_2 to oxygen and water. In contrast, exogenous antioxidants include small molecules vitamin C (ascorbic acid), vitamin E (tocopherols), carotenoids, and polyphenols. Although they are commonly labeled as antioxidants, these small molecules also exhibit pro-oxidative effects at high doses, only possible through excessive dietary supplements.[15] Together, the balance between oxidative and antioxidant is essential in a healthy biological system which would otherwise lead to oxidative stress state.

Oxidative stress from the loss in control of the intracellular reactive oxygen species, has been strongly associated in diseases such as cardiovascular diseases and cancer. For example, heart failure from ischemia-reperfusion injury is a leading cause of death worldwide. At the injured

region, generation of reactive oxygen species is dramatically increased by over three-fold.[16] This posed a challenge to the approach of transplanting mesenchymal stem cells to repair and regenerate cardiomyocytes for the restoration of heart function. The transplanted mesenchymal stem cells died within a few days following implantation. This is believed to be due to the elevated ROS levels which inhibited cellular adhesion of engrafted MSCs by decreasing the level of focal adhesion-related molecules, such as phosphor-FAK and p-Src in mesenchymal stem cells.[17]

Conversely, in cancer, aggressive growth, proliferation and metastatic ability of cancer cells may be a manifestation of oncogenic mutations and dysregulations by ROS.[18] For example, H_2O_2 activates increased expression of hypoxia-inducible factor 1 to promote tumor angiogenesis and resistance to apoptosis.[19] As the slightly higher oxidative environment supported the survival of cancer cells, these cancers are believed to have gained the resistance to withstand the higher levels of ROS.[20]

While the overall molecular events in response to injury are highly complex and multifactorial, ROS such as H_2O_2 are prominent participants in inflammation. Notwithstanding that inflammation is a beneficial component for healing under normal homeostasis, excessive ROS produced during inflammation can aggravate the patient's condition or could be an underlying initiator to subsequent pathological events, thereby posing a causal effect leading to death.

1.4 Research Overview

The goal of my research is to integrate inflammatory stimuli TNFα and ROS with macromolecules for therapy and sensing of vascular diseases. The research was supported by three main projects presented in this dissertation. To support the research done, Chapter 2 is a literature review of the materials that will be presented in the subsequent chapters.

In Chapter 3, TNFα-releasing liposomes were adsorbed on the surface of adipose-derived stem cells. This placement of nanoparticles on the cell surface allowed the in situ stimulation of mesenchymal stem cells upon the cellular transplantation at the ischemic tissue. The in situ activation seeked to increase the therapeutic efficacy of transplanted mesenchymal stem cells and to reduce loss in activity during an ex vivo culture.

In Chapter 4, reactive oxygen species (ROS) – responsive drug delivery micelles was prepared for anticancer therapy. Thioether functional groups were installed on micelle-forming block copolymers. The hydrophilic and hydrophobic block lengths were controlled such that upon oxidation by ROS, the micelles swell to release the loaded drugs. This results in a more selective and potent delivery of drug in the tissue with abnormally high ROS levels.

In Chapter 5, an H_2O_2 sensor was built from a hybrid of inorganic-organic materials. Mesoporous silica particles of different diameters were used to control the chromophore oxidation by H_2O_2. The chromophore-loaded silica particle was then loaded into a hydrogel to produce the final hydrogen peroxide sensor. By utilizing the hybrid of materials, the chromophore embedded within a solid material is visible to the eye and becomes a more versatile material than a liquid-based assay.

Finally, Chapter 6 presents a summary of the main findings in Chapters 3 to 5 and suggestions for future investigations.

1.5 References

(1) Kumar, V.; Abbas, A. K.; Aster, J. C. *Robbins and Cotran Pathologic Basis of Disease*; 9th ed.; Elsevier, 2015.

(2) Zelová, H.; Hošek, J. TNF-α Signalling and Inflammation: Interactions between Old Acquaintances. *Inflammation Research*, 2013, *62*, 641–651.

(3) Kurrelmeyer, K. M.; Michael, L. H.; Baumgarten, G.; Taffet, G. E.; Peschon, J. J.; Sivasubramanian, N.; Entman, M. L.; Mann, D. L. Endogenous Tumor Necrosis Factor Protects the Adult Cardiac Myocyte against Ischemic-Induced Apoptosis in a Murine Model of Acute Myocardial Infarction. *Proc. Natl. Acad. Sci. U. S. A.* **2000**, *97*, 5456–5461.

(4) Glass, G. E.; Chan, J. K.; Freidin, A.; Feldmann, M.; Horwood, N. J.; Nanchahal, J. TNF-α Promotes Fracture Repair by Augmenting the Recruitment and Differentiation of Muscle-Derived Stromal Cells. *Proc. Natl. Acad. Sci.* **2011**, *108*, 1585–1590.

(5) Blaser, H.; Dostert, C.; Mak, T. W.; Brenner, D. TNF and ROS Crosstalk in Inflammation. *Trends Cell Biol.* **2016**, *26*, 249–261.

(6) Kwon, Y. W.; Heo, S. C.; Jeong, G. O.; Yoon, J. W.; Mo, W. M.; Lee, M. J.; Jang, I.-H.; Kwon, S. M.; Lee, J. S.; Kim, J. H. Tumor Necrosis Factor-α-Activated Mesenchymal Stem Cells Promote Endothelial Progenitor Cell Homing and Angiogenesis. *Biochim. Biophys. Acta - Mol. Basis Dis.* **2013**, *1832*, 2136–2144.

(7) Mark, K. S.; Trickler, W. J.; Miller, D. W. Tumor Necrosis Factor-Alpha Induces Cyclooxygenase-2 Expression and Prostaglandin Release in Brain Microvessel Endothelial Cells. *J. Pharmacol. Exp. Ther.* **2001**, *297*, 1051–1058.

(8) Goldblum, S. E.; Sun, W. L. Tumor Necrosis Factor-Alpha Augments Pulmonary Arterial Transendothelial Albumin Flux in Vitro. *Am. J. Physiol.* **1990**, *258*, L57–L67.

(9) Chandrasekharan, U. M.; Siemionow, M.; Unsal, M.; Yang, L.; Poptic, E.; Bohn, J.; Ozer, K.; Zhou, Z.; Howe, P. H.; Penn, M.; *et al.* Tumor Necrosis Factor α (TNF-α) Receptor-II Is Required for TNF-α-Induced Leukocyte-Endothelial Interaction in Vivo. *Blood* **2007**, *109*, 1938–1944.

(10) Kwon, Y. W.; Heo, S. C.; Jeong, G. O.; Yoon, J. W.; Mo, W. M.; Lee, M. J.; Jang, I.-H.; Kwon, S. M.; Lee, J. S.; Kim, J. H. Tumor Necrosis Factor-α-Activated Mesenchymal Stem Cells Promote Endothelial Progenitor Cell Homing and Angiogenesis. *Biochim. Biophys. Acta - Mol. Basis Dis.* **2013**, *1832*, 2136–2144.

(11) Mittal, M.; Siddiqui, M. R.; Tran, K.; Reddy, S. P.; Malik, A. B. Reactive Oxygen Species in Inflammation and Tissue Injury. *Antioxid. Redox Signal.* **2014**, *20*, 1126–1167.

(12) van der Vliet, A.; Janssen-Heininger, Y. M. W. Hydrogen Peroxide as a Damage Signal in Tissue Injury and Inflammation: Murderer, Mediator, or Messenger? *J. Cell. Biochem.* **2014**, *115*, 427–435.

(13) Pryor, W. a. Oxy-Radicals and Related Species: Their Formation, Lifetimes, and Reactions. *Annu. Rev. Physiol.* **1986**, *48*, 657–667.

(14) Babior, B. M. Phagocytes and Oxidative Stress. *Am. J. Med.* **2000**, *109*, 33–44.

(15) Bouayed, J.; Bohn, T. Exogenous Antioxidants—Double-Edged Swords in Cellular Redox

State. *Oxid. Med. Cell. Longev.* **2010**, *3*, 228–237.

(16) Angelos, M. G.; Kutala, V. K.; Torres, C. A.; He, G.; Stoner, J. D.; Mohammad, M.; Kuppusamy, P. Hypoxic Reperfusion of the Ischemic Heart and Oxygen Radical Generation. *Am. J. Physiol. Circ. Physiol.* **2006**, *290*, H341–H347.

(17) Song, H.; Cha, M. J.; Song, B. W.; Kim, I. K.; Chang, W.; Lim, S.; Choi, E. J.; Ham, O.; Lee, S. Y.; Chung, N.; *et al.* Reactive Oxygen Species Inhibit Adhesion of Mesenchymal Stem Cells Implanted into Ischemic Myocardium via Interference of Focal Adhesion Complex. *Stem Cells* **2010**, *28*, 555–563.

(18) Khandrika, L.; Kumar, B.; Koul, S.; Maroni, P.; Koul, H. K. Role of Oxidative Stress in Prostate Cancer. *Cancer Lett.* **2009**, *282*, 125–136.

(19) Qutub, A. a; Popel, A. S. Reactive Oxygen Species Regulate Hypoxia-Inducible Factor 1alpha Differentially in Cancer and Ischemia. *Mol. Cell. Biol.* **2008**, *28*, 5106–5119.

(20) Kumar, B.; Koul, S.; Khandrika, L.; Meacham, R. B.; Koul, H. K. Oxidative Stress Is Inherent in Prostate Cancer Cells and Is Required for Aggressive Phenotype. *Cancer Res.* **2008**, *68*, 1777–1785.

CHAPTER 2: Literature Review

Nanoparticles and microparticles formed from natural and synthetic macromolecules are immensely used in the development of diagnostics and therapy. The organic or inorganic building blocks contribute to three-dimensional structures with length scales in the order of less than a few micrometers. The intricate design features of these engineered particles such as the size, shape, surface activities and sensitivity to chemical stimuli play an important role in imparting novel properties and function. We reviewed the implications of these features in the design of nanoparticles for biomedical applications in *Advanced Healthcare Materials*.[1] The following subsections summarize key aspects considered for using surface-binding nanoparticles, amphiphilic micelle-forming polymers and porous materials towards building solutions to three prevailing practical problems selected for this dissertation.

2.1 Surface-binding nanoparticles – Adhesion to the cell surface

The nature of the exterior surface is a vital feature in the design of nanoparticles for biomedical applications. Particularly, surface-binding nanoparticles are important for carrying drugs whose targets are on the cell surface to stimulate the cells in a pseudo-autocrine mechanism. This can be used to activate signal transductions into the cell which are normally stimulated by secreted chemokines or cytokines from neighboring cells and tissue. Thus, the controlled release from nanoparticles forms a sustained local high drug concentration to continuously stimulate therapeutic cells, particularly mesenchymal stem cells, for the duration of the therapy.

However, the nanoparticles tethered on the cell surface are subjected to external forces such as shear stresses by fluid flow. One pertinent situation is during the injection of the cell suspension through a needle with a narrow diameter.[2] Using a 28G needle with a radius of 0.0925 mm, with a volumetric flow rate of 1 mL min^{-1}, cells at the wall would be subjected to a shear

stress of 140 dyn cm^{-2}. Therefore, the molecules selected to adsorb nanoparticles onto the cell surface have to withstand these forces to prevent detachment prior to transplantation. The adhesion strength of a ligand-receptor or antigen-antibody pair is related to the binding affinity.[3] For 4 μm microbubbles with a surface density of 2,500 antibody molecules per μm^2, the shear stress to detach half the number of adhered microbubbles was 34 dyn cm^{-2}.[4] Therefore, the strength and affinity of nanoparticles to the cell surface are important aspects in the nanoparticle design to overcome the critical mechanical stresses.

Modulating the surface activity of nanoparticles surface requires the consideration of the chemical and biological composition of the surface of the cell. With this knowledge, the two most direct ways to tether nanoparticles on the cell surface are through conjugation via covalent bonds or through specific physisorption via ligand-receptor or antigen-antibody interactions.[5] For the chemical conjugation of nanoparticles to the cell surface, functional groups that are reactive towards thiols or amines are presented on the exterior of the nanoparticle. To target thiols found on the cell surface, nanoparticles are functionalized with maleimide groups to react with the cysteine-rich extracellular domains of the membrane proteins. Leukocyte common antigen (CD45) and ATPase subunits of the sodium/potassium pumps were identified from mass spectrometry analysis as the predominant membrane anchors of maleimide-functionalized nanoparticles on T-cells.[6] For mesenchymal stem cells, efforts have been made to modify the cell surface amine groups with succinimidyl esters.[7] In these efforts, the chemical bond appears to provide a stable connection between the cells and the nanoparticle. However, a limitation of the chemical conjugation method is that the target protein involved in the conjugation is not specific. Unless a thorough study to identify the proteins involved and evaluate the downstream effects, this new and

long-lasting attachment might unintentionally affect other cellular functions even though the cells are still viable.[7]

Alternatively, nanoparticles could be functionalized with molecules to target specific proteins on the cell surface. Plasma membrane proteins displayed on the external surface function as cell adhesion molecules, signaling receptors, transporters, receptor and enzymes. The composition of specific proteins are unique to a cell type. Conjugation of receptor-specific ligands is a popular strategy in the area of targeted drug delivery. The ligand chosen to be conjugated to the nanoparticle would be one that binds to a receptor that is expressed in high quantities on the external membrane of the target cell type. For example, trastuzumab molecules have been conjugated to the surface of nanoparticles carrying anticancer drugs to increase the binding affinity towards a form of breast cancer expressing large numbers (1×10^6 per cell) of human epidermal growth factor receptor 2.[8] For mesenchymal stem cells (MSCs), they are identified by the high levels of cluster of differentiation (CD) markers CD29, CD44, CD73, CD90, CD105, CD146 and CD166. To differentiate them from the hematopoietic stem cells, MSCs are negative for CD14, CD34, CD45 and CD133.[9] Amongst the CD markers, CD44 is a cell adhesion molecule which interacts with hyaluronic acid found in the extracellular matrix.[10]

Taking advantage of the high affinity towards CD44, hyaluronic acid is identified as a compatible building block for preparing MSCs-supported biomaterials.[11] Hyaluronic acid is a linear polymer of (β, 1-4)-glucuronic acid and (β, 1-3)-*N*-acetyl glucosamine disaccharides found in the extracellular matrix of most tissues within the body and binds to a wide variety of protein called hyaladherins.[12] Hyaladherins are characterized into two groups, the structural hyaluronan-binding proteins of the extracellular matrix, such as the link protein, or the cell surface hyaluronan receptors, such as CD44 and CD168.[10] Most hyaladherins have structurally similar hyaluronan-

binding domains with sequence homologies of 30 – 40 %.[13] For CD44, the binding between hyaluronic acid and the protein is through hydrogen bonding as a mutation of the arginine residue within the binding domain causes nearly complete loss of hyaluronan-binding capacity.[13,14] The binding affinity of hyaluronic acid to CD44 depends on the molecular weight of hyaluronic acid. As a flexible polymer, hyaluronic acid forms a swollen random coil in dilute aqueous solution. The radius of gyration, R_g, is found to depend on the molecular weight: R_g = 1.3 nm × (molecular weight (kDa))$^{0.6}$.[15] For example, hyaluronic acid with a molecular weight of 1,000 kDa would have a radius of gyration of 21 nm. For molecular weights greater than 100 kDa, the high affinity towards CD44 is attributed to the capacity for 1 molecule of hyaluronic acid to bind to more than one CD44 receptor.[16,17] Therefore, the density of hyaluronic acid or the molecular weight of hyaluronic acid used to form the nanoparticle surface may be a crucial factor in nanoparticle-binding.

The conformation of surface ligands can affect the binding activity of the nanoparticle to cell surface receptors. In the case of polysaccharides, the sugar chains may be chemically-modified with hydrophobic groups to facilitate nanoparticle self-assembly. By employing different synthetic routes, there are two possible structures which affect the presentation of hyaluronic acid on the nanoparticles.[18] The first is a grafted copolymer with the polysaccharide as the backbone and the hydrophobic group on the side chains. Based on a study using dextran, the grafted copolymer would result in a tendency to form loops, closely resembling the native coiled form.[19] The second structure is a block copolymer with the hydrophobic group forming a chemical link in tandem with the terminal end of the polysaccharide. In general, the high-density arrangement of the individual molecules results in the polysaccharides forming a brush-like conformation. These extended brushes tend to prevent protein adsorption by steric repulsion.[20,21] Therefore, a grafted copolymer

that induces a highly looped structure may be provide a stronger anchor of hyaluronic acid-decorated nanoparticles to the cell surface.

Another concern is the internalization of nanoparticles upon the CD44 ligand-receptor recognition. In this regard, the size of the nanoparticle is an important factor that affects the fate of nanoparticles upon cell surface association. Following cell contact, nanoparticle internalization is mostly though receptor-mediated endocytosis which is an energy-dependent process. In this process, a high density of cell surface receptors coat the nanoparticle to result in the wrapping of the cell membrane around the nanoparticle. Thus, the efficiency of endocytosis for a given particle is dependent on the number of receptors required to trigger the uptake. Overall, human cells most efficiently internalize spherical nanoparticles with diameters between 25 and 50 nm.[22,23] Conversely, spherical nanoparticles greater than 70 nm bind to the cell surface but remained mostly localized in the cell surface.

Additionally, the mechanical properties of the microenvironment is found to have an influence on the rate of internalization of nanoparticles from the cell surface. Particularly, the plasma membrane tension increases with stiffer substrate.[24] In turn, the high membrane tension slows the active inward bending of the membrane required for nanoparticle endocytosis. [24–26] The membrane tension also changes when the cell transitions from the rounded state to the fully spread state.[27] Mechanical measurements found that the membrane tension first decreases from a relatively high level as the rounded cell spreads on the substrate.[28] Then, the membrane tension increases slightly as the cell undergoes cytoskeletal rearrangement and the formation of stable adhesions on the substrate. Finally, the membrane tension stabilizes to a constant value when the cell is fully spread on the substrate. Thus, the rate of nanoparticle endocytosis can be affected by the shape of the plasma membrane and the matrix that the cells are transplanted on.

Alternatively, a non-internalization receptor could be a target for cell surface engineering to prevent the internalization of nanoparticles. In the case of engineered T-cells, using nanoparticles covalently-conjugated with antibodies towards CD45 (non-internalizing receptor) achieved a more sustained drug effect from the continuous drug release on the cell surface over several days than nanoparticles covalently-conjugated with antibodies towards CD90 (internalizing receptor) that were internalized and degraded in the endolysosomal pathway.[29] Thus, the discovery of non-internalization receptors would be useful for mesenchymal stem cell surface engineering.

2.2 Amphiphilic micelle-forming polymers – Hydrophilic-hydrophobic balance

Apart from manipulating the external architecture of nanoparticles, synthetic polymers have been widely used as drug carriers for their capacity to tune the functional groups that form the nanoparticle core. For example, micelles with a hydrophobic core encapsulate molecules that are largely insoluble in water and blood. By formulating them with drugs, a more precise dose could be brought to the disease tissue such as a tumor. Upon arrival at the tumor, the micelles are internalized by cancer cells through endocytosis. The micelles then release the drugs to allow the diffusion of the drugs to their intracellular targets. Therefore, polymers for micelle drug delivery are carefully designed to encompass physicochemical properties to accomplish these steps.

Micelle-forming block copolymers consist of a hydrophilic polymer and a hydrophobic polymer connected by a covalent bond. To form micelles, polymers are first solvated in a water-soluble organic solvent that solubilizes both blocks. At this stage, the mobility of the polymer chain is high and aggregated structures are also freely moving and exchanging. Then, the addition of water removes the organic solvent from the hydrophobic domain. This slows the chain mobility to result in the self-assembly into micelle structures in which the insoluble block forms the core of

the micelle while the soluble block forms the corona.[30,31] The propensity for copolymers to form micelles is estimated by the mass fraction of the hydrophilic block to total mass of the copolymer and the glass transition temperatures. For poly(ethylene oxide)-*block*-poly(butadiene), the mass fraction of the poly(ethylene oxide) block to total mass of the copolymer needs to be greater than 0.45 in order for the copolymers to form spherical micelles.[32]

The polymer choice for the corona-forming hydrophilic block is important as it interacts closely with species in the surrounding media. Thus, the function of this polymer block is to increase the colloidal stability of the micelle in the biological environment populated by numerous proteins and patrolling immune cells.[33] Poly(ethylene glycol) chains in water are highly flexible and create a cloud of steric hindrance that provides the micelle protection against aggregation and interaction with blood components and proteins interactions such as enzymatic degradation or opsonization.[34] Individual chains interact by intermolecular van der Waals forces while the chains interact with water in the bulk solution by hydrogen bonding and dipole-dipole forces.[35] Shorter and lower surface density of poly(ethylene glycol) chains results in limited surface coverage of the micelle that leads to exposure of the hydrophobic core and micelle destabilization.

On the other hand, the hydrophobic block has a larger implication on the stability of the micelle which is assessed based on the micelle thermodynamic stability and kinetic stability. Thermodynamic stability describes changes in the polymer-aqueous system during micelle formation to reach equilibrium [35] and it is measured by the Gibbs free energy of micellization.[36] Using the phase separation model for nonionic surfactants, the molar Gibbs energy of micelle formation ($\Delta G_m^{micelle}$) is dependent on the critical micelle concentration (CMC) and are related through the equation, $\Delta G_m^{micelle} = RT \ln [CMC]$. The typical CMC values are below 1 M and thus, lower CMCs are indicative of higher micelle thermodynamic stability. The CMC could be lowered

by increasing the hydrophobicity of the polymer. At polymer concentrations above the CMC, the water molecules surrounding individual unimers orientate themselves to form hydrogen bonds with each other. An increased number of hydrogen bonds leads to a favorable increase in enthalpy. On the other hand, water molecules that form a solvation shell around the hydrophobic block of the copolymer experience a reduction in mobility. This leads to a loss in entropy. Therefore, the hydrophobic blocks of the copolymers are forced together to reduce the total surface area that breaks up the water hydrogen bond matrix to result in the lowest Gibbs free energy. Conversely, at a polymer concentration below the CMC, there are insufficient number of chains to self-assemble. Instead, the individual polymer chains are distributed and act as surfactants by adsorbing at the air-water interface.

Even after micelle formation, the individual chains are constantly exchanging between the micelles and the bulk solution. These dynamic nanostructures can also disassemble due to changes in the environment. Kinetic stability describes the dynamics between micelles and the environment over time and predicts the rate of polymer exchange and micelle disassembly.[35] This is affected by the polymer chain mobility which is lowered at temperatures below the polymer glass transition temperature. Thus, polymers with glass transition temperatures above ambient temperature such as polylactides are kinetically frozen because of the low mobility of the chains.[37] To impart greater kinetic stability within a micelle, functional groups capable of forming intermolecular electrostatic interactions, hydrogen bonds or chemical cross-links are incorporated in the same or different polymer chains.

Current studies are focused on controlling their disassembly to increase the efficiency of the release. To do so, the hydrophobic block of the copolymer is installed with reactive functional groups that respond to the biochemical difference in the microenvironments for selective cargo

unloading. These functional groups react with species that are in high abundance in specific cellular compartments or tissues. For example, in an acidic organelle such as the lysosome, the high concentration of protons could be used to ionize basic groups such as diethylamines. In micelles formed with poly[(ethylene oxide)-*block*-2-hydroxyethyl methacrylate-*block*-2-(diethylamino)ethyl methacrylate] triblock copolymers, micelles were formed at pH above the pKa of the diethyamine groups.[38] At low pH, the diethylamine groups become protonated and hydrophilic. As a result, the micelle core formed by 2-(diethylamino)ethyl methacrylate block swelled. On the other hand, nanoparticles containing poly(methacrylic acid) core swelled as more carboxylic acid groups become ionized with increasing pH due to the increased electrostatic repulsion within the core.[39] In another example of utilizing biochemical signals to prepare dynamic micelles, phenylboronic acid group were introduced into block copolymers to form micelles that were sensitive to an abnormal accumulation of glucose.[40] The complexation of glucose from the microenvironment and phenylboronic acid increased the hydrophilicity of the core and resulted in micelle expansion. Alternatively, polymers could be installed with chemical groups responsive to an external trigger such as a focused heat sources in photothermal therapy. At temperatures above the lower critical solution temperature of poly(*N*-isopropylacrylamide), the hydrophobic polymer chains are collapsed in a dehydrated state. Lowering the temperature leads to reordering of the chains to form hydrogen bonds with water molecules and results in a swollen and hydrated state. In micelles formed from poly(*N*-vinylpyrrolidone)-*block*-poly(*N*-isopropylacrylamide), the absorption of the large amounts of water led to the swelling of micelles.[41] As the nanoparticle size is a critical factor in affecting the nanoparticle permeability through fenestrated vasculatures,[42] the size of the micelles may also be controlled to prevent the undesirable accumulation of the small molecules in organs such as the heart, lungs and kidneys through size-exclusion effects.

To summarize, building micelles that responds to external stimuli provides a desirable additional control to the drug delivery carrier. It requires engineering polymers by balancing the hydrophobic and hydrophilic functional groups that affect the overall micelle physicochemical properties. This on demand activation of the nanoparticle could be a vital design feature to address problems such as side effects from non-specific drug interactions by free diffusing drugs and the escape of small nanoparticles through leaky vasculatures.

2.3 Porous microparticles – Pore mesostructures

Beside self-assembled nanoparticles formed from organic polymers, inorganic microparticles with porous features have important applications including catalysis and drug delivery systems.[43] Mesoporous silica is a family of microparticles with ordered porous features with intermediate pore diameters, ranging between 2 – 50 nm. These porous structures result in high surface area (> 500 m^2/g) which is advantageous for molecular adsorption. In this regard, the pore diameter and surface areas are important features in developing mesoporous silica as scaffolds for encapsulation of drugs and proteins for medical applications, gas adsorption for industrial separations or as catalyst supports for chemical synthesis.

Mesoporous silica microparticles of different mesostructures could be prepared by changing the synthesis method that controls the hydrolysis and condensation of the siloxane bond.[44,45] The building blocks consists of a silica source (e.g. silanes) and a structure directing (e.g. surfactants and micelle-forming polymers) agent. The synthesis rate is the slowest at the silica species isoelectric point of 2.0. Conversely, the rate of the hydrolysis is quicker when the silica species are positively or negatively charged in acidic or basic conditions, respectively. Particles are produced by first creating a burst nuclei, followed by a separate growth phase. At pH 2 – 7, negatively charged silica species assembly with positively-charged surfactants or neutral polymers

through electrostatic and hydrogen-bonding interactions. Under basic conditions (pH > 7.0), silica species assemble with cationic surfactants through strong electrostatic interactions. Subsequently, the condensation of silicates results in the formation of 3D mesostructures within microparticles.

Microparticles with hexagonally close packed cylindrical pore channels can be synthesized from a wide range of conditions. The most extensively investigated mesoporous silica molecular sieve is MCM-41 which is commonly synthesized using CTAB as a structure directing agent in a basic solution. Typical values of pore diameter and Braunauer – Emmett – Teller (BET) surface area are 4 nm and 1000 $m^2 g^{-1}$, respectively. Another important product is SBA-15, which is commonly synthesized using poly(ethylene) oxide (PEO) and poly(propylene) oxide (PPO) triblock copolymer (PEO-PPO-PEO) as a structure directing agent in an acidic solution. Typical values of pore diameter and BET surface area are ~6.5 to 10 nm and 800 $m^2 g^{-1}$. Compared to MCM-41 which has a pore wall thickness of about 1 nm and no micropores, SBA-15 pore walls range from 3.1 to 4.8 nm in thickness with disordered micropores in the silicate walls.[46]

These features contribute to differences in the molecular transport of small molecules. This is because the actual diffusion length could be longer than that of predicted by just considering the overall diameter of the particle [47] At low surface coverage, molecular transport within MCM-41 is strongly influenced by surface diffusion which accounts for significant interactions between the wall and the diffusing molecule.[48] In comparison, molecular transport in SBA-15 is dominated by a three-dimensional diffusion pathway through the micropores located with the mesoporous wall.[49] Therefore, these difference in molecular transport could have a significant effect on reactants that need to be in close proximity for electron transfer in order for the reaction to occur.

The effects of the architecture on the adsorption of small molecule drugs have been compared with MCM-41 and SBA-15 materials. In these studies, ibuprofen, a small molecule drug,

which has molecular dimensions of approximately 1 nm × 0.5 nm × 0.8 nm, is used as a model drug. Hydrogen bonding of Si-OH groups on SBA-15 or MCM-41 with the carboxyl group of ibuprofen could be detected with FTIR by a small blue shift from 1707 cm^{-1}.[50,51] Although MCM-41 materials have higher BET surface areas, the mass of adsorbed ibuprofen on MCM-41 is lower than on SBA-15. This was attributed to the narrow pore diameter and disordered domains of parallel short pore channels radially oriented toward the center of the particle which led to accumulation near the pore opening. In comparison, ibuprofen molecules could be adsorbed to form a film deposited along walls of the internal pore channels of SBA-15.[52] Loading with 30 wt % of ibuprofen results in the decrease in mesopore diameter from 8.4 to 6.3 nm.

The surface functional groups on the silica particles is important for solid catalysts and drug carriers. To present negatively-charged groups, trimethoxysilylpropyldiethylphosphonate or 3-mercaptopropyltrimethoxysilane is added to tetraethylorthosilicate to present phosphoric acid or sulfonic acids, respectively.[53–55] For the synthesis of mesoporous materials containing sulfonic acid, an additional oxidation step is necessary to convert the thiol groups to sulfonic acid. When this step was introduced during the synthesis, this in situ oxidation resulted in particles with larger pore diameters and pore volume compared to particles prepared by post-synthesis oxidation.[55] These materials are used as solid acid catalysts where larger pore diameters are desirable for more efficient mass transport and acid site accessibility.[56] Alternatively, to enhance the loading capacity of silica particles that are used as carriers, surface modification techniques could be performed on the silica scaffold. For example, silica surface groups could be modified after the particle synthesis to present amine groups using silane coupling agent 3-aminopropyltriethoxysilane. The surface amine groups are able form electrostatic interactions with carboxylic acid-containing molecules such as anti-inflammatory drug ibuprofen. Higher density of amine led to increased ibuprofen

adsorption in MCM-41 materials.[57] Conversely, functionalization could also lead to the loss of ordered structures and micropores. This resulted in lower accessibility to adsorption sites in SBA-15. Therefore, modifications in the synthesis process or post-synthesis may affect the nanostructure and surface properties and it is imperative to not assume that other characteristics would be similar to the parent silica particle.

To enhance the catalytic efficiency of homogenous systems, silica scaffolds could be doped with transition metals to speed up redox reactions. For example, iron(III)protoporphyrin(IX) was encapsulated in MCM-41 to produce mimic the activity of horseradish peroxidase.[58] Although this provides a more robust alternative to peroxidase which is deactivated at extreme pH and temperature, the material was unable to match the rate of oxidation by the peroxidase enzyme.

Given the versatility of these inorganic microparticles, there have been several efforts to combine silica scaffolds with organic hydrogels to form a hybrid material. Hydrogels, which are primarily crosslinked organic polymers to form a soft solid that take a variety of 3D structures, are widely applicable in areas such as biomedical implants, industrial piping and chemical adsorbents.[59,60] The crosslinks also form pores which allow movement of solutes throughout the volume of the hydrogel. The combination of the two distinct materials is appealing as each material could enhance or add properties of which the other material is lacking. In a poly(*N*,*N*-dimethylacrylamide)−silica hydrogel hybrid, the silica nanoparticles increased the stiffness of the gel network by creating additional physical cross-linking points.[61] Besides structural properties, the silica nanoparticles may be a source for bioactive molecules. For example, glass nanoparticles, which had a composition of 85 % SiO_2 and 15 % CaO, were a depot for Ca^{2+} and Si^{4+} ions to support osteogenesis for mesenchymal stem cells within a tissue-mimicking collagen-based

hydrogel.[62] Thus, the blend of merits from the high surface area inorganic microparticles and the tunable structural properties of hydrogels produces an attractive three-dimensional material.

To summarize, porous structures are advantageous in increasing the surface area for the adsorption of a variety of compounds. Yet, there has been few efforts in combining the efforts of these high surface area particles with hydrogel systems. Greater understanding on how to control these porous materials could prompt more ideas into using these materials to form novel solutions.

Overall, these nanoscale features make up our toolbox for building solutions for biomedical problems. It is intriguing how the porous structures and physicochemical properties within and on the surface of nanoparticles may be harness to increase the usefulness and efficiency of biotechnology. While the potential of utilizing these features have been explored in numerous prior demonstrations, there are many biomedical problems that are still unsolved. Therefore, there is a need to find a match of nanomaterials to the demand in the respective industries.

2.4 References

(1) Leong, J.; Teo, J. Y.; Aakalu, V. K.; Yang, Y. Y.; Kong, H. Engineering Polymersomes for Diagnostics and Therapy. *Adv. Healthc. Mater.* **2018**, *7*, 1701276.

(2) Aguado, B. A.; Mulyasasmita, W.; Su, J.; Lampe, K. J.; Heilshorn, S. C. Improving Viability of Stem Cells During Syringe Needle Flow Through the Design of Hydrogel Cell Carriers. *Tissue Eng. Part A* **2012**, *18*, 806–815.

(3) Kuo, S. C.; Lauffenburger, D. A. Relationship between Receptor/Ligand Binding Affinity and Adhesion Strength. *Biophys. J.* **1993**, *65*, 2191–2200.

(4) Takalkar, A. M.; Klibanov, A. L.; Rychak, J. J.; Lindner, J. R.; Ley, K. Binding and Detachment Dynamics of Microbubbles Targeted to P-Selectin under Controlled Shear Flow. *J. Control. Release* **2004**, *96*, 473–482.

(5) Stephan, M. T.; Irvine, D. J. Enhancing Cell Therapies from the Outside in: Cell Surface Engineering Using Synthetic Nanomaterials. *Nano Today* **2011**, *6*, 309–325.

(6) Stephan, M. T.; Stephan, S. B.; Bak, P.; Chen, J.; Irvine, D. J. Synapse-Directed Delivery of Immunomodulators Using T-Cell-Conjugated Nanoparticles. *Biomaterials* **2012**, *33*, 5776–5787.

(7) Cheng, H.; Byrska-Bishop, M.; Zhang, C. T.; Kastrup, C. J.; Hwang, N. S.; Tai, A. K.; Lee, W. W.; Xu, X.; Nahrendorf, M.; Langer, R.; *et al.* Stem Cell Membrane Engineering for Cell Rolling Using Peptide Conjugation and Tuning of Cell-Selectin Interaction Kinetics. *Biomaterials* **2012**, *33*, 5004–5012.

(8) Nielsen, U. B.; Kirpotin, D. B.; Pickering, E. M.; Drummond, D. C.; Marks, J. D. A Novel Assay for Monitoring Internalization of Nanocarrier Coupled Antibodies. *BMC Immunol.* **2006**, *7*, 24.

(9) Niehage, C.; Steenblock, C.; Pursche, T.; Bornhäuser, M.; Corbeil, D.; Hoflack, B. The Cell Surface Proteome of Human Mesenchymal Stromal Cells. *PLoS One* **2011**, *6*, e20399.

(10) Zhu, H.; Mitsuhashi, N.; Klein, A.; Barsky, L. W.; Weinberg, K.; Barr, M. L.; Demetriou, A.; Wu, G. D. The Role of the Hyaluronan Receptor CD44 in Mesenchymal Stem Cell Migration in the Extracellular Matrix. *Stem Cells* **2006**, *24*, 928–935.

(11) Toh, W. S.; Lim, T. C.; Kurisawa, M.; Spector, M. Modulation of Mesenchymal Stem Cell Chondrogenesis in a Tunable Hyaluronic Acid Hydrogel Microenvironment. *Biomaterials* **2012**, *33*, 3835–3845.

(12) Knudson, W.; Peterson, R. S. The Hyaluronan Receptor: CD44. In *Chemistry and Biology of Hyaluronan*; Elsevier, 2004; pp. 83–123.

(13) Yang, B.; Yang, B. L.; Savani, R. C.; Turley, E. A. Identification of a Common Hyaluronan Binding Motif in the Hyaluronan Binding Proteins RHAMM, CD4 and Link Protein. *EMBO J.* **1994**, *1*, 286–296.

(14) Banerji, S.; Wright, A. J.; Noble, M.; Mahoney, D. J.; Campbell, I. D.; Day, A. J.; Jackson, D. G. Structures of the Cd44-Hyaluronan Complex Provide Insight into a Fundamental Carbohydrate-Protein Interaction. *Nat. Struct. Mol. Biol.* **2007**, *14*, 234–239.

(15) Takahashi, R.; Kubota, K.; Kawada, M.; Okamoto, A. Effect of Molecular Weight Distribution on the Solution Properties of Sodium Hyaluronate in 0.2M NaCl Solution. *Biopolymers* **1999**, *50*, 87.

(16) Mizrahy, S.; Raz, S. R.; Hasgaard, M.; Liu, H.; Soffer-Tsur, N.; Cohen, K.; Dvash, R.; Landsman-Milo, D.; Bremer, M. G. E. G.; Moghimi, S. M.; *et al.* Hyaluronan-Coated Nanoparticles: The Influence of the Molecular Weight on CD44-Hyaluronan Interactions and on the Immune Response. *J. Control. Release* **2011**, *156*, 231–238.

(17) Wolny, P. M.; Banerji, S.; Gounou, C.; Brisson, A. R.; Day, A. J.; Jackson, D. G.; Richter, R. P. Analysis of CD44-Hyaluronan Interactions in an Artificial Membrane System: Insights into the Distinct Binding Properties of High and Low Molecular Weight

Hyaluronan. *J. Biol. Chem.* **2010**, *285*, 30170–30180.

(18) Lemarchand, C.; Gref, R.; Couvreur, P. Polysaccharide-Decorated Nanoparticles. *European Journal of Pharmaceutics and Biopharmaceutics*, 2004, *58*, 327–341.

(19) Chauvierre, C.; Vauthier, C.; Labarre, D.; Hommel, H. Evaluation of the Surface Properties of Dextran-Coated Poly(Isobutylcyanoacrylate) Nanoparticles by Spin-Labelling Coupled with Electron Resonance Spectroscopy. *Colloid Polym. Sci.* **2004**, *282*, 1016–1025.

(20) Passirani, C.; Barratt, G.; Devissaguet, J. P.; Labarre, D. Interactions of Nanoparticles Bearing Heparin or Dextran Covalently Bound to Poly(Methyl Methacrylate) with the Complement System. *Life Sci.* **1998**, *62*, 775–785.

(21) Minsky, B. B.; Antoni, C. H.; Boehm, H. Controlled Immobilization Strategies to Probe Short Hyaluronan-Protein Interactions. *Sci. Rep.* **2016**, *6*, 21608.

(22) Gao, H.; Shi, W.; Freund, L. B. Mechanics of Receptor-Mediated Endocytosis. *Proc. Natl. Acad. Sci. U. S. A.* **2005**, *102*, 9469–9474.

(23) Zhang, S.; Li, J.; Lykotrafitis, G.; Bao, G.; Suresh, S. Size-Dependent Endocytosis of Nanoparticles. *Adv. Mater.* **2009**, *21*, 419–424.

(24) Huang, C.; Butler, P. J.; Tong, S.; Muddana, H. S.; Bao, G.; Zhang, S. Substrate Stiffness Regulates Cellular Uptake of Nanoparticles. *Nano Lett.* **2013**, *13*, 1611–1615.

(25) Diz-Muñoz, A.; Fletcher, D. A.; Weiner, O. D. Use the Force: Membrane Tension as an Organizer of Cell Shape and Motility. *Trends in Cell Biology*, 2013, *23*, 47–53.

(26) Apodaca, G. Modulation of Membrane Traffic by Mechanical Stimuli. *Am. J. Physiol. Renal Physiol.* **2002**, *282*, F179–F190.

(27) Pietuch, A.; Janshoff, A. Mechanics of Spreading Cells Probed by Atomic Force Microscopy. *Open Biol.* **2013**, *3*, 130084–130084.

(28) Gauthier, N. C.; Masters, T. A.; Sheetz, M. P. Mechanical Feedback between Membrane Tension and Dynamics. *Trends in Cell Biology*, 2012, *22*, 527–535.

(29) Zheng, Y.; Tang, L.; Mabardi, L.; Kumari, S.; Irvine, D. J. Enhancing Adoptive Cell Therapy of Cancer through Targeted Delivery of Small-Molecule Immunomodulators to Internalizing or Noninternalizing Receptors. *ACS Nano* **2017**, *11*, 3089–3100.

(30) Cui, H.; Chen, Z.; Zhong, S.; Wooley, K. L.; Pochan, D. J. Block Copolymer Assembly via Kinetic Control. *Science (80-.).* **2007**, *317*, 647–650.

(31) Lund, R.; Willner, L.; Stellbrink, J.; Radulescu, A.; Richter, D. Role of Interfacial Tension for the Structure of PEP-PEO Polymeric Micelles. A Combined SANS and Pendant Drop Tensiometry Investigation. *Macromolecules* **2004**, *37*, 9984–9993.

(32) Discher, D. E.; Eisenberg, A. Polymer Vesicles. *Science* **2002**, *297*, 967–973.

(33) Moore, T. L.; Rodriguez-Lorenzo, L.; Hirsch, V.; Balog, S.; Urban, D.; Jud, C.; Rothen-Rutishauser, B.; Lattuada, M.; Petri-Fink, A. Nanoparticle Colloidal Stability in Cell Culture Media and Impact on Cellular Interactions. *Chem. Soc. Rev.* **2015**, *44*, 6287–6305.

(34) Knop, K.; Hoogenboom, R.; Fischer, D.; Schubert, U. S. Poly(Ethylene Glycol) in Drug Delivery: Pros and Cons as Well as Potential Alternatives. *Angewandte Chemie - International Edition*, 2010, *49*, 6288–6308.

(35) Owen, S. C.; Chan, D. P. Y.; Shoichet, M. S. Polymeric Micelle Stability. *Nano Today*, 2012, *7*, 53–65.

(36) Butt, H.-J.; Graf, K.; Kappl, M. *12 Surfactants,Micelles, Emulsions, and Foams*; Wiley-VCH Verlag GmbH & Co. KGaA: Weinheim, FRG, 2003.

(37) Mai, Y.; Eisenberg, A. Self-Assembly of Block Copolymers. *Chem. Soc. Rev.* **2012**, *41*, 5969.

(38) Liu, S.; Weaver, J. V. M.; Save,M; Armes, S. P. Synthesis of PH-Responsive Shell Cross-Linked Micelles and Their Use as Nanoreactors for the Preparation of Gold Nanoparticles. **2002**, *18*, 8350.

(39) Qu, J. B.; Chapman, R.; Chen, F.; Lu, H.; Stenzel, M. H. Swollen Micelles for the Preparation of Gated, Squeezable, PH-Responsive Drug Carriers. *ACS Appl. Mater. Interfaces* **2017**, *9*, 13865–13874.

(40) Wang, B.; Ma, R.; Liu, G.; Li, Y.; Liu, X.; An, Y.; Shi, L. Glucose-Responsive Micelles from Self-Assembly of Poly(Ethylene Glycol)-a-Poly(Acrylic Acid-Co-Acrylamidophenylboronic Acid) and the Controlled Release of Insulin. *Langmuir* **2009**, *25*, 12522–12528.

(41) Zhu, Z.; Sukhishvili, S. A. Temperature-Induced Swelling and Small Molecule Release with Hydrogen- Bonded Multilayers of Block Copolymer Micelles. *ACS Nano* **2009**, *3*, 3595–3605.

(42) Ho, Y. T.; Adriani, G.; Beyer, S.; Nhan, P. T.; Kamm, R. D.; Kah, J. C. Y. A Facile Method to Probe the Vascular Permeability of Nanoparticles in Nanomedicine Applications. *Sci. Rep.* **2017**, *7*, 707.

(43) Choi, Y.; Lee, J. E.; Lee, J. H.; Jeong, J. H.; Kim, J. A Biodegradation Study of SBA-15 Microparticles in Simulated Body Fluid and in Vivo. *Langmuir* **2015**, *31*, 6457–6462.

(44) Wan, Y.; Zhao, D. On the Controllable Soft-Templating Approach to Mesoporous Silicates. *Chem. Rev.* **2007**, *107*, 2821–2860.

(45) Wu, S.-H.; Mou, C.-Y.; Lin, H.-P. Synthesis of Mesoporous Silica Nanoparticles. *Chem. Soc. Rev.* **2013**, *42*, 3862.

(46) Joo, S. H.; Ryoo, R.; Kruk, M.; Jaroniec, M. Evidence for General Nature of Pore Interconnectivity in 2-Dimensional Hexagonal Mesoporous Silicas Prepared Using Block Copolymer Templates. *J. Phys. Chem. B* **2002**, *106*, 4640–4646.

(47) Vattipalli, V.; Qi, X.; Dauenhauer, P. J.; Fan, W. Long Walks in Hierarchical Porous Materials Due to Combined Surface and Configurational Diffusion. *Chem. Mater.* **2016**, *28*, 7852–7863.

(48) Qiao, S. Z.; Bhatia, S. K. Diffusion of Linear Paraffins in Nanoporous Silica. *Ind. Eng. Chem. Res.* **2005**, *44*, 6477–6484.

(49) Huang, Q.; Eić, M.; Xiao, H.; Kaliaguine, S. Characterization of the Diffusion Path in Micro- and Meso-Porous Materials from ZLC Analysis. In *Adsorption*; 2010; Vol. 16, pp. 531–539.

(50) Song, S. W.; Hidajat, K.; Kawi, S. Functionalized SBA-15 Materials as Carriers for Controlled Drug Delivery: Influence of Surface Properties on Matrix-Drug Interactions. *Langmuir* **2005**, *21*, 9568–9575.

(51) Muñoz, B.; Rámila, A.; Pérez-Pariente, J.; Díaz, I.; Vallet-Regí, M. MCM-41 Organic Modification as Drug Delivery Rate Regulator. *Chem. Mater.* **2003**, *15*, 500–503.

(52) Mellaerts, R.; Jammaer, J. A. G.; Van Speybroeck, M.; Hong, C.; Van Humbeeck, J.; Augustijns, P.; Van Den Mooter, G.; Martens, J. A. Physical State of Poorly Water Soluble Therapeutic Molecules Loaded into SBA-15 Ordered Mesoporous Silica Carriers: A Case Study with Itraconazole and Ibuprofen. *Langmuir* **2008**, *24*, 8651–8659.

(53) Corriu, R. J. P.; Guari, Y.; Mehdi, A.; Reyé, C.; Thieuleux, C.; Datas, L. Ordered SBA-15 Mesoporous Silica Containing Phosphonic Acid Groups Prepared by a Direct Synthetic Approach. *Chem. Commun.* **2001**, 763–764.

(54) Van Rhijn, W. M.; De Vos, D. E.; Sels, B. F.; Bossaert, W. D.; Jacobs, P. A. Sulfonic Acid Functionalized Ordered Mesoporous Materials as Catalysts for Condensation and Esterification Reactions. *Chem. Commun.* **1998**, 317–318.

(55) Margolese, D.; Melero, J. A.; Christiansen, S. C.; Chmelka, B. F.; Stucky, G. D. Direct Syntheses of Ordered SBA-15 Mesoporous Silica Containing Sulfonic Acid Groups. *Chem. Mater.* **2000**, *12*, 2448–2459.

(56) Dacquin, J. P.; Lee, A. F.; Pirez, C.; Wilson, K. Pore-Expanded SBA-15 Sulfonic Acid Silicas for Biodiesel Synthesis. *Chem. Commun.* **2012**, *48*, 212–214.

(57) Szegedi, A.; Popova, M.; Goshev, I.; Mihály, J. Effect of Amine Functionalization of Spherical MCM-41 and SBA-15 on Controlled Drug Release. *J. Solid State Chem.* **2011**, *184*, 1201–1207.

(58) Nazari, K.; Shokrollahzadeh, S.; Mahmoudi, A.; Mesbahi, F.; Matin, N. S.; Moosavi-Movahedi, A. A. Iron(III)Protoporphyrin/MCM41 Catalyst as a Peroxidase Enzyme

Model: Preparation and Typical Test Reactions. *J. Mol. Catal. A Chem.* **2005**, *239*, 1–9.

(59) Khan, M.; Lo, I. M. C. A Holistic Review of Hydrogel Applications in the Adsorptive Removal of Aqueous Pollutants: Recent Progress, Challenges, and Perspectives. *Water Res.* **2016**, *106*, 259–271.

(60) Yu, A. C.; Chen, H.; Chan, D.; Agmon, G.; Stapleton, L. M.; Sevit, A. M.; Tibbitt, M. W.; Acosta, J. D.; Zhang, T.; Franzia, P. W.; *et al.* Scalable Manufacturing of Biomimetic Moldable Hydrogels for Industrial Applications. *Proc. Natl. Acad. Sci.* **2016**, *113*, 14255–14260.

(61) Lin, W. C.; Fan, W.; Marcellan, A.; Hourdet, D.; Creton, C. Large Strain and Fracture Properties of Poly(Dimethylacrylamide)/Silica Hybrid Hydrogels. *Macromolecules* **2010**, *43*, 2554–2563.

(62) El-Fiqi, A.; Lee, J. H.; Lee, E.-J.; Kim, H.-W. Collagen Hydrogels Incorporated with Surface-Aminated Mesoporous Nanobioactive Glass: Improvement of Physicochemical Stability and Mechanical Properties Is Effective for Hard Tissue Engineering. *Acta Biomater.* **2013**, *9*, 9508–9521.

CHAPTER 3: Surface tethering of TNFα nanostimulator to enhance the efficacy of adipose-derived stem cells for treatment of acute limb ischemia

Acknowledgements

Kyeongsoo Kim for the 3D angiogenesis assay, Eunkyung Ko for performing the surgery for the mouse ischemic hindlimb model, Svyatoslav Dvoretskiy for the muscle force measurements, Yu-Fu Wu for the immunohistochemistry analysis (not shown). DLS and TEM data were acquired at the Frederick Seitz Materials Research Laboratory Central Facilities at the University of Illinois.

3.1 Introduction

Adipose-derived stem cells (ADSCs) have emerged as a new generation of medicine that can repair ischemic tissues stemming from vascular rupture or occlusion.[1] ADSCs endogenously secrete multiple growth factors and cytokines that can orchestrate recruitment, proliferation, and differentiation of tissue-forming host cells, while alleviating inflammation and cell death.[2] For instance, ADSCs secrete both proangiogenic vascular endothelial growth factor and anti-angiogenic pigment epithelium-derived factor to regulate endothelial sprouting and maturation in a balanced manner.[3] Cells also secrete monocyte chemoattractant protein-1 that stimulates angiogenesis to restore perfusion to the tissues.[4] ADSCs also secrete immunomodulatory factors, such as prostaglandin E_2 (PGE_2). PGE_2 inhibits the T cell proliferation but does not affect their function. As a result, transplanted cells support the tissue recovery process by modulating the level of inflammation.[5] This prevents the detrimental escalation of infiltrating leukocytes that release reactive oxygen species and hence block tissue recovery.[6] Furthermore, ADSCs have been found

to evade allogenic rejection so the cells from other donors can be transplanted. It is also possible to expand ADSCs collected from a patient in vitro to attain desired number of cells for therapies.

Currently, pre-clinical studies are working on the strategy to inject ADSCs into the ischemic tissue for a better therapeutic outcome than to administer the conditioned media collected from the ADSC culture in vitro. [7] Success in the cell therapy therefore relies on the ability to activate transplanted stem cells in a sustainable manner. To meet these challenges, cells would be conditioned in vitro through soluble factors or oxygen-deprivation. For example, ADSCs grown long term under hypoxic conditions were stimulated to upregulate the secretion of growth factors and cytokines. Therefore, pre-conditioning may provide a potential means of enhancing efficacy of cell therapy by priming the cells prior to transplantation. However, the sustainability of the pre-conditioning treatment from ex vitro culture to in vivo transplantation is still unclear.[8,9] A critical concern is that the upregulation from the pre-treatment will be lost after exposure to the in vivo environment.[9] This motivated studies to use gene therapy to increase the life-time of proteins such as anti-apoptotic proteins and hypoxia-inducing factors.[10–13] Additionally, there are other factors including media composition and ex vivo passaging that often alter the cellular activity to secrete therapeutic molecules.[14,15]

We hypothesize that in situ activation of ADSCs with cell-adherent liposomes releasing tumor necrosis factor-α (TNFα), named as a "nanostimulator" would allow us to sustainably stimulate the cells to secrete therapeutic molecules in the transplanted tissue (**Scheme 3.1**). This unprecedented strategy would significantly improve therapeutic efficacy of ADSCs to treat tissue damaged by acute injury. To examine this hypothesis, we encapsulated TNFα into the liposomes coated by hyaluronic acid that binds with CD44 of ADSCs. The diameter of liposomes was kept constant at 400 nm, so as to minimize cellular uptake of liposomes. First, we examined the binding

kinetics of the nanostimulator on ADSCs and residence on the cell surface. Next, we analyzed secretion profiles of ADSCs modulated by the nanostimulator and subsequent neovascularization using a microfluidic chip, along with underlying cell signaling pathways. Finally, we tested therapeutic efficacy of the ADSCs by transplanting them into the mouse model for acute limb ischemia and monitoring the recovery of perfusion and the retention of muscle physiology.

3.2 Results

3.2.1 Assembly of nanostimulator, an ADSC-adherent liposomal carrier of TNFα

Hyaluronic acid that binds to adipose-derived stem cell (ADSC) surface receptor CD44 and CD168 was chemically modified to associate with liposomes. Hyaluronic acid (HA) was alkylated by forming an amide bond between octadecylamine and glucuronic acid monomers of hyaluronic acid, catalyzed by 1-ethyl-3-(3-dimethylaminopropyl)carbodiimide and *N*-hydroxysuccinimide. The presence of octadecyl chains on hyaluronic acid was confirmed by the presence of the triplet at 0.85 ppm on the ^{1}H NMR spectroscopy spectrum, assigned to the protons on the terminal carbon of octadecylamine (**Figure 3.1**). The degree of substitution was calculated to be 3% by taking the ratio of CH_3 between octyldecylamine and glucosamine groups. The resulting alkyl-substituted hyaluronic acid, termed as HA-g-C18, is soluble in cell culture media supplemented with 10% serum.

Liposomes coated with HA-g-C18 were prepared by hydrating a thin film of lipid molecules followed by vigorous mixing of resulting liposomes with HA-g-C18. To examine the spatial distribution of the HA-g-C18 on the liposomes, HA-g-C18 and lipid molecules were labeled

with rhodamine B and nitrobenzoxadiazole, respectively. The confocal image shown in **Figure 3.2A** displayed the co-localization of fluorescence from HA-g-C18 and the lipid bilayer.

The role of octadecyl chains of HA-g-C18 on increasing binding affinity between HA and liposome was examined with the fluorescence resonance energy transfer (FRET) between rhodamine B (FRET acceptor) on HA and nitrobenzoxadiazole on the liposome (FRET donor). Upon excitation at wavelength 420 nm, an absorption wavelength of nitrobenzoxadiazole, the aqueous mixture of HA-g-C18 and liposomes displayed a decreased emission intensity of nitrobenzoxadiazaole maximized at 530 nm, compared with the emission intensity of the liposome free of HA-g-C18 (**Figure 3.2B**). Also, the mixture of liposome and HA-g-C18 showed the increased emission intensity of rhodamine B maximized at 590 nm compared with the aqueous solution of HA-g-C18. Both the decrease of the FRET donor emission intensity and the increase of the FRET acceptor emission intensity indicate the close proximity of HA and liposomes. The FRET efficiency, calculated using **Equation 3.1** was 22%. In contrast, the aqueous mixture of unmodified hyaluronic acid and liposomes exhibited an increase of the emission intensity of rhodamine B maximized at 590 nm, but a FRET efficiency being 13% was lower than that of the mixture of HA-g-C18 and liposomes (**Figure 3.2C**).

The resulting liposomes coated with HA-g-C18 were resized to nano-sized particles by extruding them through a 400-nm pore diameter membrane. The diameters of the liposomes were uniformly 400 nm as confirmed with dynamic light scattering measurements (**Figure 3.3A**). The diameters of dehydrated liposomes measured under the transmission electron microscope were approximately 100 nm (**Figure 3.3B**).

1,2-dipalmitoyl-*sn*-glycero-3-phosphocholine exists as a zwitterionic form and confers the liposomes formed with a net neutral charge. In contrast, glucuronic acid of HA has a pKa of 3.2 and is therefore deprotonated to present negative charge in DI water. The zeta potential of unmodified liposomes was 5 mV, while that of the liposome coated with HA-g-C18 was -36 mV (**Figure 3.3C**). Due to the negative zeta potential, the liposomes coated with HA-g-C18 remained more stable in aqueous media than unmodified liposomes. In blood-mimicking media containing serum albumin, liposomes coated with HA-g-C18 remained stable for at least 24 h, while unmodified liposomes aggregated immediately to form particles of greater than 1 μm (**Figure 3.3D-F**).

3.2.2 Kinetic analysis of the liposome tethering to ADSC surface

We assessed the extent that HA immobilized on the liposome modulates the number of liposomes tethered to ADSCs using the liposome labeled with nitrobenzoxadiazole. Cells were incubated in the suspension of unmodified liposome or liposome coated with HA-g-C18 for 15 minutes while gently shaking the mixture at 37 °C. According to the confocal images of cells captured after removing non-adherent liposomes, cells that were incubated with liposomes coated with HA-g-C18 yielded a larger fluorescence than cells incubated with unmodified liposomes (**Figure 3.4A**). In parallel, the number of liposomes tethered to cells was counted with fluorescence spectroscopy. The number of unmodified liposomes per cell was 58,000, while that of liposomes coated with HA-g-C18 was 94,000 (**Figure 3.4B**).

To estimate the equilibrium dissociation constant, K_D, the ADSCs were incubated with different concentrations of nitrobenzoxadiazole-labeled liposomes and the number of surface-tethered liposomes at equilibrium was measured (**Figure 3.4C(i)**, **Equation 3.2**). Liposomes coated with HA-g-C18 associated with ADSCs at a higher affinity than unmodified liposomes. K_D

of liposomes coated with HA-g-C18 was 93 pM, while that of unmodified liposomes was 231 pM. In addition, the dissociation rate constant, k_{-1}, was measured by placing ADSCs with surface-tethered liposomes in fresh media and counting the number of liposomes remaining on the cell surface at various time points (**Figure 3.4C(ii)**, **Equation 3.3**). The k_{-1} of the liposomes coated with HA-g-C18 was 0.0091 min^{-1}, while that of unmodified liposomes was 0.013 min^{-1}. As a result, the time required for half the liposomes coated with HA-g-C18 to dissociate from the surface ($t_{1/2}$), calculated using **Equation 3.4** was 76 min. In contrast, $t_{1/2}$ of the unmodified liposomes was 53 min.

To determine if the ADSCs suspended in media took up liposomes coated with HA-g-C18, intracellular lysosomes were labeled with Lysotracker Green. Separately, HA-g-C18 on the surface of liposomes were chemically coupled with rhodamine B. If the cells took up the liposomes, there should be co-localization of fluorescence signals from both liposomes and lysosomes. Liposomes were found only on the cell surface after incubating cells in suspension for 2 hours (**Figure 3.5A**). Then, cells were seeded on a type I collagen gel to simulate cells transplanted in tissue. After 24 hours, most of the liposomes were found on the cell surface as confirmed with minimal co-localization of fluorescence from liposomes and lysosomes (**Figure 3.5B**). There was no significant cellular uptake of liposomes even after 3 days (**Figure 3.5C**) and 5 days incubation (**Figure 3.5D**).

3.2.3 In vitro analysis of the stimulatory function of TNFα-releasing liposomes coated with HA-g-C18 (HA-liposomes)

TNFα was loaded into the liposomes by mixing them into the hydration medium used to form the liposomes. The encapsulation efficiency of TNFα loaded in unmodified liposomes and liposomes coated with HA-g-C18 (HA-liposomes) were 73% and 83%, respectively. The release

profile of TNFα from HA-liposomes showed a sustained and steady release over 5 days of incubation in neutral media at 37 °C (**Figure 3.6A**). In contrast, the release profile of the liposomes without HA-g-C18 follows a biphasic profile. 20% of the loaded TNFα was released initially due to the unstable aggregation of liposomes shown in **Figure 3.3E**. Then, liposomes released TNFα slowly. The TNFα release profiles were fit against the empirical model describing the fractional release at time t, $\frac{\text{Cumulative mass of TNF}\alpha\text{ released at time,t}}{\text{Total mass of TNF}\alpha\text{ released}} = \text{kt}^{\text{n}}$ (**Figure 3.6B**). In the equation, *k* represents the release rate constant and *n* represents the release exponent. *n* for liposomes coated with HA-g-C18 was 0.34 which indicates that liposomes released TNFα mainly by diffusion (**Figure 3.6C**).[16] In contrast, *n* of the unmodified liposomes was 0.21, which may be attributed to polydispersed size distribution. The *k* value for unmodified liposomes was 5-fold higher than that of liposomes coated with HA-g-C18, indicating that the HA-g-C18 coating reduced the rate of TNFα release (**Figure 3.6D**).

Next, the secretion profile of the ADSCs activated by the TNFα-releasing liposome was examined with an array of antibodies towards angiogenesis-related proteins (**Figure 3.7A**). During 24 h of cell culture on the type I collagen gel, ADSCs released a series of proangiogenic factors, activin A, angiogenin, interleukin-8 (IL-8), monocyte chemoattractant protein 1 (MCP-1), vascular endothelial growth factor (VEGF) and anti-angiogenic factors, pigment epithelium-derived factor (PEDF). The cells also secrete inhibitors such as tissue inhibitor of metalloproteinase-1 (TIMP-1) and plasminogen activator inhibitor (PAI-1), which decrease remodeling and fibrosis, respectively. Additionally, the cells released anti-apoptotic cytokines insulin-like growth factor-binding protein 3 (IGFBP-3), pentraxin-related protein (PTX-3), thrombospondin-1 (TSP-1) and urokinase plasminogen activator (uPA). Interestingly, compared with untreated ADSCs, ADSCs tethered with TNFα-releasing HA-liposomes exhibited increased secretion levels of activin A, angiogenin,

MCP-1, VEGF, PEDF and uPA, and decreased secretion levels of IL-8 and TSP-1 (**Figure 3.7B**). The secretion levels of IGFBP-3, TIMP-1, PAI-1 and PTX-3 remained the same.

The long-term secretion levels of pro-angiogenic VEGF, anti-angiogenic PEDF, and immunomodulatory prostaglandin E_2 (PGE_2) were measured using ELISA for individual proteins. On Day 1, the VEGF secretion levels of ADSCs tethered with TNFα-releasing HA-liposomes was 1.7-fold higher than untreated ADSCs (**Figure 3.8A**). VEGF secretion was sustained and reached to 3 ng mL^{-1} after 5 days (**Figure 3.8B**). The VEGF secretion level of ADSCs tethered with TNFα-releasing HA-liposomes was 1.9-fold higher than the untreated ADSCs or ADSCs mixed with unmodified liposomes. Also, interestingly, ADSCs tethered with blank HA-liposomes secreted a 1.6-fold larger VEGF than untreated ADSCs.

To determine the mechanism for activating VEGF up-regulation, ADSCs were incubated with inhibitors to VEGF transcription regulators including extracellular signal-regulated kinases (ERK) and p38 mitogen-activated protein kinases (MAPK). The inhibitors had minimal effects on the untreated ADSCs. In contrast, for ADSCs tethered with TNFα-releasing HA-liposomes, the MAPK inhibitor suppressed the VEGF secretion level more significantly than the ERK inhibitor (**Figure 3.8C**).

Concurrently, the secretion levels of PEDF by ADSCs continued to increase from 3 to 40 ng mL^{-1} over 5 days of culture (**Figure 3.8D** & **E**). No difference of the secretion level was found among untreated ADSCs, ADSCs mixed with unmodified liposomes, and ADSCs tethered with blank HA-liposomes. In contrast, the ADSCs tethered with TNFα-releasing HA-liposomes exhibited 1.2-fold lower secretion level of PEDF.

Immunomodulatory PGE_2 is a potent mediator responsible for immunosuppression and anti-inflammation by ADSCs.[17] ADSCs tethered with TNFα-releasing HA-liposome displayed 2-fold higher PGE_2 secretion steadily over 48 h than other conditions including untreated ADSCs, ADSCs mixed with unmodified liposomes, and ADSCs tethered with blank HA-liposomes (**Figure 3.8F**). After 48 h, the PGE_2 secretion level was approximately 9 ng mL^{-1}.

Subsequent studies then focused on analyzing the therapeutic activities of ADSCs tethered with TNFα-releasing HA-liposomes in comparison to untreated ADSCs. The therapeutic efficacy of the activated ADSCs to induce angiogenesis was assessed with a 3D microvascular device assembled for in vitro neovascularization study (**Figure 3.9A**). Human umbilical vein endothelial cells (HUVEC) as vascular precursor cells were seeded in a fibrin gel that filled the central channel (**Figure 3.9B**). ADSCs were seeded in a fibrin gel that filled the outer channels. Thus, bioactive molecules released from ADSCs diffuse into the central channel in which HUVECs reside. In the absence of ADSCs, HUVECs aggregated to a form of cell clusters. In the presence of untreated ADSCs, HUVECs formed hollow endothelial lumens, which were interconnected to each other (**Figure 3.9C**). ADSCs tethered with TNFα-releasing HA-liposomes resulted in endothelial lumen which is interconnected more compactly than untreated ADSCs. The tubule length was increased by 1.3-folds with ADSCs tethered with TNFα-releasing HA-liposomes, compared with untreated ADSCs (**Figure 3.9D**). The number of interconnected junctions was 1.3-folds greater with ADSCs tethered with TNFα-releasing HA-liposomes than untreated ADSCs (**Figure 3.9E**).

3.2.4 In vivo assessment of therapeutic efficacy of ADSCs to treat ischemic hindlimb

Finally, the therapeutic efficacy of ADSCs tethered with TNFα-releasing HA-liposomes was evaluated in vivo by using an ischemic hindlimb model introduced into CD-1 mice (**Figure 3.10A**). The ligation of right femoral artery and vein resulted in the impaired perfusion as

confirmed with the Laser Doppler perfusion imaging (LDPI) (**Figure 3.10B**). In contrast, the left intact hindlimb retained normal perfusion, same as the mouse which did not undertake the vascular ligation. The saline solution, untreated ADSCs, or ADSCs tethered with TNFα-releasing HA-liposomes were injected into the quadriceps and calf muscles immediately after vascular ligation.

According to the LDPI measurements, on the first day after the ischemic injury was induced, the mice from all experimental groups had an average perfusion ratio of 0.15, which is quantified as the ratio of perfusion between the right ischemic hindlimb and the left intact hindlimb. Subsequently on Day 7, the mice transplanted with untreated ADSCs displayed a 2-fold increase in the average perfusion ratio to 0.56 compared to mice that received saline (**Figure 3.10C**). However, the average perfusion ratio of mice transplanted with untreated ADSCs remained the same at 0.51 through the following 3 weeks. The average perfusion ratio on Day 28 was similar to that of mice injected with saline. In contrast, the ADSCs tethered with TNFα-releasing HA-liposomes served to increase the average perfusion ratio to 0.70 within 7 days. The perfusion level remained stable at a value of 0.75 until the 28^{th} day.

We further quantified the mean walking stride length of the mice at Day 26 (**Figure 3.11A**). Mice treated with saline or untreated ADSCs had a similar stride length of 5.9 cm (**Figure 3.11B**). In contrast, mice treated with ADSCs tethered with TNFα-releasing HA-liposomes had a stride length of 6.8 cm that is similar to mice without vascular ligation surgery.[18–20]

After 28 days of recovery, the strength of the mice hindlimb muscles were evaluated by electrically stimulating the muscle fibers in the hindlimb and measuring the isometric contractions in vivo. There was no significant difference among the experimental groups where the mean maximum isometric torque was 383 N.mm kg^{-1} (**Figure 3.12A**). Similarly, there was no significant

difference in muscle fatigue where the mean percentage drop in muscle force was 50% (**Figure 3.12B**). On the other hand, there was a significant increase in gastrocnemius muscle mass by 1.2-folds (**Figure 3.12C**) in mice treated with TNFα-nanostimulated ADSCs.

3.3 Discussion

The results of this study demonstrated that a nano-sized liposome engineered to anchor to adipose-derived stem cells (ADSCs) and release TNFα is advantageous to enhancing therapeutic efficacy of stem cells to treat ischemic injury. Liposomes coated with HA-g-C18 showed an increased colloidal stability and association to the external membrane of ADSCs. Liposomes tethered to stem cells released TNFα and, in turn, stimulated cellular secretion of proangiogenic factors and immunomodulatory factors while reducing secretion of anti-angiogenic factors. As a consequence, ADSCs tethered with TNFα-releasing HA-liposomes were active to stimulate endothelial cells to form networks of endothelial tubes in vitro. Also, stem cells activated by the TNFα-releasing HA-liposomes served to recover perfusion in the ischemic hindlimb.

Peripheral arterial disease arising from the acute occlusion in the limb damages blood vessels and skeletal muscle.[21–23] Studies for last decades have focused solely on stimulating angiogenesis to recover perfusion in the injured tissue. Mesenchymal stem cells derived from bone marrow and adipose tissue have emerged as a rich depot of therapeutic cytokines and growth factors.[1,8,24] However, there are grand demands for stimulating cellular secretory activity sustainably. The optimal conditions using soluble factors developed under static in vitro cannot be replicated in vivo. Diffusion of stimulating factors would result in loss of activity over time. In order to maintain this, multiple administration at high doses of the soluble factor would be

required. Not only will multiple dosing cause undesired toxicity, patient compliance might be another obstacle.

To this end, we created a strategy to attach TNFα-releasing liposomes to the cells by coating the liposomes with HA-g-C18. HA binds with hyaluronan receptors of ADSCs, CD44 and CD168.[25] The binding between hyaluronic acid and CD44 is through hydrogen bonding as a mutation of the arginine residue within the binding domain causes nearly complete loss of hyaluronan-binding capacity.[26,27] The binding affinity of hyaluronic acid to CD44 depends on the molecular weight of hyaluronic acid. As a flexible polymer, hyaluronic acid forms a swollen random coil in dilute aqueous solution. For example, hyaluronic acid with a molecular weight of 100 kDa would have a radius of gyration of 21 nm.[28] The high affinity of hyaluronic acid with molecular weights greater than 100 kDa towards CD44 has been attributed to the capacity for a molecule of hyaluronic acid to bind to more than one CD44 receptor.[29,30] The multivalent interactions between multiple binding sites on HA-liposome and multiple receptors on the cell was shown to drastically increase in the binding stability. Therefore, the hyaluronic acid on the liposomal surface serves to increasing binding strength of nanoparticles to the cells.

To enhance binding of nanoparticles to cells, nanoparticles could be functionalized to present *N*-hydroxysuccinimides to react with the amine groups on the cell surface.[31] In these efforts, the resulting chemical bonds appear to provide a stable connection between the cells and the nanoparticle. However, this chemical reaction occurs on any proteins on the cell surface. Unless a thorough study to identify the proteins involved and evaluate the downstream effects, this new and long-lasting attachment might unintentionally affect other cellular functions even though the cells are still viable.[31] Therefore, we chose to utilize hyaluronic acid-CD44 bonds for tethering of nanoparticles to stem cells, although the bond strength may be weaker than the chemical bonds.

Another highlight of this study is the surface-tethering HA-liposomes function to stimulate ADSCs in a pseudo-autocrine mechanism. This strategy circumvents the dependency of endogenously produced TNFα to activate the ADSCs. Effective paracrine signalling in vivo requires close proximity to the cytokine-secreting cells such as T cells. While secreted cytokines diffuse and peak at about four cells away, the concentration is drastically diluted by diffusion in the three-dimensional tissue.[32] Of another importance is the continued release of TNFα from the liposomes that provided a sustained activation of ADSCs for secretory activity. TNFα Studies estimated that stimulated T cells secrete an average of 2 TNFα molecules per second but diminish over 12 hours.[33] Therefore, we propose that the tethered TNFα-releasing liposomes can reduce the proximity of TNFα to the TNF receptors and prolong the signal transduction needed for extending the reparative activity by ADSCs.

This study used a microfluidic system that allows us to co-culture endothelial cells and ADSCs and monitor neovascularization over five days. This analysis aims to examine the importance of the activation of ADSCs to stimulate vascularization in vitro. In particular, the microfluidic system is advantageous over the typical microwell plate assay, which relies on a basement membrane matrix that contains a small amount of growth factors capable of inducing premature tube formation. Also, endothelial tubes formed on the matrix detach and break apart quickly after 16 – 24 h which undermines a long-term evaluation of the role of stem cells on vascularization. In contrast, using the microfluidic system, we observed the stable formation of tubule networks likely due to the continued secretion of pro-angiogenic factors from ADSCs over five days. The aligned endothelial cells were interconnected and necessary for effective blood perfusion. In our system, the endothelial cells and ADSCs were spatially separated by a channel filled with media to mimic the initial spatial separation upon cell transplantation. Interestingly, the

vessel structures produced after five days were similar to that when endothelial cells were initially uniformly dispersed with bone marrow-derived mesenchymal stem cells (MSCs).[34] The presence of MSCs also stimulated the formation of longer and narrow microvessels. In comparison, the addition of anti-angiogenic factors resulted in disconnected networks. Thus, while ADSCs were also secreting anti-angiogenic factor PEDF, we observed that the effect of TNFα-releasing liposomes was overall pro-angiogenic.

This proximal delivery of TNFα to cell surface using the HA-liposome served to improve the efficacy of stem cells to treat ischemic hindlimb. Although the limb ischemia in humans and animal models elevate of levels of VEGF and other angiogenic cytokines, the elevated level is not sufficient or sustained for the full recovery in standpoints of perfusion and muscle strength.[35] Therapies focused solely on microvascular angiogenesis such as single growth factor deliveries also face similar obstacles and has led to efforts in combining multiple growth factors to augment angiogenesis.[36,37] We attribute the improved rate of perfusion recovery with the transplantation of stem cells tethered with HA-liposome releasing TNFα to the orchestration of pro-angiogenic factors, anti-apoptotic and immunomodulatory factors secreted by ADSCs. Specifically, the VEGF secreted by ADSCs sustainably would initiate the host endothelial cells to form blood vessel tubules. The PEDF secreted by cells over the course of recovery could facilitate stabilization of blood vessels to vascularize the ischemic limb. The host immune response to inflammatory cytokines at the ischemic injury is important for tissue recovery. However, the escalation of tissue damage by inflammation could be resisted by anti-apoptotic factors and immunomodulatory factors secreted by ADSCs.[38,39] The importance of the sustained generation of these factors was supported by the marked increase in perfusion within 7 days, in agreement to observations of greater number of collateral arteries from the continuous infusion of MCP-1.[40] Altogether, the

restoration of stable blood vessels supplied oxygen and nutrients to facilitate recovery of the hindlimb muscles.

3.4 Conclusions

In conclusion, we have demonstrated the in situ nanostimulation of adipose-derived stem cells for tissue repair in an ischemic limb. Nano-stimulation was accomplished with a hyaluronic acid-liposome and encapsulated TNFα as the soluble stimulus. TNFα-nanostimulators were prepared with adipose-derived stem cells by the cell surface association of hyaluronic acid and hyaluronan receptors in a cell suspension. This strategy allows the cells to be efficiently prepared for injection for cellular transplantation in vivo. This cell surface engineering strategy effectively stimulated adipose-derived stem cells to secrete protein factors for angiogenesis. The 3D microvascular device captured the engagement of TNFα-nanostimulated adipose-derived stem cells to induce endothelial cells to form blood vessel networks. TNFα-nanostimulation increased the rate of perfusion recovery and muscle regeneration characterized by increased muscle weight of the lower limb.

3.5 Experimental methods

3.5.1 Synthesis of HA-g-C18

Sodium hyaluronate (FMC BioPolymer) (100 mg, 0.25 mmol of –COOH) was dissolved in formamide (5 mL) by sonication for 30 min and gentle heating. After the solution was cooled to room temperature, two molar excess of 1-ethyl-3-(3-dimethylaminopropyl)carbodiimide hydrochloride (96 mg) and *N*-hydroxysuccinimide (58 mg) were added and stirred for 2 h to activate the carboxylic group. Then, octadecylamine (3.6 mg, 12.5 μmol) dissolved in anhydrous

DMF (1 mg mL^{-1}) was added slowly to the solution. To label hyaluronic acid (HA) with rhodamine B, lissamine rhodamine B ethylenediamine (1.6 mg dissolved in DMSO, 50 mg mL^{-1}; Invitrogen™) was added to the reaction mixture. Then, the reaction mixture was stirred at 60 °C under a nitrogen atmosphere for 5 h and an additional 24 h at room temperature. The resultant mixture was dialyzed against excess amount of water/ethanol for 2 days and distilled water for another 2 days. Finally, the solution was filtered with a 0.45 μm filter to remove other impurities, followed by lyophilization. The modified HA is referred to as HA-g-C18. To determine the degree of substitution by ^{1}H NMR analysis, HA-g-C18 was dissolved in deuterium oxide (Cambridge Isotope Laboratory) at a concentration of 10 mg mL^{-1}. ^{1}H NMR (500 MHz, D_2O, 22 °C): δ 3.3-4.0 (m, hyaluronic acid sugar backbone), 3.2 (m, $CH_2(CH_2)_{16}CH_3$), 2.9 (m, $CH_2(CH_2)_{16}CH_3$), 2.05 (s, -$COCH_3$ of hyaluronic acid), 0.85 (t, $CH_2(CH_2)_{16}CH_3$).

3.5.2 Liposome preparation

Liposomes were prepared by a film hydration method followed by vortex mixing and extrusion. 1,2-dipalmitoyl-*sn*-glycero-3-phosphocholine (DPPC; Avanti Polar Lipids) was dissolved in chloroform and placed in a round-bottom flask. Chloroform was removed by rotary evaporation to yield an evenly distributed film. The film was then hydrated with HA-g-C18 dissolved in deionized water (2 mg mL^{-1}) at 50 °C, which is above the transition temperature of DPPC. The lipid concentration was kept constant at 1 mg mL^{-1}. For experiments involving fluorescently-labeled liposomes, referred to as NBD-liposomes, 0.002 mg of 1-palmitoyl-2-{12-[(7-nitro-2-1,3-benzoxadiazol-4-yl)amino]dodecanoyl}-*sn*-glycero-3-phosphocholine) (Avanti Polar Lipids) was mixed with 1 mg of DPPC. The mixture was immediately vortexed for 30 s and extracted into a glass syringe. The liposomes were sized down by passing the liposome suspension 21 times through a 400 nm polycarbonate membrane assembled on the Avanti Mini Extruder. For

experiments involving encapsulation of TNFα, TNFα (GenScript, USA) was added to HA-g-C18 dissolved in cell culture media or PBS. The lipid film was then hydrated with the aqueous mixture of protein and HA-g-C18. Liposome diameters were measured using Zetasizer Nano ZS (Malvern Instrument Ltd) equipped with a He-Ne laser beam at 633 nm (Scattering angle: 173 °C). Each sample was measured three times, and an average diameter was obtained.

3.5.3 Analysis of liposome on cell surface

Adipose-derived stem cells (80,000 cells per group) were counted and suspended in cell culture media mixed with NBD-labeled liposomes. The cell density was kept constant at 1 million cells per mL of liposome suspension. The mixture was gently shaken at 37 °C for 15 minutes. After 15 minutes, the cells were centrifuged and washed once with PBS. The mass of liposomes tethered to the cell surface was quantified by measuring the liposome mass in the supernatant using a black 96-well plate reader (TECAN Infinite M200 Pro; Excitation wavelength: 460 nm, emission wavelength: 530 nm). Liposomes on the cell surface were also imaged using a confocal laser scanning microscope (Zeiss LSM 700). Cells were fixed with 3.7 % formaldehyde for 10 minutes before imaging. Confocal microscopy was carried out with excitation at 488 nm. Emission above 530 nm and brightfield images were collected.

3.5.4 Kinetic analysis of liposome tethering to ADSC surface

ADSCs (240,000 cells per group) were mixed with varying concentrations of liposomes labeled with NBD (i.e., 0.1, 0.2, 0.5, 1 mg/mL DPPC). Cell density in the suspension was kept constant at 1 million cells per mL of liposome suspension. The mixture was incubated for 15 min at 37ºC. The excess liposomes in the suspension were removed by centrifuging the cells and replacing the supernatant with fresh media. The number of liposomes in the supernatant was

measured using a microplate reader with a fluorescence setup. To determine the dissociation rate constant, the cell suspension was centrifuged at 5, 10, 15 and 30 min after the replacement with fresh media. Then, the number of liposomes dissociated from the cells was counted using with a calibration curve of fluorescence intensity against number of liposomes labeled with NBD in media.

3.5.5 Cellular internalization of liposomes coated with HA-g-C18

To determine the uptake of surface-tethered liposomes, liposomes were coated with rhodamine B-labeled HA-g-C18. ADSCs were mixed with rhodamine B-labeled liposomes at 1 million cells per mL of liposome suspension. The mixture was incubated for 15 min at 37ºC. The excess liposomes in the suspension were removed by centrifuging the cells and replacing the supernatant with fresh media containing LysoTracker® Green DND-26 (50 nM) to label the endolysosomes and Hoechst 33342 to label the nuclei. The cells were incubated for 30 min at 37 °C before imaging with a confocal laser scanning microscope (Zeiss LSM 700).

3.5.6 Kinetic release of TNFα from liposomes

Liposomes were suspended in PBS at 1 mg mL^{-1} and placed in a cellulose ester dialysis membrane with molecular weight cut-off of 100,000 Da. The bag was submerged into a bottle containing 10 mL PBS (pH 7.4) and placed on a rotary shaker in a 37 °C incubator. At designated intervals (4, 8, 24 h, 2, 3, 4, 5 days), 1 mL of release media was collected and replaced with 1 mL of fresh buffer. TNFα in the release media was measured using an enzyme-linked immunosorbent assay (R&D Systems, USA).

3.5.7 Analysis of secretion activity from ADSCs

Collagen hydrogels were prepared in a sterile condition. First, 200 μL of type I bovine collagen solution (3 mg mL^{-1} in 0.01 N hydrochloric acid; Advanced BioMatrix) was mixed with 100 μL of culture media. The mixture was pipetted until the phenol red changed from red to yellow. Care was taken to avoid the formation of air bubbles. Then, 25 μL of reconstituting solution (0.26 M sodium bicarbonate, 0.2 M HEPES, 0.04 N NaOH) was gently mixed with the collagen solution until the phenol red changed from yellow to pink. The pre-gel solution was quickly transferred to a pre-cooled 96 well plate and incubated at 37 °C for 3 h.

To tether liposomes to the adipose-derived stem cells (ADSCs, Lonza), 160,000 ADSCs per group were counted and mixed with liposomes by gently shaking at 37 °C for 15 minutes. After 15 minutes, the cells were centrifuged (200 × g, 5 min) and re-suspended in fresh media to a concentration of 100,000 cell mL^{-1}. Then, 100 μL of cell suspension was added on to the pre-made collagen hydrogels. Cell culture media was collected after 24 h and 5 days.

A proteome profiler human angiogenesis array kit (R&D Systems, USA) was used to analyze the proteins in the cell culture media following the manufacturer protocol. Briefly, 400 μL of cell culture supernatant was pooled (n = 5) and diluted with a cocktail of biotinylated antibodies. The mixture was then applied to a membrane pre-coated with multiple capture antibodies printed in duplicate. Samples were incubated at 4 °C overnight on a rotating shaker. Following multiple washes, a horseradish peroxidase-conjugated streptavidin conjugate was applied for 30 min. Blots were detected from the oxidation of luminol and the emitted light was captured by exposure to X-ray films.

Separately, the amount of VEGF and PDEF were measured using DuoSet® enzyme-linked immunosorbent assay development system (R&D Systems, USA). Briefly, 96-well microplates were coated with the capture antibody diluted in PBS. The plates were incubated overnight at room temperature. Free binding sites were blocked with 0.1% bovine serum albumin (BSA) in PBS. 100 μL of samples or standards were added to each well. After incubation for 2 h at room temperature, biotinylated detection antibody was added, followed by addition of streptavidin-horseradish peroxidase. The plate was washed before each step with 0.05% Tween 20 in PBS. A substrate solution consisting of an equal mixture of Color Reagent A containing H_2O_2 and Color Reagent B containing tetramethylbenzidine (R&D Systems) was added and incubated for 20 min at room temperature. The color development was terminated by the addition of 50 μL of 2 N H_2SO_4. The color intensity was measured immediately using a microplate reader (Tecan M200 Pro) set at 450 nm (with background correction wavelength set to 570 nm).

3.5.8 Microfluidic chip angiogenesis assay

A fibrinogen solution was prepared by dissolving 2.5 mg ml^{-1} bovine fibrinogen in Dulbecco's phosphate-buffered saline supplemented with aprotinin (0.15 U ml^{-1}, Sigma, A1153) to the solution. Human umbilical vein endothelial cells (HUVECs, Lonza) and ADSCs were suspended in the fibrinogen solution, at a concentration of 2 or 3×10^6 cells ml^{-1} for HUVECs and 5×10^6 cells ml^{-1} for ADSCs. The cell suspensions were mixed with thrombin (0.5 U ml^{-1}) and then immediately introduced into a central HUVEC culture channel and ADSC culture channels located on both sides. The cell-suspended gel constructs were allowed to crosslink for 5 min at room temperature. To fill the hydrophobic channels, the inlet reservoirs of the cell culture medium channels were loaded with EGM-2, and vacuum was applied at the outlet reservoirs. Following

the loading of all four reservoirs, the microfluidic platforms were incubated at 37℃ and 5% CO_2. The cell culture medium was removed and refilled with fresh EGM-2 culture medium every 24 h.

After 5 days, cells were washed once with PBS and fixed in 4% (w/v) paraformaldehyde-PBS mixture for 15 min, and then permeabilized using a 0.15% Triton X-100 in PBS solution for 15 min. After blocking with 3% BSA in PBS for 1 h, samples were incubated overnight at 4℃ with CD31 primary antibodies directly conjugated with fluorescent marker (1:200). The cell nuclei were stained with Hoechst 33342 (1:1000) for 1 h at room temperature. The chips were washed three times and stored in PBS before imaging. Quantification of tubule length was conducted using ImageJ software.

3.5.9 Induction of ischemic hindlimb injury and laser Doppler perfusion imaging analysis

The surgery to induce hindlimb ischemia was performed in accordance with the protocol approved by the Illinois Institutional Animal Care and Use Committee. The animals used were 7-week old female CD1 mice (Charles River). Under anaesthesia, two sections of femoral artery, 5 mm apart, on the right limb were tied with 5-0 Ethilon sutures. Then, the middle section was cut before the surgical site was closed with 5-0 Ethilon sutures. ADSCs (1.0×10^6 cells per mouse) were suspended in 100 µL PBS and injected intramuscularly at two sites (60 µL to the quadriceps and 40 µL the tibialis anterior) using 28-gauge insulin syringes 1 h after the surgery. The overall perfusion recovery rate in the hindlimb was monitored by Laser Doppler Perfusion Imaging (LDPI) of the whole leg after 1, 3, 7, 14, 21 and 28 days post-cell transplantation. Prior to imaging, the fur on the legs and lower abdomen was shaved. Scans of the ischemic and non-ischemic limbs were taken while the mice were placed on a 37 °C heating pad to control the body temperature. 7-8 mice were analysed per condition. On Day 26, the stride length of recovering mice were

measured using a previously described method.[18–20] The forepaws and hindpaws of the mice were dipped in green and red non-toxic inkpads, respectively. The mice were trained to walk along a 50-cm-long, 12-cm-wide, paper-covered runway. The stride length was determined by measuring the distance between two hindpaw prints.

3.5.10 Muscle function and histological analysis

The strength of the hindlimb muscles were assessed in vivo after 28 days. Under anesthesia with isoflurane gas, the mouse hindlimb was placed on the foot pedal and the sciatic nerve was electrically stimulated at 100 Hz. The maximal isometric force was collected with a servomotor and analog control unit (model 305C-LR, Aurora Scientific, Canada). The maximal force output was presented as torque from an individual mouse and normalized to the mass of the corresponding mouse. To assess the ability of the muscle to generate the maximal force after multiple contractions, the electrical stimulation was repeated for an additional 9 times with 5 s recovery periods. Then, the muscle fatigue was represented by the percentage drop in muscle force. This was calculated by subtracting the value from the first stimulation from the last stimulation and dividing by the value from the first stimulation.

Immediately after the measurements, the mice were sacrificed, and the quadriceps and gastrocnemius muscle were gently dissociated from underlying bone. Muscle weight were measured before they were immediately frozen in precooled isopentane.

3.5.11 Statistical Analysis

Three samples were analyzed per condition and the data were presented as mean ± standard deviation unless otherwise specified. To determine significance, comparisons between groups were performed by one-way ANOVA followed by Tukey's post hoc analyses. Student's t-tests

with unequal or equal variance were used to compare differences between two experimental groups. Data were considered significant for p values less than 0.05.

3.6 Scheme, Figures and Equations

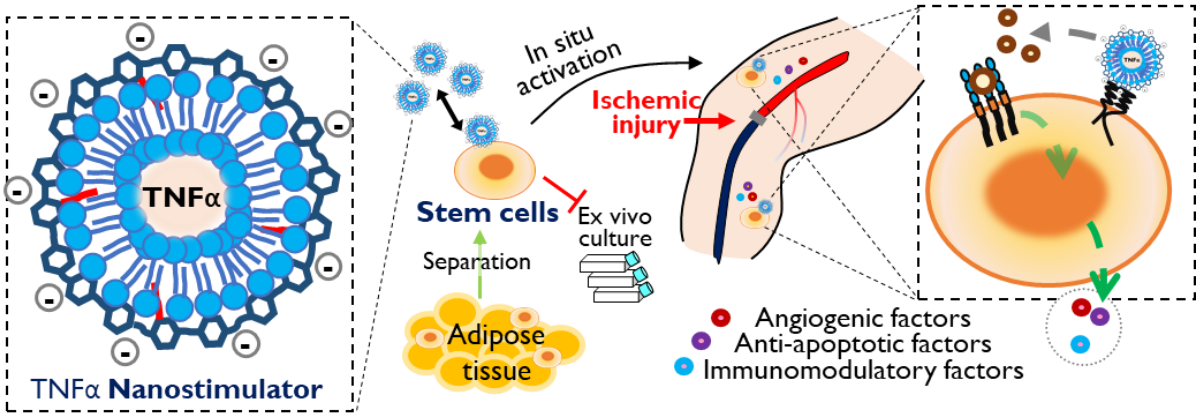

Scheme 3.1. In situ stimulation of adipose-derived stem cells (ADSCs) for cellular therapy in ischemic tissue recovery. Nanostimulator consists of TNFα-releasing liposome coated with hyaluronic acid-graft-octadecylamine (HA-g-C18). HA tethers the liposomes to stem cell surface via specific binding with CD44. The nanostimulator on the stem cell surface up-regulates cellular secretion levels of angiogenic and immunomodulatory factors for revascularization and the prevention of muscle damage. Also, the nanostimulator removes ex vivo culture for pre-conditioning of stem cells, thus allowing for isolation and injection in an operation room.

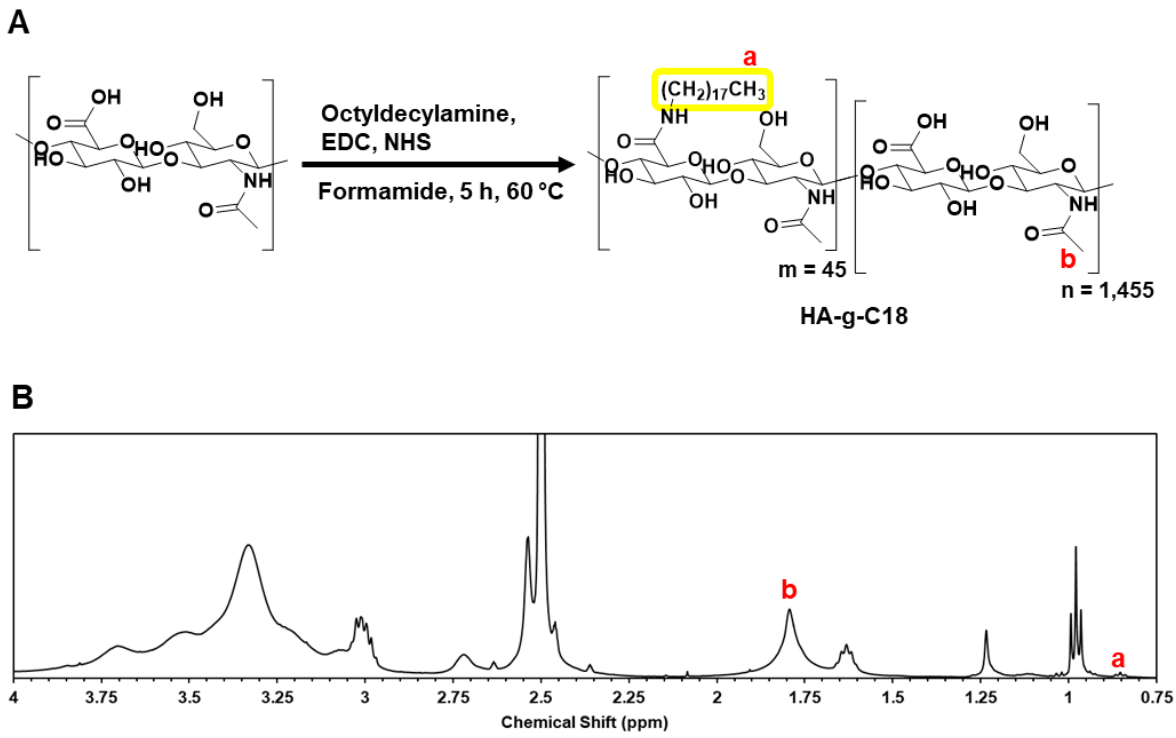

Figure 3.1. Synthesis and characterization of hyaluronic acid-graft-octyldecylamine. (a) Synthesis of HA-g-C18 formed by amide coupling between the uronic acid groups on hyaluronic acid and amine group of octadecylamine. (b) NMR spectrum of hyaluronic acid before (i) and after (ii) grafting of octydecyl chains.

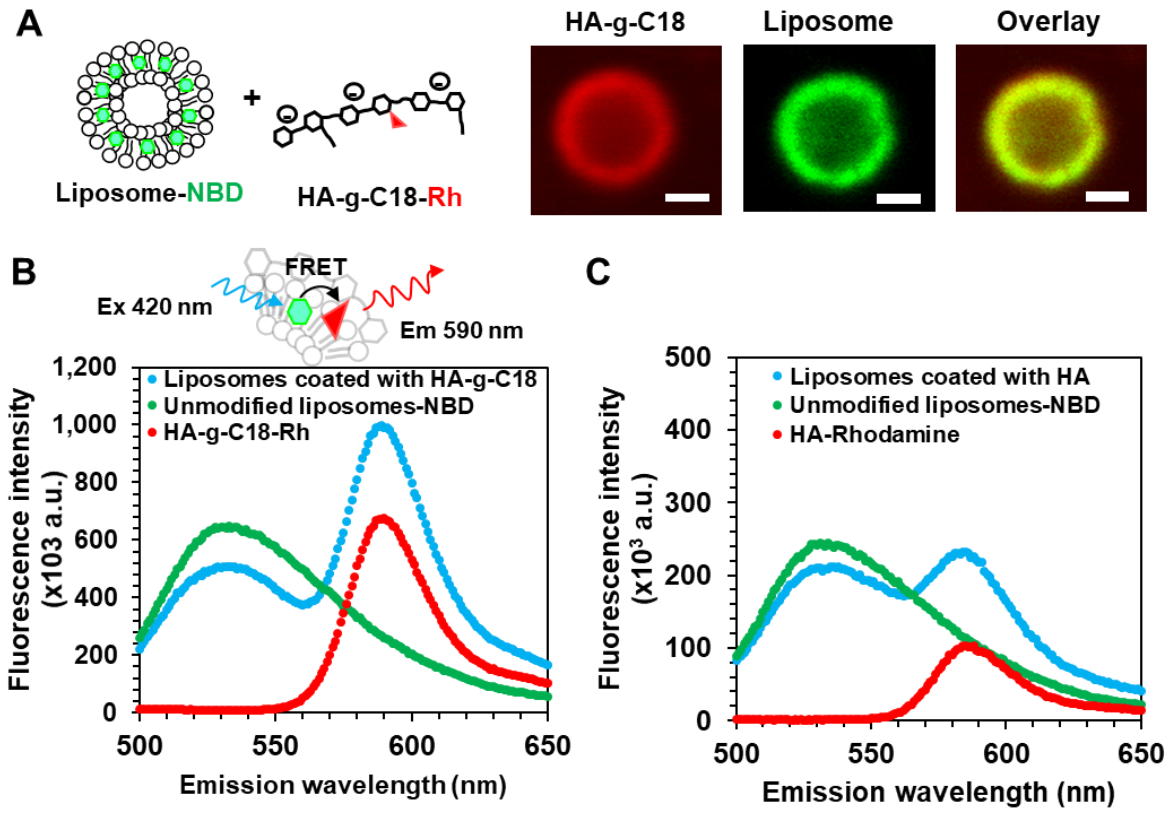

Figure 3.2. Spatial location of hyaluronic acid-g-C18 (HA-g-C18) on liposomes. (A) Fluorescent images of HA-g-C18 liposomes where HA-g-C18 were labelled with rhodamine (in red) and the lipid layer was labelled with nitrobenzoxadiazole (NBD) (in green). The overlay panel shows the merged images. Images were taken with mass ratio of HA-g-C18 to lipid ratio of 2:1. Scale bar represent 1 μm. Förster resonance energy transfer (FRET) assay to evaluate the association between (B) HA-g-C18 or (C) HA and liposomes. All three samples were excited at wavelength of 460 nm.

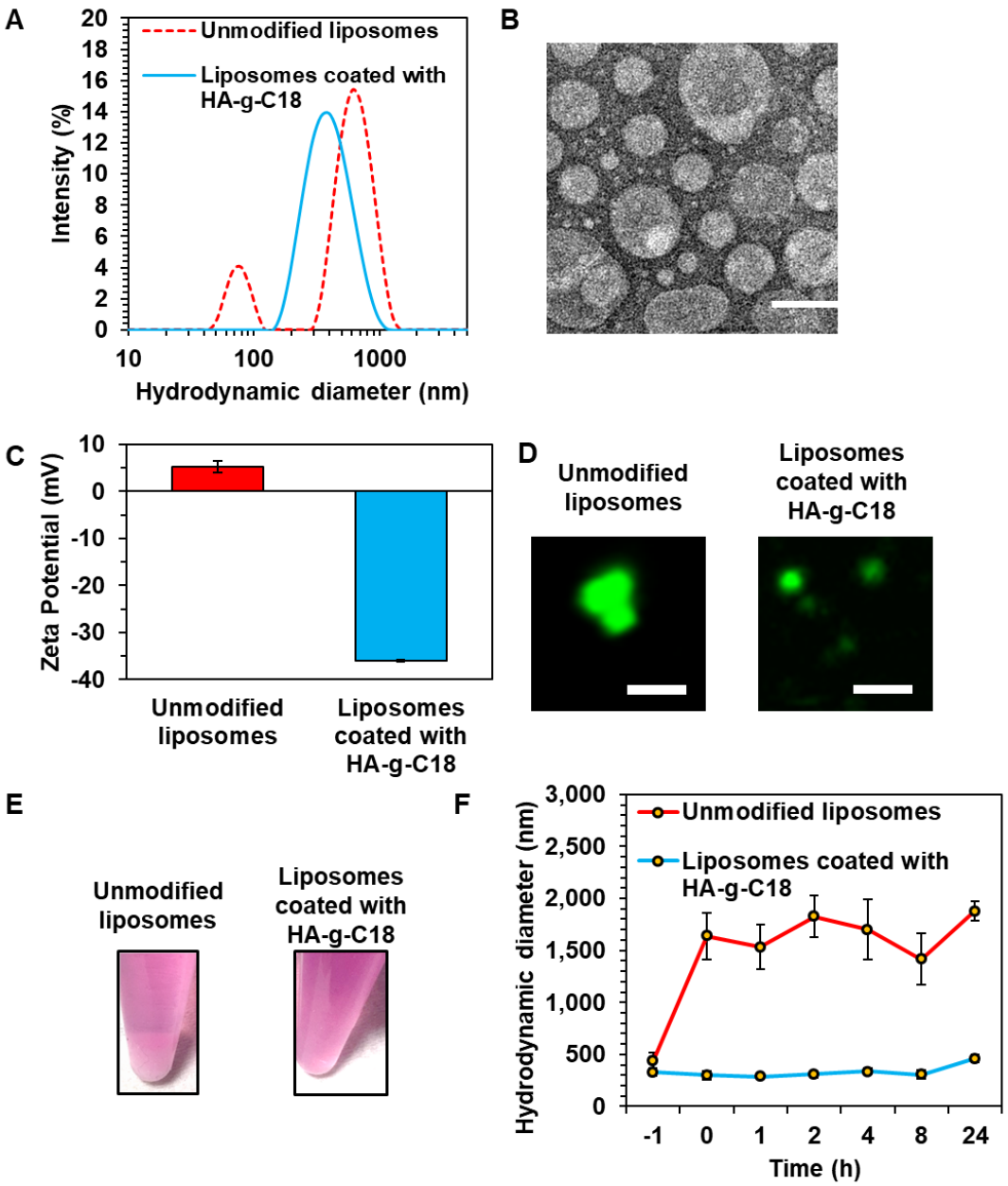

Figure 3.3. Physical characterization of hyaluronic acid-g-C18 (HA-g-C18) liposomes. (A) Hydrodynamic diameter of unmodified liposomes (in red) and liposomes coated with HA-g-C18 (in blue) in PBS. (B) TEM micrograph of liposomes coated with HA-g-C18. Scale bar represents 100 nm. (C) Zeta potential of unmodified liposomes and liposomes coated with HA-g-C18 in deionized water. (D) Confocal microscope images of unmodified liposomes and liposomes coated with HA-g-C18 after 4 h in media supplemented with 10% serum. Scale bar represents 1 μm. Liposomes were fluorescently-labelled with nitrobenzoxadiazole. (E) Photographs of unmodified liposomes and liposomes coated with HA-g-C18 after 4 h in media supplemented with 10% serum. (F) Hydrodynamic diameter of liposomes with (in blue) and without HA-g-C18 (in red) incubated in media supplemented with 10% serum at 37 °C. Data points represent the mean and error bars represent standard deviations (N = 3, $p < 0.05$).

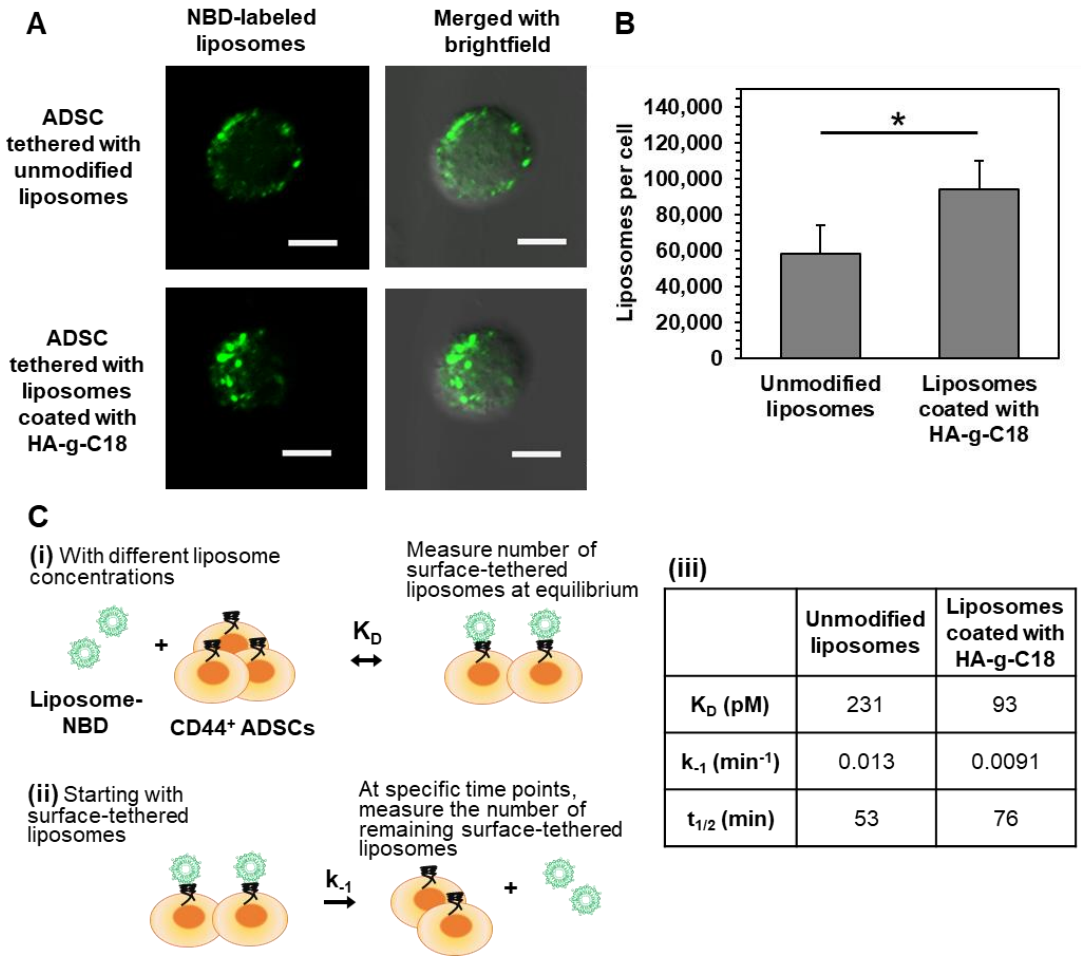

	Unmodified liposomes	Liposomes coated with HA-g-C18
K_D (pM)	231	93
k_{-1} (min^{-1})	0.013	0.0091
$t_{1/2}$ (min)	53	76

Figure 3.4. Characterization of the association of liposomes with ADSCs. (A) Confocal microscope images of ADSCs after incubation with unmodified liposomes or liposomes coated with HA-g-C18. Liposomes were fluorescently-labeled using the covalently-bound NBD fluorophore (in green). Scale bar represents 10 µm. (B) Quantification of the number of liposomes on the surface of ADSCs. Data points represent the mean and error bars represent standard deviations. N=3, * represents the statistical significance in the number of liposomes between the unmodified liposomes and liposomes coated with HA-g-C18. *$p < 0.05$. (C) Schematic illustration of the kinetic analysis of the liposome tethering to ADSCs. (i) At a given liposome concentration, the number of liposomes tethered to cells was measured to quantify the dissociation equilibrium constant, K_D; (ii) The dissociation rate constant, k_{-1} and the half-time of liposome dissociation $t_{1/2}$, the number of remaining surface-tethered liposomes were measured by counting the liposomes detached from cells at different time points. (iii) Tabulation of K_D, k_{-1} and $t_{1/2}$ of unmodified liposomes and liposomes coated with HA-g-C18.

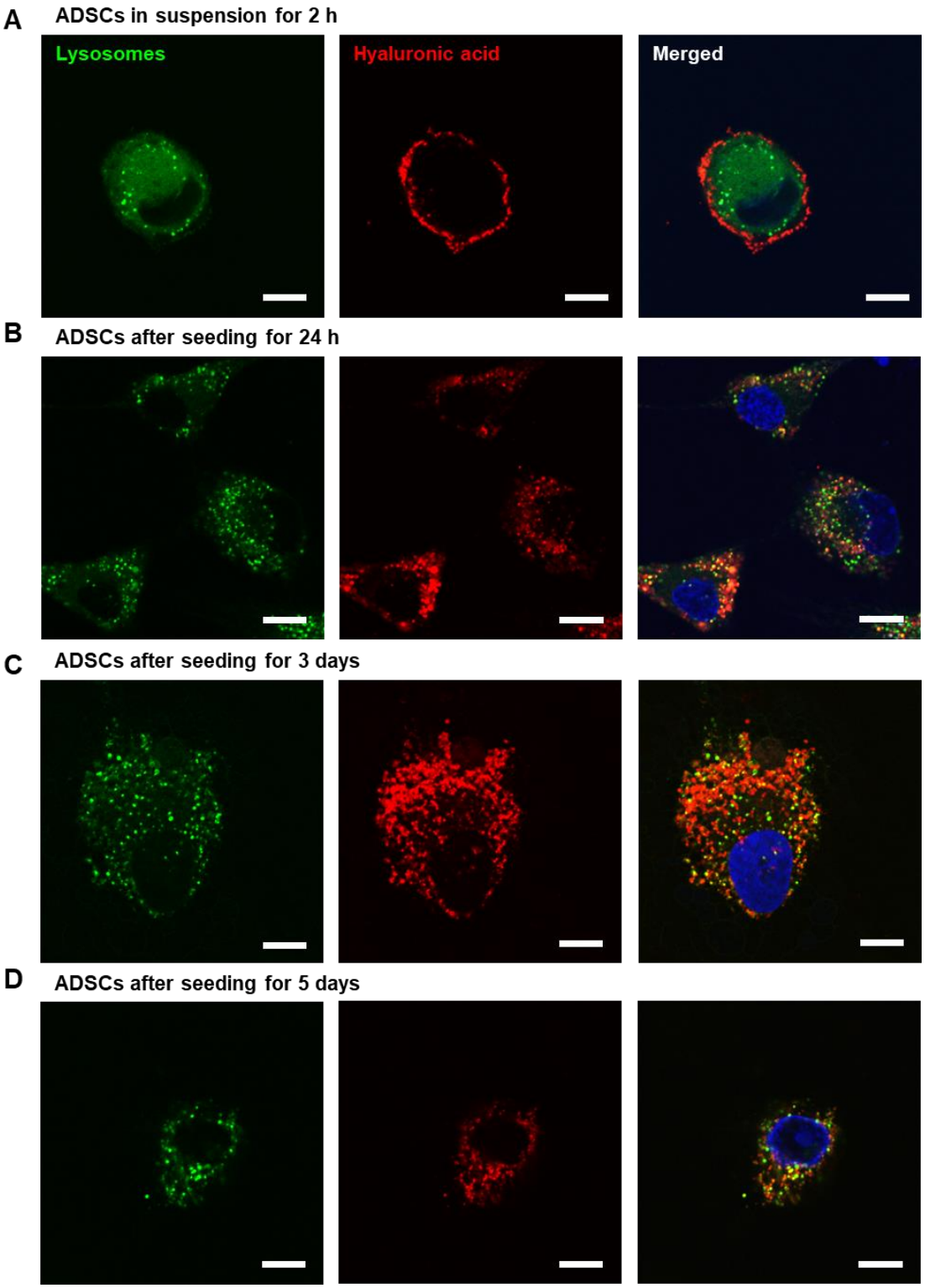

Figure 3.5. Analysis to determine cellular internalization of liposomes coated with HA-g-C18. Lysosomes were labelled with LysoTracker Green while liposomes were labelled with rhodamine B-conjugated HA-g-C18 (red). (A) ADSCs were incubated in suspension for 2 h. (B) ADSCs were incubated on type I collagen hydrogels for 24 h, (C) 3 days and (D) 5 days. The 3rd column shows the merged images of the first two columns. Scale bars represent 10 µm.

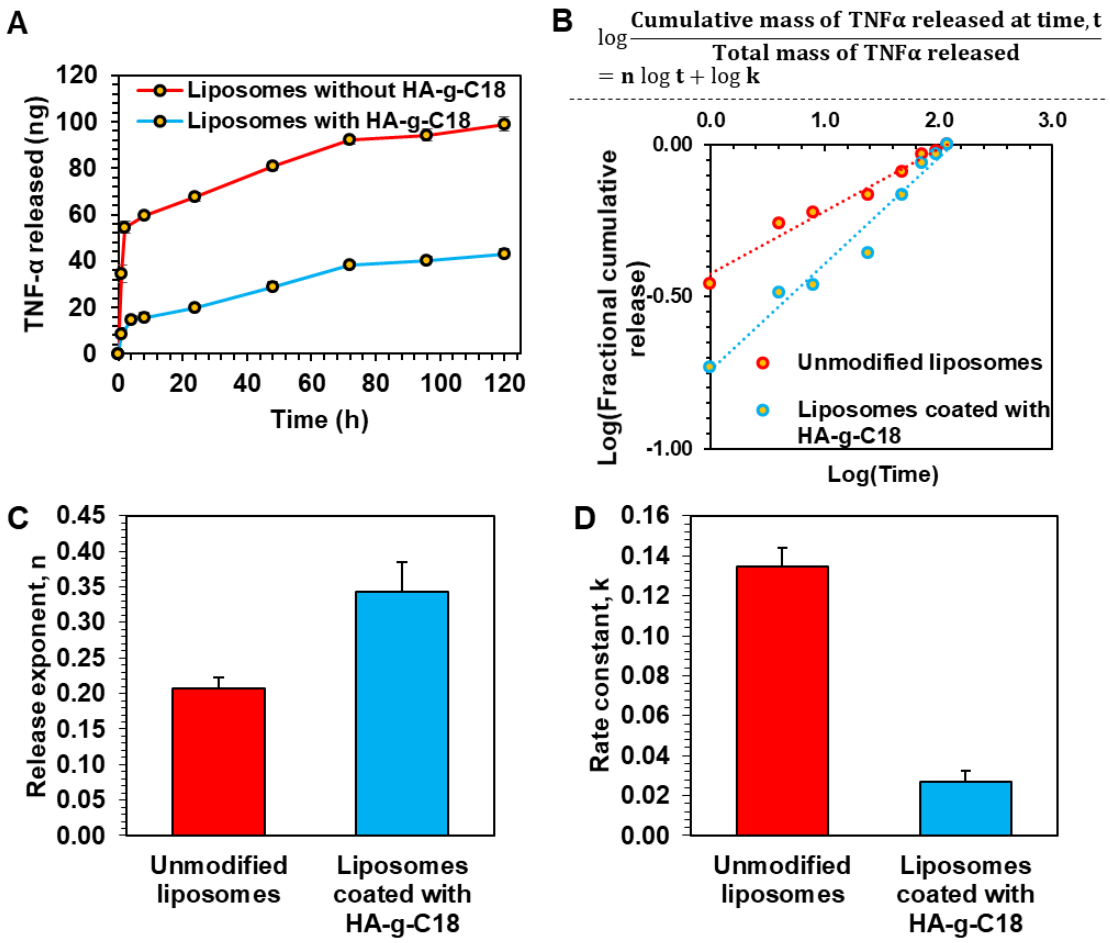

Figure 3.6. Characterization of TNFα-loaded liposomes. (A) Cumulative release of TNFα protein molecules from unmodified liposomes (in red) and liposomes coated with HA-g-C18 (in blue) after incubation at 37 °C. The released proteins were quantified using ELISA. Data points represent the mean and error bars represent standard deviations. N = 3. (B) TNFα release profile from unmodified liposomes (in red) and liposomes coated with HA-g-C18 (in blue) against the empirical model for TNFα transport from liposomes. *n* represents the release exponent (C), and *k* represents the release rate constant (D). For spherical liposomes, $n \leq 0.43$ corresponds to Fickian diffusion, $0.43 < n < 1.00$ corresponds to non-Fickian transport, $n = 1.00$ corresponds to zero-order release.

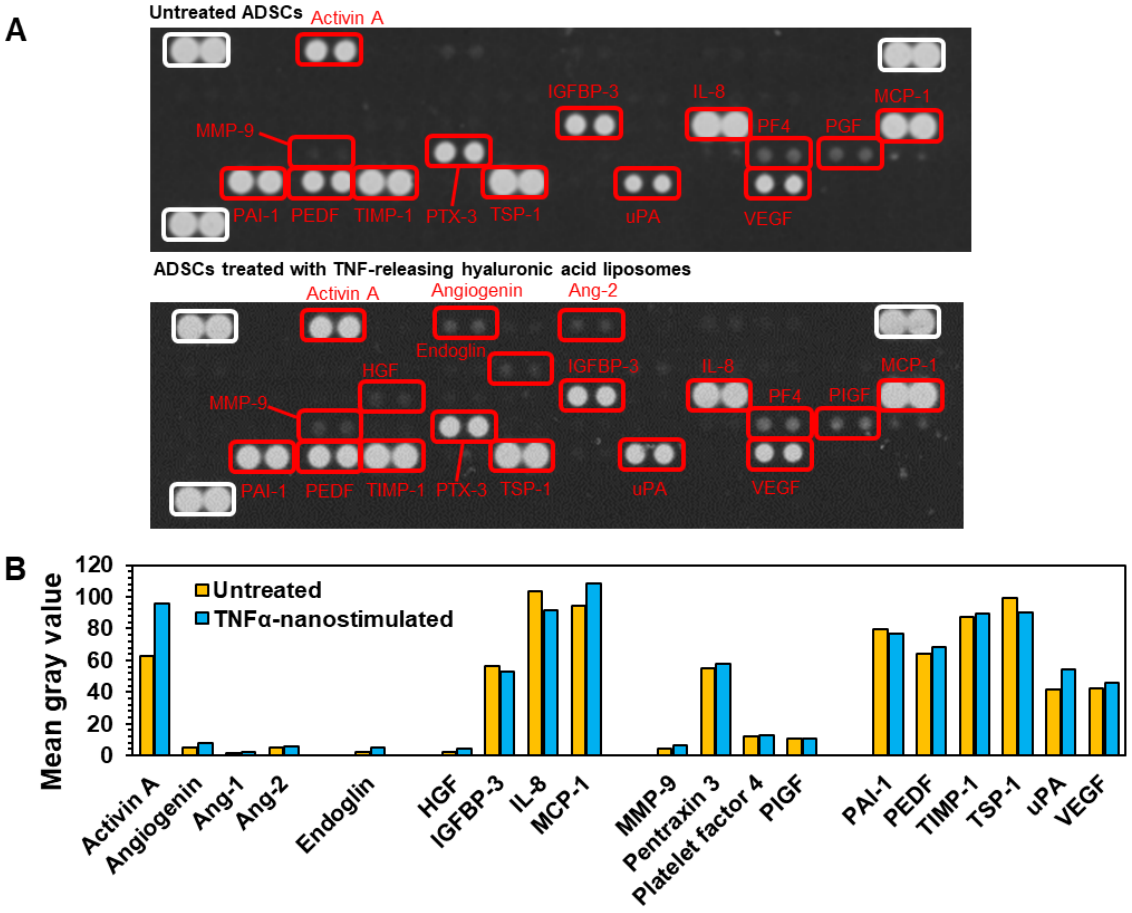

Figure 3.7. Analysis of the secretory activity of ADSCs using the angiogenesis antibody array. (A) Images of angiogenesis antibody array membrane incubated with media from the ADSC culture after 24 h. Both untreated ADSCs and ADSCs tethered with TNFα-releasing HA-liposomes secrete growth factors and cytokines involved in pro-angiogenesis, anti-angiogenesis, fibrosis, anti-apoptosis, and tissue remodeling. (B) Quantification of the signal intensities of the spots in duplicates.

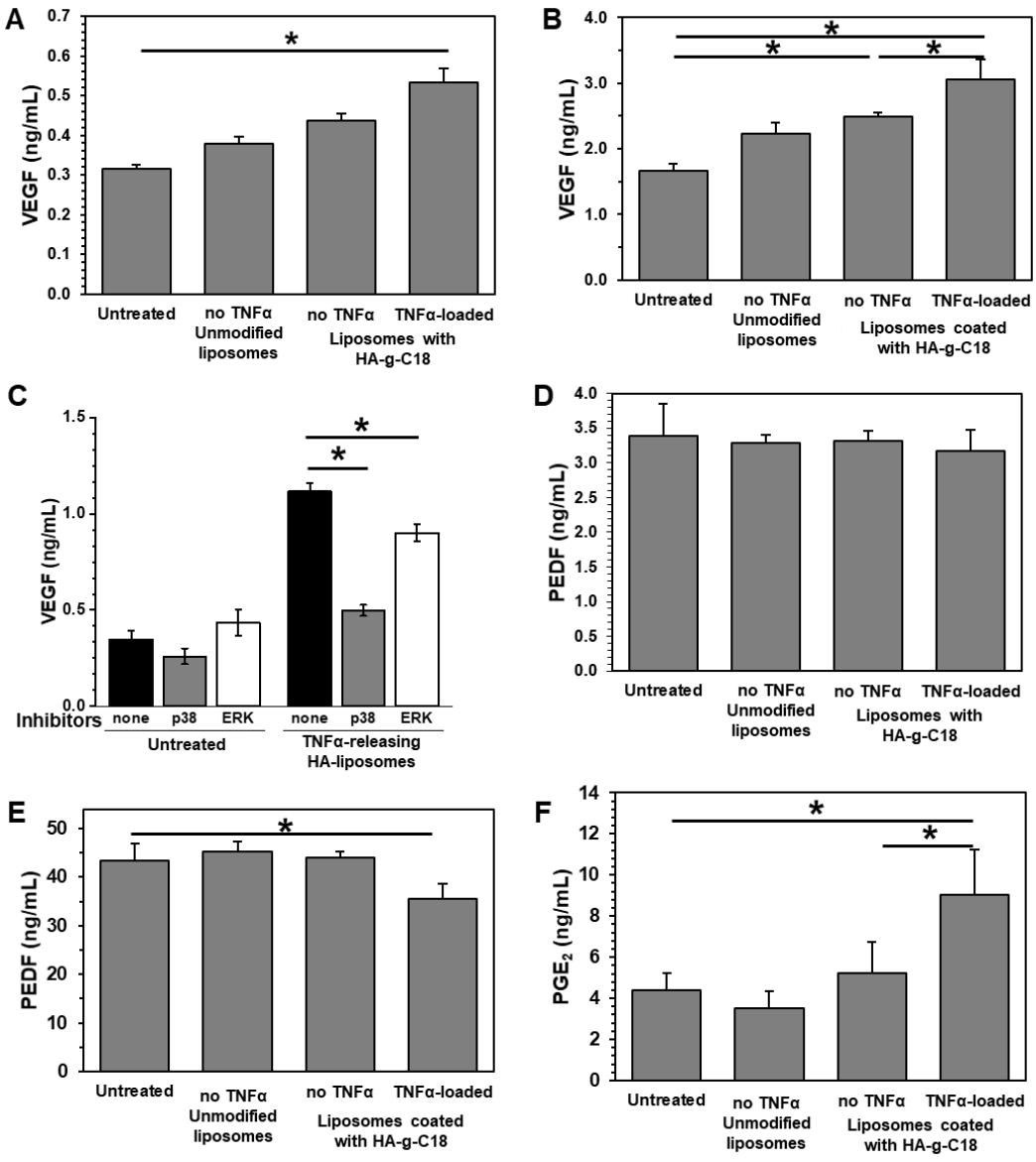

Figure 3.8. Quantification of pro-angiogenic VEGF, anti-angiogenic PEDF, and immunomodulatory PGE_2 levels secreted by ADSCs using ELISA. VEGF secretion level after (A) 24 h and (B) 5 days. (C) Amount of VEGF in the media cultured with untreated ADSCs and ADSCs tethered with TNFα-releasing HA-liposomes after 24 h incubation in the absence or presence of p38 MAPK or ERK inhibitors. PEDF secretion level after (D) 24 h and (E) 5 days. (F) PGE_2 secretion level after 48 h. Data points represent the mean and error bars represent standard deviations. N = 3, * represents the statistical significance between the conditions indicated. $p < 0.05$.

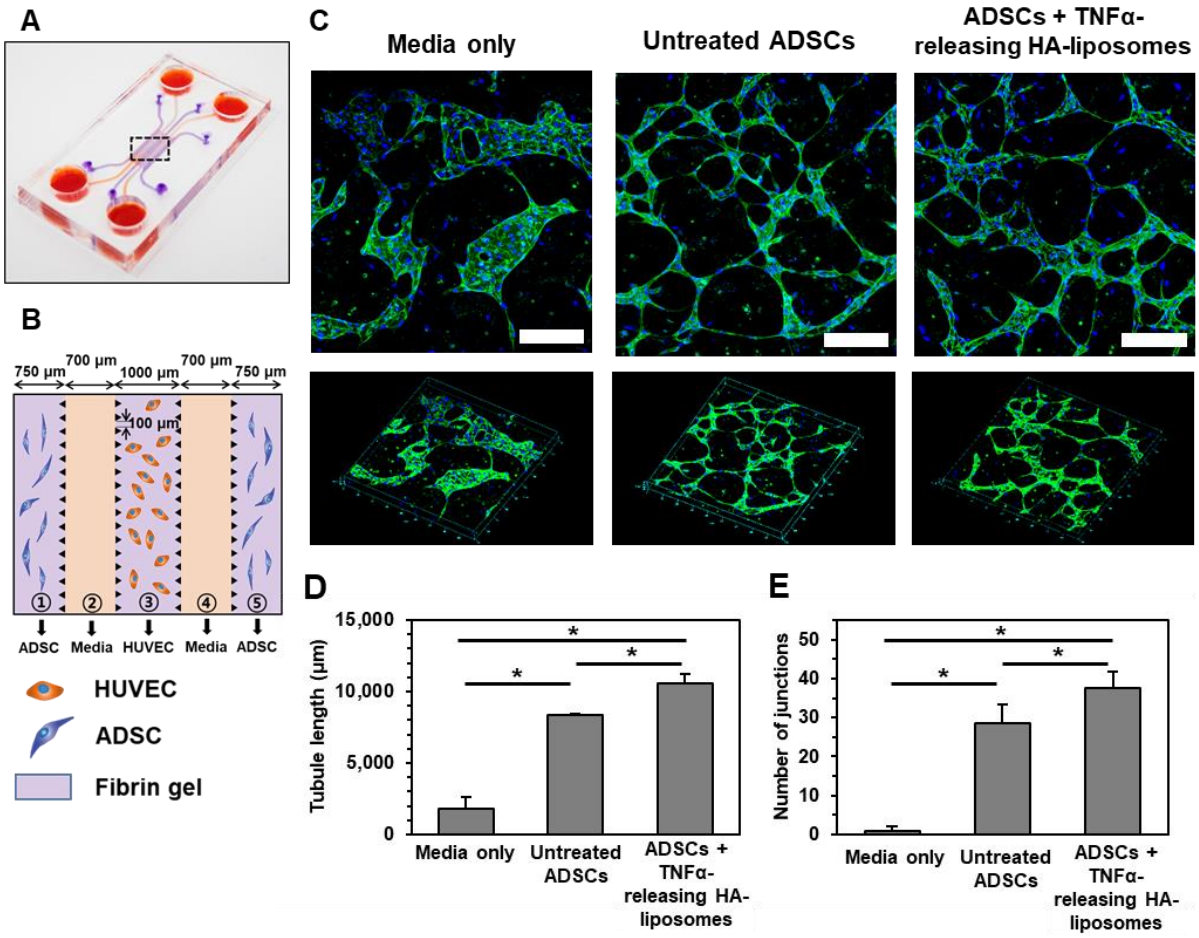

Figure 3.9. In vitro angiogenesis assay with a 3D microvascular device. (A) Schematic illustration of the device fabricated with polydimethylsiloxane using soft lithography. (B) The central portion features 5 channels. ADSCs in fibrin gels were seeded in the outer channels ① and ⑤; cell culture medium was filled in channels ② and ④; and HUVECs in the fibrin gel were seeded in the center channel ③. (C) Confocal laser scanning microscope images of immunostained HUVECs with CD31 (in green) in channel ③ after 5 days incubation with the cell culture media only, with untreated ADSCs only or ADSCs tethered with TNFα-releasing HA-liposomes. Cell nuclei were stained with Hoechst dye (in blue). Scale bar represents 200 μm. The lower panels display an overview of the selected region. (D) Quantification of the tubule length and (E) the number of interconnected junctions. Data points represent the mean and error bars represent standard deviations. N=3, * represents the statistical significant between the conditions indicated. *$p < 0.05$. *Data was provided by Kyeongsoo Kim.*

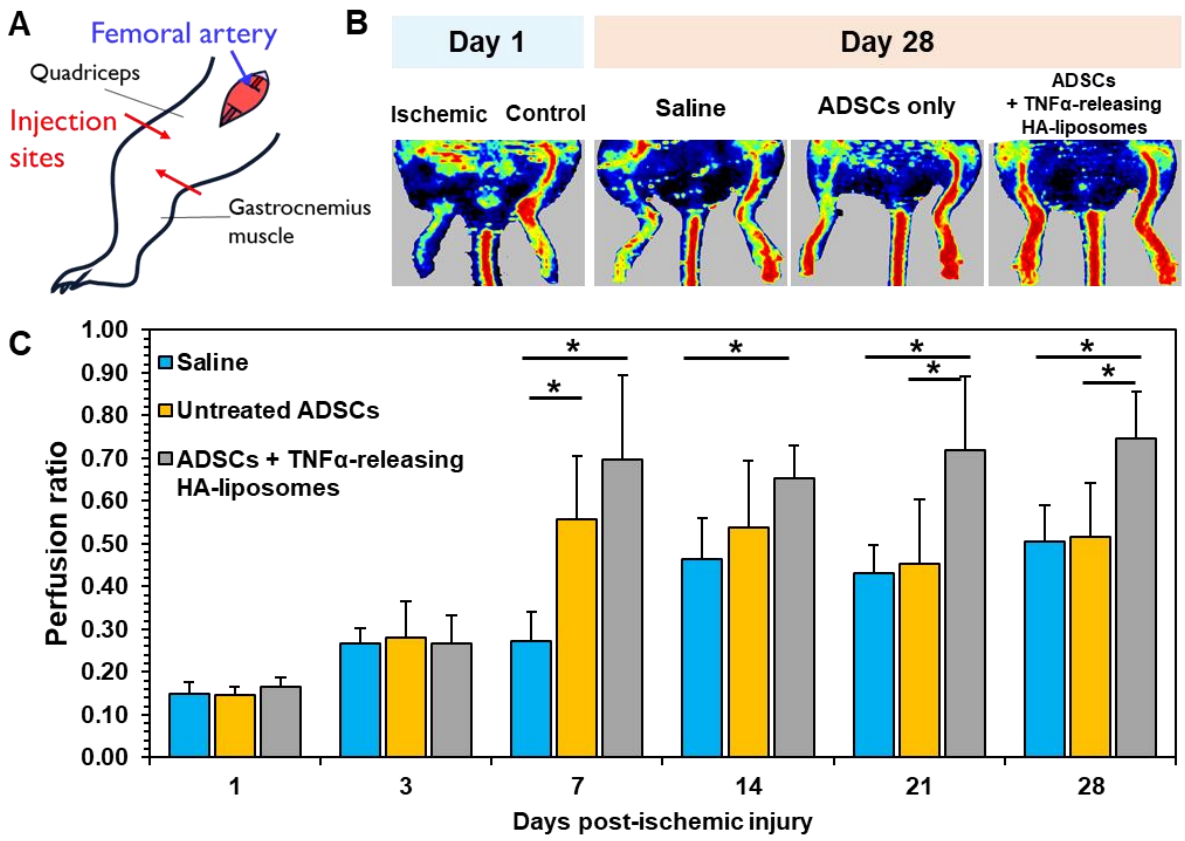

Figure 3.10. Laser Doppler perfusion imaging (LDPI) of mice induced with ischemic hindlimb injury. (A) Illustration of the femoral artery ligation. Red arrows indicate the sites where the cells were transplanted by intramuscular injections into the quadriceps and calf muscles. (B) LDPI images of mice 1 day and 28 days after the ischemic hindlimb surgery. Ischemia was introduced by ligating the femoral artery. The red color intensity represents the highest intensity of perfusion. Mice treated with ADSCs received 1 million untreated ADSCs or 1 million ADSCs tethered with TNFα-releasing HA-liposomes per mouse. (B) Quantification of the average perfusion ratio defined as the perfusion in the ischemic limb divided by the perfusion in the non-ischemic limb. Data points represent the mean and error bars indicate standard deviations. N = 7-8 mice, * represents the statistical significance between the conditions indicated. $p < 0.05$.

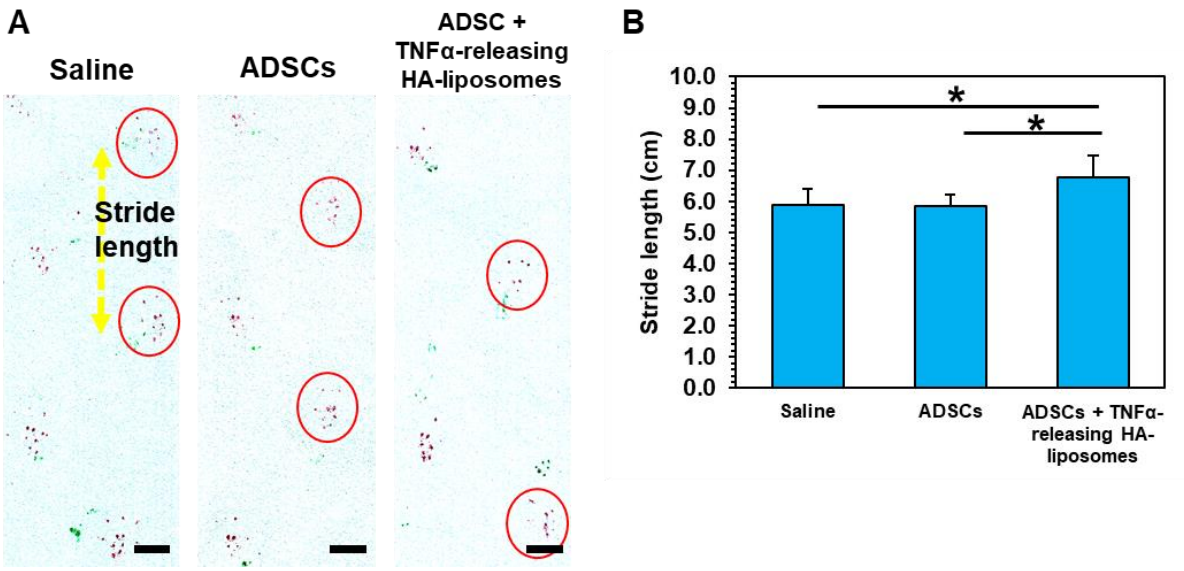

Figure 3.11. Gait analysis of recovered mice on Day 26. (A) Footprints of mice treated with PBS only, ADSCs only or ADSCs with TNFα-loaded in HA-g-C18 liposomes. Forepaws and hindpaws were dipped in green and red ink, respectively. Images were treated for higher image contrast of the red ink. Scale bar represents 2 cm. (B) Quantification of the average stride length. Data points represent the mean and error bars indicate standard deviations (N = 7-8 mice, $p < 0.05$).

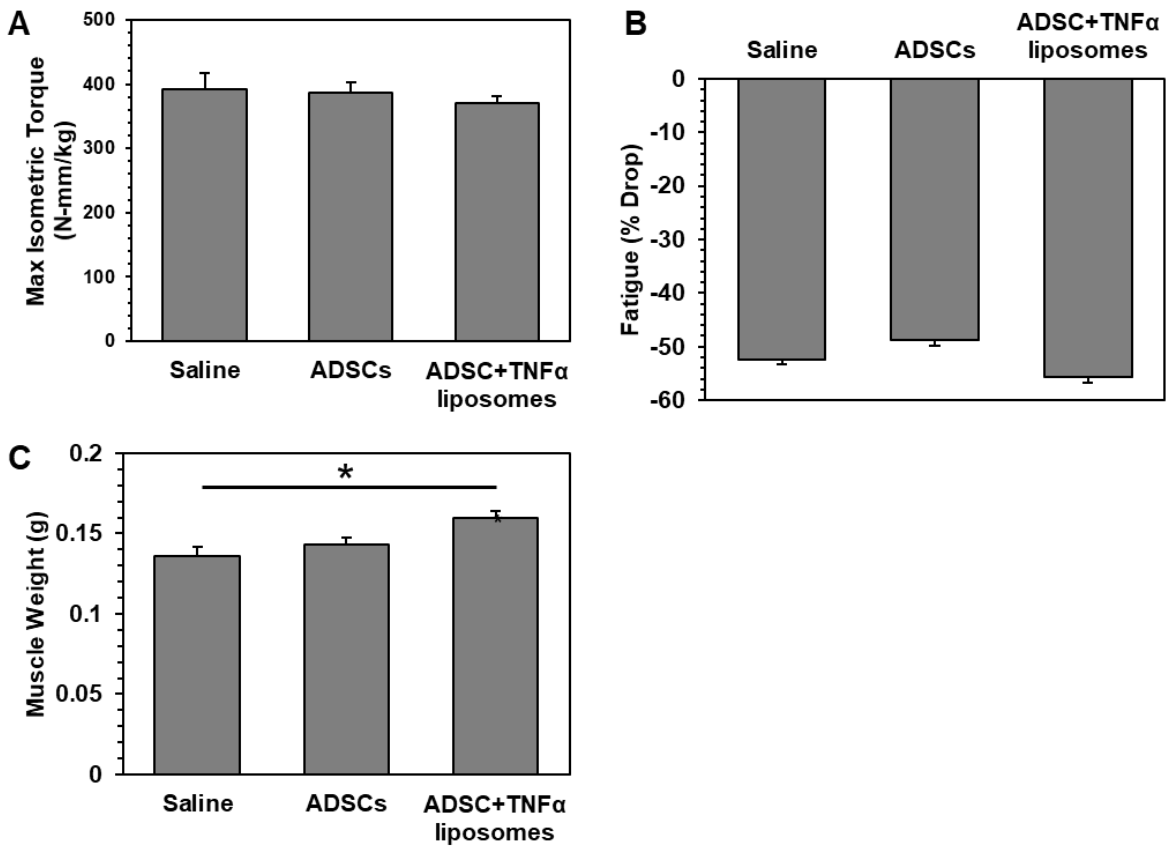

Figure 3.12. Assessment of the muscles in the limb after 28 days of recovery from ischemic injury and cellular transplantation with ADSCs only or ADSCs with TNFα-loaded in HA-g-C18 liposomes. (A) Maximal isometric torque measured from an electrical stimulation at 100 Hz. (B) Muscle fatigue was determined by the difference in muscle force from the first stimulation and muscle force after the electrical stimulation was repeated for an additional 9 times. (C) Weight of the recovered gastrocnemius muscle. Data points represent the mean and error bars indicate standard deviations (N = 7-8 mice, $p < 0.05$). *Data was provided by Svyatoslav Dvoretskiy.*

Equation 3.1

$$\text{FRET Efficiency} = 1 - \frac{\text{Intensity of modified liposomes with HA} - \text{g} - \text{C18 or HA at 530 nm}}{\text{Intensity of nitrobenzoxadiazole} - \text{labelled unmodified liposomes only at 530 nm}}$$

Equation 3.2: $\frac{C_{L0}}{N_c} = \frac{1}{N_{RT}} C_{L0} + \frac{K_D}{N_{RT}}$

C_{L0}: initial liposome concentration

N_c: number of liposome-cell complexes

N_{RT}: total number of receptors

K_D: dissociation equilibrium constant

Equation 3.3: $\ln\left(\frac{N_c}{N_{c0}}\right) = -k_{-1}t$

N_c: number of liposome-cell complexes

N_{c0}: initial number of liposome-cell complexes

k_{-1}: dissociation rate constant

Equation 3.4:

Time required for the concentration to dissociate half of its maximum, $t_{1/2} = \frac{\ln 2}{k_{-1}}$

3.7 References

(1) Liew, A.; O'Brien, T. Therapeutic Potential for Mesenchymal Stem Cell Transplantation in Critical Limb Ischemia. *Stem Cell Res. Ther.* **2012**, *3*, 28.

(2) Tsuji, W.; Rubin, J. P.; Marra, K. G. Adipose-Derived Stem Cells: Implications in Tissue Regeneration. *World J. Stem Cells* **2014**, *6*, 312–321.

(3) Wietecha, M. S.; Król, M. J.; Michalczyk, E. R.; Chen, L.; Gettins, P. G.; DiPietro, L. A. Pigment Epithelium-Derived Factor (PEDF) as a Multifunctional Regulator of Wound Healing. *Am. J. Physiol. - Hear. Circ. Physiol.* **2015**, *309*, ajpheart.00153.2015.

(4) Ito, W. D.; Arras, M.; Winkler, B.; Scholz, D.; Schaper, J.; Schaper, W. Monocyte Chemotactic Protein-1 Increases Collateral and Peripheral Conductance after Femoral Artery Occlusion. *Circ. Res.* **1997**, *80*, 829–837.

(5) Kalinski, P. Regulation of Immune Responses by Prostaglandin E2. *J. Immunol.* **2012**, *188*, 21–28.

(6) Dopheide, J. F.; Doppler, C.; Scheer, M.; Obst, V.; Radmacher, M. C.; Radsak, M. P.; Gori, T.; Warnholtz, A.; Fottner, C.; Münzel, T.; *et al.* Critical Limb Ischaemia Is Characterised by an Increased Production of Whole Blood Reactive Oxygen Species and Expression of TREM-1 on Neutrophils. *Atherosclerosis* **2013**, *229*, 396–403.

(7) Iseri, K.; Iyoda, M.; Ohtaki, H.; Matsumoto, K.; Wada, Y.; Suzuki, T.; Yamamoto, Y.; Saito, T.; Hihara, K.; Tachibana, S.; *et al.* Therapeutic Effects and Mechanism of Conditioned Media from Human Mesenchymal Stem Cells on Anti-GBM Glomerulonephritis in WKY Rats. *Am. J. Physiol. - Ren. Physiol.* **2016**, *310*.

(8) Ranganath, S. H.; Levy, O.; Inamdar, M. S.; Karp, J. M. Harnessing the Mesenchymal Stem Cell Secretome for the Treatment of Cardiovascular Disease. *Cell Stem Cell* **2012**, *10*, 244–258.

(9) Ankrum, J. A.; Dastidar, R. G.; Ong, J. F.; Levy, O.; Karp, J. M. Performance-Enhanced Mesenchymal Stem Cells via Intracellular Delivery of Steroids. *Sci. Rep.* **2014**, *4*, 4645.

(10) Martinez, V. G.; Ontoria-Oviedo, I.; Ricardo, C. P.; Harding, S. E.; Sacedon, R.; Varas, A.; Zapata, A.; Sepulveda, P.; Vicente, A. Overexpression of Hypoxia-Inducible Factor 1 Alpha Improves Immunomodulation by Dental Mesenchymal Stem Cells. *Stem Cell Res. Ther.* **2017**, *8*, 208.

(11) Leroux, L.; Descamps, B.; Tojais, N. F.; Séguy, B.; Oses, P.; Moreau, C.; Daret, D.; Ivanovic, Z.; Boiron, J. M.; Lamazière, J. M. D.; *et al.* Hypoxia Preconditioned Mesenchymal Stem Cells Improve Vascular and Skeletal Muscle Fiber Regeneration after Ischemia through a Wnt4-Dependent Pathway. *Mol. Ther.* **2010**, *18*, 1545–1552.

(12) Lu, W.; Chen, X.; Si, Y.; Hong, S.; Shi, Z.; Fu, W. Transplantation of Rat Mesenchymal Stem Cells Overexpressing Hypoxia-Inducible Factor 2 α Improves Blood Perfusion and

Arteriogenesis in a Rat Hindlimb Ischemia Model. *Stem Cells Int.* **2017**, *2017*, 1–11.

(13) Haider, H. K.; Jiang, S.; Idris, N. M.; Ashraf, M. IGF-1-Overexpressing Mesenchymal Stem Cells Accelerate Bone Marrow Stem Cell Mobilization via Paracrine Activation of SDF-1α/CXCR4 Signaling to Promote Myocardial Repair. *Circ. Res.* **2008**, *103*, 1300–1308.

(14) Oikonomopoulos, A.; Van Deen, W. K.; Manansala, A. R.; Lacey, P. N.; Tomakili, T. A.; Ziman, A.; Hommes, D. W. Optimization of Human Mesenchymal Stem Cell Manufacturing: The Effects of Animal/Xeno-Free Media. *Sci. Rep.* **2015**, *5*, 16570.

(15) Choi, M. R.; Kim, H. Y.; Park, J. Y.; Lee, T. Y.; Baik, C. S.; Chai, Y. G.; Jung, K. H.; Park, K. S.; Roh, W.; Kim, K. S.; *et al.* Selection of Optimal Passage of Bone Marrow-Derived Mesenchymal Stem Cells for Stem Cell Therapy in Patients with Amyotrophic Lateral Sclerosis. *Neurosci. Lett.* **2010**, *472*, 94–98.

(16) Ritger, P. L.; Peppas, N. A. A Simple Equation for Description of Solute Release I. Fickian and Non-Fickian Release from Non-Swellable Devices in the Form of Slabs, Spheres, Cylinders or Discs. *J. Control. Release* **1987**, *5*, 23–36.

(17) Yañez, R.; Oviedo, A.; Aldea, M.; Bueren, J. A.; Lamana, M. L. Prostaglandin E2 Plays a Key Role in the Immunosuppressive Properties of Adipose and Bone Marrow Tissue-Derived Mesenchymal Stromal Cells. *Exp. Cell Res.* **2010**, *316*, 3109–3123.

(18) Girirajan, S.; Patel, N.; Slager, R. E.; Tokarz, M. E. M. E.; Bucan, M.; Wiley, J. L.; Elsea, S. H. How Much Is Too Much? Phenotypic Consequences of Rai1 Overexpression in Mice. *Eur. J. Hum. Genet.* **2008**, *16*, 941–954.

(19) Wang, H.; Chen, X.; Li, Y.; Tang, T. S.; Bezprozvanny, I. Tetrabenazine Is Neuroprotective in Huntington's Disease Mice. *Mol. Neurodegener.* **2010**, *5*, 18.

(20) Fernagut, P. O.; Diguet, E.; Labattu, B.; Tison, F. A Simple Method to Measure Stride Length as an Index of Nigrostriatal Dysfunction in Mice. *Journal of Neuroscience Methods*, 2002, *113*, 123–130.

(21) Paek, R.; Chang, D. S.; Brevetti, L. S.; Rollins, M. D.; Brady, S.; Ursell, P. C.; Hunt, T. K.; Sarkar, R.; Messina, L. M. Correlation of a Simple Direct Measurement of Muscle PO2 to a Clinical Ischemia Index and Histology in a Rat Model of Chronic Severe Hindlimb Ischemia. *J. Vasc. Surg.* **2002**, *36*, 172–179.

(22) Shireman, P. K.; Contreras-Shannon, V.; Reyes-Reyna, S. M.; Robinson, S. C.; McManus, L. M. MCP-1 Parallels Inflammatory and Regenerative Responses in Ischemic Muscle. *J. Surg. Res.* **2006**, *134*, 145–157.

(23) Chen, M.; Fan, H.; Ledford, B. T.; Farah, Z.; Barron, C.; Liu, Z.; He, J. Q. Impacts of Femoral Artery and Vein Excision versus Femoral Artery Excision on the Hindlimb Ischemic Model in CD-1 Mice. *Microvasc. Res.* **2017**, *110*, 48–55.

(24) Kim, Y. J.; Kim, H. K.; Cho, H. H.; Bae, Y. C.; Suh, K. T.; Jung, J. S. Direct Comparison of Human Mesenchymal Stem Cells Derived from Adipose Tissues and Bone Marrow in Mediating Neovascularization in Response to Vascular Ischemia. *Cell. Physiol. Biochem.* **2007**, *20*, 867–876.

(25) Zhu, H.; Mitsuhashi, N.; Klein, A.; Barsky, L. W.; Weinberg, K.; Barr, M. L.; Demetriou, A.; Wu, G. D. The Role of the Hyaluronan Receptor CD44 in Mesenchymal Stem Cell Migration in the Extracellular Matrix. *Stem Cells* **2006**, *24*, 928–935.

(26) Yang, B.; Yang, B. L.; Savani, R. C.; Turley, E. A. Identification of a Common Hyaluronan Binding Motif in the Hyaluronan Binding Proteins RHAMM, CD4 and Link Protein. *EMBO J.* **1994**, *1*, 286–296.

(27) Banerji, S.; Wright, A. J.; Noble, M.; Mahoney, D. J.; Campbell, I. D.; Day, A. J.; Jackson, D. G. Structures of the Cd44-Hyaluronan Complex Provide Insight into a Fundamental Carbohydrate-Protein Interaction. *Nat. Struct. Mol. Biol.* **2007**, *14*, 234–239.

(28) Takahashi, R.; Kubota, K.; Kawada, M.; Okamoto, A. Effect of Molecular Weight Distribution on the Solution Properties of Sodium Hyaluronate in 0.2M NaCl Solution. *Biopolymers* **1999**, *50*, 87.

(29) Mizrahy, S.; Raz, S. R.; Hasgaard, M.; Liu, H.; Soffer-Tsur, N.; Cohen, K.; Dvash, R.; Landsman-Milo, D.; Bremer, M. G. E. G.; Moghimi, S. M.; *et al.* Hyaluronan-Coated Nanoparticles: The Influence of the Molecular Weight on CD44-Hyaluronan Interactions and on the Immune Response. *J. Control. Release* **2011**, *156*, 231–238.

(30) Wolny, P. M.; Banerji, S.; Gounou, C.; Brisson, A. R.; Day, A. J.; Jackson, D. G.; Richter, R. P. Analysis of CD44-Hyaluronan Interactions in an Artificial Membrane System: Insights into the Distinct Binding Properties of High and Low Molecular Weight Hyaluronan. *J. Biol. Chem.* **2010**, *285*, 30170–30180.

(31) Cheng, H.; Byrska-Bishop, M.; Zhang, C. T.; Kastrup, C. J.; Hwang, N. S.; Tai, A. K.; Lee, W. W.; Xu, X.; Nahrendorf, M.; Langer, R.; *et al.* Stem Cell Membrane Engineering for Cell Rolling Using Peptide Conjugation and Tuning of Cell-Selectin Interaction Kinetics. *Biomaterials* **2012**, *33*, 5004–5012.

(32) Thurley, K.; Gerecht, D.; Friedmann, E.; Höfer, T. Three-Dimensional Gradients of Cytokine Signaling between T Cells. *PLoS Comput. Biol.* **2015**, *11*, e1004206.

(33) Han, Q.; Bagheri, N.; Bradshaw, E. M.; Hafler, D. A.; Lauffenburger, D. A.; Love, J. C. Polyfunctional Responses by Human T Cells Result from Sequential Release of Cytokines. *Proc. Natl. Acad. Sci.* **2012**, *109*, 1607–1612.

(34) Jeon, J. S.; Bersini, S.; Whisler, J. A.; Chen, M. B.; Dubini, G.; Charest, J. L.; Moretti, M.; Kamm, R. D. Generation of 3D Functional Microvascular Networks with Human Mesenchymal Stem Cells in Microfluidic Systems. *Integr. Biol.* **2014**, *6*, 555–563.

(35) Semenza, G. L. Vasculogenesis, Angiogenesis, and Arteriogenesis: Mechanisms of Blood

Vessel Formation and Remodeling. *J. Cell. Biochem.* **2007**, *102*, 840–847.

(36) Borselli, C.; Storrie, H.; Benesch-Lee, F.; Shvartsman, D.; Cezar, C.; Lichtman, J. W.; Vandenburgh, H. H.; Mooney, D. J. Functional Muscle Regeneration with Combined Delivery of Angiogenesis and Myogenesis Factors. *Proc. Natl. Acad. Sci.* **2010**, *107*, 3287–3292.

(37) Anderson, E. M.; Kwee, B. J.; Lewin, S. A.; Raimondo, T.; Mehta, M.; Mooney, D. J. Local Delivery of VEGF and SDF Enhances Endothelial Progenitor Cell Recruitment and Resultant Recovery from Ischemia. *Tissue Eng. Part A* **2015**, *21*, 1217–1227.

(38) Ho, A. T. V.; Palla, A. R.; Blake, M. R.; Yucel, N. D.; Wang, Y. X.; Magnusson, K. E. G.; Holbrook, C. A.; Kraft, P. E.; Delp, S. L.; Blau, H. M. Prostaglandin E2 Is Essential for Efficacious Skeletal Muscle Stem-Cell Function, Augmenting Regeneration and Strength. *Proc. Natl. Acad. Sci.* **2017**, 201705420.

(39) Makarevich, P. I.; Boldyreva, M. A.; Gluhanyuk, E. V.; Efimenko, A. Y.; Dergilev, K. V.; Shevchenko, E. K.; Sharonov, G. V.; Gallinger, J. O.; Rodina, P. A.; Sarkisyan, S. S.; *et al.* Enhanced Angiogenesis in Ischemic Skeletal Muscle after Transplantation of Cell Sheets from Baculovirus-Transduced Adipose-Derived Stromal Cells Expressing VEGF165. *Stem Cell Res. Ther.* **2015**, *6*, 204.

(40) Hoefer, I. E.; Grundmann, S.; Van Royen, N.; Voskuil, M.; Schirmer, S. H.; Ulusans, S.; Bode, C.; Buschmann, I. R.; Piek, J. J. Leukocyte Subpopulations and Arteriogenesis: Specific Role of Monocytes, Lymphocytes and Granulocytes. *Atherosclerosis* **2005**, *181*, 285–293.

CHAPTER 4: Reactive-oxygen species-responsive and pH-responsive micellar nanoparticles for anticancer drug delivery

Acknowledgements

The manuscript for this chapter is under peer-review.

Willy Chin for his guidance in the polymer synthesis. Xiyu Ke for his guidance in the in vivo imaging. Shujun Gao for performing the tumor inoculation and tail-vein injections on the mice.

4.1 Introduction

Nanoparticle-mediated drug delivery has made tremendous progress over the last decade.[1] The largest clinical impact is in cancer therapy where the side effects of potent chemotherapeutic drugs are reduced by nanoparticle invasion into tumors with fenestrated blood vessels.[2] Yet, issues such as poor retention and sluggish drug release at the disease site limit their therapeutic benefits.[3–5] Strategies to overcome these obstacles include developing stimuli-responsive nanoparticles. These nanoparticle are exclusively triggered in the disease microenvironment to increase nanoparticle size or release rate of the therapeutic cargo at the targeted site.[2,6]

High levels of reactive oxygen species (ROS) is a common characteristic of several disease microenvironments.[7–10] Recent studies suggest that some cancers such as prostate cancer exhibit characteristics have constitutively high levels of ROS that has been correlated with metastatic potential.[11–13] For example, biopsies taken from patients suffering prostate cancer have more than 2-fold higher superoxide content compared to normal prostate epithelium.[14,15] From this perspective, efforts have been made to utilize this feature to design nanocarriers for cancer therapy.[16] Nanocarriers formulated from polymers composed of ROS-cleavable thioketal linkages

on the backbone or pendant arylboronic esters breakdown in the presence of ROS.[17] Another class of oxidation-sensitive polymers contain thioethers, also called polysulfides, when oxidized to sulfoxides or sulfones, cause a phase-change from hydrophobic to hydrophilic.[18–22] This change at the molecular level could be used to engineer polymer carriers to trigger drug release at tumor microenvironments.

Despite favorable in vitro and in vivo results, many of these polymers tend to be polydispersed due to the poor polymerization control or form particles with diameter in the hundred-nanometer range. We have recently established organocatalytic ring-opening polymerization (OROP) methodology, and employed it to synthesize various functional polycarbonates with remarkable control on the degree of polymerization without the use of toxic metals for biomedical applications such as drug, protein and gene delivery. With incorporation of functional groups that form non-covalent interactions, we have produced carriers that are small and stable enough to pass through the fenestrated vascular arising from aberrant tumor angiogenesis (the enhanced permeability and retention effect – EPR effect).[23–25] Our previous work suggests that polymers displaying pH-responsiveness serve as more effective drug carriers.[26] This is based on the consensus that tumors are slightly acidic (pH 6.8 – 7.2) and the predominant mechanisms of nanoparticle uptake by tumor cells are through endocytosis processes that lead to lysosomal fusion.[27] Therefore, pH-sensitive micelles were designed to exploit the higher acidity in the endolysosomal environment (pH 4.0 – 6.5) to provide enhanced intracellular drug release. Interestingly, recent studies are suggesting that endosomes and lysosomes are also oxidizing in nature.[28] Thus, on top of pH, it might be conceivable to use the oxidizing potential as a handle to trigger drug release.

In this study, we synthesized amphiphilic diblock copolymers of PEG and polycarbonate functionalized with thioether and acid groups by OROP of functional cyclic carbonates to form micellar nanoparticles as drug delivery carriers which exploit the oxidative tumor and acidic endolysosomal environments. To do so, thioether groups were installed via thio-ene and thio-yne click chemistry of 3-mercaptopropionic acid into the pendant chains of polycarbonates to construct acid-functionalized PEG-*block*-polycarbonates. The PEG length and pendant group architecture (one or two carboxylic acid groups per monomer) were varied while the total number of carboxylic acid groups per chain was fixed. To enhance the self-assembly and stability, block copolymers bearing phenylurea groups were synthesized via thio-ene click chemistry of 1-(2-mercaptoethyl)-3-phenylurea. Primary amine-containing doxorubicin was used as a model anticancer and positively-charged drug. Electrostatic interaction between the amine group in doxorubicin and the carboxylic acid group in the nanoparticles would facilitate doxorubicin loading. Doxorubicin-loaded nanoparticles were characterized for particle size, size distribution, drug loading, ROS-sensitivity, pH-sensitivity and in vitro drug release. In addition, in vitro anticancer efficacy of the doxorubicin-loaded nanoparticles was evaluated against PC-3 human prostate cancer cell line, which was reported to predominantly be in an oxidative stressed state.[14,29]

4.2 Results

4.2.1 Polymer design and synthesis

Carbonate monomers bearing allyl and propargyl functional groups were synthesized using a 2-step synthesis route.[30] PEG (MW 5 kDa or 10 kDa) was used as the macroinitiator in the synthesis to form amphiphilic diblock copolymers (**Scheme 4.1A**). The metal-free OROP of functional carbonates enabled excellent control of the lengths of the polycarbonate block. Polymers bearing the terminal alkene (**Figure 4.1**) or alkyne (**Figure 4.2**) pendant groups exhibited

narrow molecular weight distribution with a polydispersity index of ~1.1 and are versatile platforms for addition of various functional groups. For this study, we varied the degree of polymerization (DP) of the hydrophobic block from 5 to 15, which are long enough to enable self-assembly but do not cause precipitation in water.[31]

Post-polymerization acid or urea functional group installation was performed via thiol-ene or thiol-yne click chemistry (**Scheme 4.1B**). To form polymers with a single carboxylic acid per pendant group, an excess of 3-mercaptopropionic acid was reacted with alkene-bearing polymers in near-quantitative conversion of the radical-mediated addition (**Figure 4.3**). For the double acid-functionalized polymers, an excess of 3-mercaptopropionic acid was reacted with alkyne-bearing polymers with near-quantitative conversion (**Figure 4.4**). Disappearance of the peak corresponding to the terminal alkyne proton (2.5 ppm) and the absence of alkene peaks suggests that the alkyne was fully converted (**Figure 4.4** & **4.5**).

For the phenylurea-functionalized polymers, the benzylic ring in the phenylurea-functionalized block polymer was designed to help in stable packing of doxorubicin through pi-pi stacking and provide a more rigid hydrophobic micellar core, and urea group contains both a hydrogen-bond donor and acceptor to stabilize the micelles through hydrogen bonding as well as interact with the carboxylic acid groups.[31] The precursor 3-mercaptoethylphenylurea was synthesized from the condensation of phenyisocyanate and cysteamine (**Figure 4.6**). Then, the alkene-bearing polymers were used to form phenylurea-functionalized polymers with different PEG lengths (**Figure 4.7** & **4.8**). The series of PEG/acid- and phenylurea-functionalized thioether-containing polycarbonate diblock copolymers were synthesized as listed in **Table 4.1**.

4.2.2 Micelle formation and doxorubicin loading

The acid-functionalized micelles had high capacity for doxorubicin molecules due to the electrostatic interactions with the primary amine on doxorubicin (**Table 4.1**). Despite forming small micelles in water, acid-functionalized polymers resulted in nanoparticles close to or above 200 nm in hydrodynamic size with polydispersed size distribution due to the formation of aggregates after doxorubicin loading (**Table 4.1**), which is not desirable for intravenous administration. This indicates that while the long hydrophobic alkyl chains facilitate self-assembly, the encapsulation was not well-ordered. On the other hand, mixing with phenylurea-functionalized polymers promoted a more well-coordinated self-assembly process to produce micelles at low concentrations, and their CMC values are in the range of 4.3-7.5 mg L^{-1}, indicating good dynamic stability after intravenous injection into the blood stream.

In contrast, doxorubicin-loaded mixed micelles had diameters of less than 100 nm with a unimodal size distribution (**Table 4.2**), which is desirable for targeting the tumor leaky vasculatures. These mixed micelles have a doxorubicin-loading capacity of 20 – 26 wt%. Mixed micelles formed with 5 kDa PEG have higher drug-loading capacity than mixed micelles formed with 10 kDa PEG (MM5S vs. MM10S; MM5D vs. MM10D) due to the relatively longer hydrophobic block. When the number of acid groups was fixed, similar drug loading levels were obtained (MM5S vs. MM5D; MM10S vs. MM10D). This indicated that the doxorubicin loading was dependent on the electrostatic interactions between doxorubicin and polymer. The zeta potential for the doxorubicin-loaded micelles range from -6.5 mV to – 3.0 mV (**Table 4.2**). These micelles are considered neutrally-charged which is favorable in minimizing uptake by phagocytic cells and clearance from the blood.[32,33]

4.2.3 Oxidation by ROS

We investigated effect of the treatment on representative polymers with oxidants H_2O_2 or NaOCl using NMR spectroscopy by tracking the downfield shift caused by the increased electron-withdrawing effect of sulfoxides and sulfones. **Figure 4.9** shows dependency of concentration and molar equivalence of H_2O_2 on the extent of oxidation of thioethers to sulfoxides. When treated with a lower concentration of H_2O_2, thioethers were partially oxidized. This is evident from the presence of 2 signals (1.85-1.77 ppm and 2.0-1.9 ppm) from the CH_2 protons, which are two carbons away from the sulfur atom. However, when treated with a higher concentration of H_2O_2, thioethers were fully oxidized. The original signals at 1.85-1.77 ppm were completely shifted to 2.0-1.9 ppm. Similar observations were made for protons on carbons adjacent to the sulfur atom (originally 2.7-2.6 ppm to 3.0-2.7 ppm).

To determine if the thioethers could be oxidized even further, the polymers were treated with a stronger oxidant, NaOCl. Interestingly, a larger downfield shift was observed. Original signals at 1.85-1.77 ppm were completely shifted to 2.0-1.9 ppm and at the same time, original signals at 2.7-2.6 ppm were shifted to 3.2-3.1 ppm. This indicates that the thioether groups were further oxidized to sulfones. This could not be reproduced at higher molar equivalency of H_2O_2 tested. This is expected because H_2O_2 require higher activation energy and rates are correspondingly slower.[34] Absence of sharp peaks at 5.0-4.7 ppm suggests that the oxidation species did not cause polymer degradation. There were also no monomer peaks found when the treated sample was analyzed by GPC (**Figure 4.10**).

To investigate the oxidative effect on the nanoparticles, doxorubicin-loaded micelles were suspended in water. Following that, the polymer solutions were spiked with H_2O_2. The increase in hydrodynamic diameter was concentration dependent. In order to simulate a highly oxidative

environment, 10 to 100 mM of H_2O_2 was added. This is equivalent to 10 to 100 times the number of thioether group. When 10 mM H_2O_2 was added, the increase in hydrodynamic diameter was only observed after 48 h (**Figure 4.11**). On the other hand, the response from the polymer oxidation at 100 mM was observed within 24 h (**Figure 4.12A** & **4.12B**).

The count rates from the dynamic light scattering was recorded to determine if the increase in diameter was due to aggregation of particles or particle swelling. H_2O_2 was added after an equilibration of 5 minutes. The mean count rate immediately decreased before stabilizing after 40 minutes (**Figure 4.12C**). This was accompanied by a slow increase in hydrodynamic diameter (**Figure 4.12D**). As the particles swelled, the refractive index of particles decreases that results in the decreasing mean count rate. A similar decrease in the mean scattered light intensity was observed for the micelles formulated with the urea-functionalized polymer 10U10 though at a much slower rate (**Figure 4.13A**). In contrast to 10S10 micelles, there was no increase in the hydrodynamic size observed after oxidation, further suggesting slow oxidation of the urea-functionalized 10U10 micelles (**Figure 4.13B**).

4.2.4 Kinetic stability of doxorubicin-loaded micelles

The lyophilized doxorubicin-loaded mixed micelles were able to disperse in water easily without the use of cryoprotectants, and the particle sizes of the micelles were close to those measured before lyophilization. For in vivo application, it is imperative for micelles to be stable in the presence of serum as serum protein binding can lead to recognition by immune system, opsonization and subsequent removal by the reticuloendothelial system. While there was an increase in size of doxorubicin-loaded micelles after 48 h incubation with 10% serum, the hydrodynamic diameters were still below 100 nm and no precipitation or aggregation was observed (**Figure 4.14A**).

The kinetic stability of doxorubicin-loaded micelles was further studied by challenging the micelles with a surfactant, sodium dodecyl sulfate (**Figure 4.14B**). The destabilizing effect of the surfactant was monitored with dynamic light scattering. The drop in the scattered light intensity reflects the degree of micelle dissociation. The micelles prepared with diblock polymers containing 10 kDa PEG were more stable than micelles prepared with diblock polymers containing 5 kDa PEG. The micelles prepared with 2 carboxylic acid groups per monomer were more stable than the micelles prepared with 1 carboxylic acid group per monomer.

4.2.5 In vitro drug release

Doxorubicin release from the micelles was studied at pH 7.4 and pH 5.0 to simulate the extracellular and endolysosomal environments, respectively (**Figure 4.15**). The drug release was also compared in the presence of hydrogen peroxide. However, it was found that doxorubicin was unstable in the presence of hydrogen peroxide at pH 7.4. This was confirmed by generating the absorbance standard curves of doxorubicin at different time points (**Table 4.3**), and doxorubicin concentration decreased as a function of time in the presence of H_2O_2. On the other hand, the photobleaching effect by H_2O_2 on doxorubicin over time was less prominent at pH 5, and there was no change in doxorubicin concentration observed. Therefore, the effect of H_2O_2 on drug release was investigated at pH 5.0.

Overall, the in vitro release profiles of doxorubicin showed no significant initial burst release, and encapsulated doxorubicin were released in a sustained manner over 8 h. After 8 h, the release rate was not significant due to the lower concentration gradient. The micelles prepared with 5 kDa PEG copolymers released 10% more doxorubicin than micelles prepared with 10 kDa PEG copolymers.

Doxorubicin release was greater in media at pH 5.0 than at pH 7.4 and the fastest in the presence of H_2O_2. The difference between conditions was the greater for MM5D than for MM5S (**Figure 4.15A** & **4.15B**). The final cumulative release of doxorubicin from MM5D was 42%, 55% and 72%, respectively (**Figure 4.15B**). Similarly, doxorubicin release from MM10S (**Figure 4.15C**) and MM10D (**Figure 4.15D**) made from the longer phenylurea-functionalized polycarbonate was also faster at pH 5.0 as compared to pH 7.4. However, for these micelles, there was no significant effect of H_2O_2.

4.2.6 Intracellular distribution of doxorubicin

The intracellular distribution and uptake of doxorubicin-loaded micelles were compared with free doxorubicin (**Figure 4.16**). Acidic endosomes and lysosomes were stained in green with LysoTracker while PC-3 nuclei were stained in blue with Hoechst dye. Diffusion of free doxorubicin molecules resulted in their accumulation in the nucleus after 1 h (**Figure 4.16A**). Nanoparticles were trafficked into the cells by endocytosis and accumulated in the cytoplasm (**Figure 4.16B**). Importantly, the micelle-encapsulated doxorubicin escaped the endosomes and consequently, doxorubicin molecules were detected in the nucleus for cells. Using flow cytometry to quantify the amount of doxorubicin molecules, cellular uptake of doxorubicin-loaded micelles was comparable with that of free doxorubicin at both 1 h and 4 h time points (**Figure 4.16C**). Particularly, there were no significant difference in the percentage of cells with doxorubicin treated with micelles loaded with doxorubicin or free doxorubicin (**Figure 4.16D**).

4.2.7 In vitro cytotoxicity of doxorubicin-loaded micelles

The cytotoxicity of blank mixed micelles and doxorubicin-loaded mixed micelles was evaluated in PC-3, an androgen-independent human prostate cancer cell line (**Figure 4.17**). PC-3 cell line is known to display some extent of drug-resistance towards doxorubicin. However, when

delivered through the MM5S or MM5D mixed micelle vehicle, a lower IC50 of 2 to 4-folds is observed (**Figure 4.17A**). MM10S and MM10D made from the longer urea-functionalized polycarbonate exhibited comparable cytotoxicity with the free doxorubicin. This is probably because of the more effective dissociation of MM5S and MM5D by oxidation, which enhanced doxorubicin release and thus exerted greater cytotoxicity. Blank micelles did not show significant toxicity to the cells where cell viability remained at 100% (**Figure 4.17B**). Thus, the cytotoxicity of doxorubicin-loaded micelles could be attributed to the encapsulated doxorubicin.

4.2.8 Biodistribution of micelles in tumor-bearing mice

The biodistribution of MM5D mixed micelles in nude BALB/c mice bearing subcutaneous PC-3 tumors was evaluated. DiR, a near-infrared fluorophore (NIRF), was encapsulated in MM5D micelles that were administered through a single tail-vein intravenous injection. The in vivo real-time biodistribution of the fluorophore was studied by whole body live imaging at various time points over 7 days. As shown in **Figure 4.18A**, within 30 min post-administration, DiR fluorescence signals were detected in the whole body because of extensive circulation of the micelles in the bloodstream. The contrast between free DiR and micelle-encapsulated DiR became apparent after 24 h. With the equivalent amount of DiR administered, DiR was more widely distributed throughout the whole body when delivered through micellar encapsulation. On the other hand, the NIRF signal from free DiR was found very strong in the liver, indicating that DiR was rapidly eliminated from the mice's blood after injection. This demonstrates the ability of micellar formulation to improve tumor treatment by enhancing circulation time. Moreover, in the mice administered with micelles, the greater intensity of NIRF signals from the subcutaneous tumor and normal tissues was more prominent at 24 h post-injection. On the other hand, signals could not be detected in the tumor in mice administered with free DiR.

The tumor and major organs were harvested at 7 days post-injection. As shown in **Figure 4.18B**, for the mice administered with DiR-loaded MM5D micelles, greater NIRF signals were detected in the tumor the healthy organs (liver, spleen and kidney). Notably, there was negligible signal detected in the heart and lungs. This contrasts with the mice injected with free DiR where high NIRF signals were detected in the lungs, liver and spleen.

4.3 Discussion

One of the long-standing challenges of drug delivery is the retention of drugs within the disease site. While small molecule drugs and nanoparticles enter fenestrated tissues easily, the tissue interstitial pressure also pushes them back out into the circulation. To this end, we proposed a swelling micelle that is triggered by the local ROS levels. We hypothesized that the swelling micelle increases the retention and release of cargo exclusively in the diseased tissue (**Figure 4.19**). To test this hypothesis, we designed the biodegradable polymers with oxidizable thioether groups by using polycarbonates and thiol-ene or thiol-yne click chemistry to install carboxylic acid groups or phenylurea groups in a facile manner.

PEG was chosen for the hydrophilic block to reduce the recognition and clearance of the micelles by immune cells. Carboxylic acid groups were installed on the hydrophobic polycarbonate block to facilitate doxorubicin loading. Although the acid-functionalized polymers could self-assembly in water to form micelles with diameters of less than 100 nm and had low polydispersity indices, the complexation with doxorubicin molecules via electrostatic interactions resulted in micelles that were polydispersed and large. This may be due to uncontrolled aggregation of doxorubicin molecules. However, when the acid-functionalized polymers were mixed with the phenylurea-functionalized polymers, the micelle diameters decreased dramatically

and were monodispersed. There was minimal reduction in the loading level which suggests that the phenylurea groups help in coordinating the pi-pi stacking of doxorubicin molecules within the micelles.

Apart from loading high quantities of drug molecules, the loaded drugs also need to be effectively released upon cellular internalization. Upon endocytosis, the micelles are trafficked into the acidic endolysosomal compartments. For these micelles, at pH 5.0, both acid and amino groups become more protonated. Thus, the initial electrostatic interactions that held doxorubicin to the polymer are weakened. This pH trigger contributed to the quicker diffusion of doxorubicin out of the micellar core.

Thioethers, which are also called sulfides, are oxidized in the presence of strong oxidants to sulfoxides and sulfones. The changes in physical and chemical properties from the oxidation of methionine, a biological building block, have been utilized at the cellular level to modulate crucial protein function and cell physiology.[35,36] Similarly, the extent of oxidation increases the polymer hydrophilicity due to the presence of additional oxygen atoms. The increased hydrophilicity facilitates water to enter and swell the micelles from diameters of less than 100 nm to over 500 nm. Interestingly, the architecture of the polymers influenced the response of the micelles to oxidation by H_2O_2. All the polymers have the same number of thioether and carboxylic acid groups. Yet, the shorter backbone in MM5D allowed greater access for H_2O_2 to the thioether groups to result in an increased release in doxorubicin than MM5S.

The balance of micelle stability and sensitivity to the oxidation is an important consideration for triggered release systems. The relative hydrophilic to hydrophobic ratio of the phenylurea-functionalized diblock polymers was kept the same. In the mixed micelles with 10 kDa PEG, the longer phenylurea-functionalized polycarbonate stabilized the micelles and protected the

micelles from dissociation caused by surfactant molecules. However, this also resulted in a slower drug release than micelles prepared with polymers containing 5 kDa PEG. The phenylurea groups form strong hydrogen bonding between themselves within the micellar core and strong hydrophobic interactions through the aromatic ring. Nevertheless, the increase in the hydrophilicity from the sulfoxide bond disrupted some of the urea/urea hydrogen bonding interaction to result in a triggered release of doxorubicin.

H_2O_2 was selected as a model reactive oxygen species because it is widely-recognized second messenger in rapidly proliferating cells. However, other ROS and reactive nitrogen species also contribute to cancer progression. In this regard, we investigated the intracellular transport of doxorubicin by the micelles in PC-3 cells that were reported to produce high levels of ROS. The distribution of doxorubicin in PC-3 cells from micelle delivery was similar to that of free doxorubicin formulation. As a result, the mixed micelles inhibited the proliferation of PC-3 cancer cells at a comparable drug concentration as the free doxorubicin. Furthermore, the advantage of the ROS-triggered swelling micelle was more pronounced in vivo. The micelles not only extended the circulation time, but they also increased the accumulation of the cargo in the tumor.

4.4 Conclusions

In summary, thioether-containing acid- and urea-functionalized PEG-block-polycarbonates were synthesized to form mixed micelles with diameters of 30 – 70 nm. These mixed micelles effectively loaded the amine-containing chemotherapy drug doxorubicin via electrostatic and hydrogen bonding interactions as well as pi-pi stacking. Drug release from the micelles is both pH- and ROS-sensitive. The micelles accumulated in the tumor tissue based on the EPR effect in a PC-3 xenograft mouse model. The triggered size expansion nanoparticles are

not exclusive to tumors, and could be useful in improving retention and release of drugs in other diseased tissues.

4.5 Experimental methods

4.5.1 Materials

All chemicals were obtained from Sigma-Aldrich (U.S.A.) and used as received. 1-(3,5-bis(trifluoromethyl)-phenyl)-3-cyclohexyl-2-thiourea (TU) was prepared as reported previously.[23–25] TU was dissolved in tetrahydrofuran (THF), stirred with CaH_2, filtered to get rid of moisture, and vacuum dried to remove the residual solvent. 1,8-Diazabicyclo[5,4,0]undec-7-ene (DBU) was stirred over CaH_2, vacuum distilled, and then transferred to a glove box. Doxorubicin-hydrochloride was bought from Merck (Singapore). PC-3 human prostate cancer cell line was purchased from ATCC (U.S.A.), and cultured in RPMI-1640 medium containing 25 mM Hepes and L-glutamine (Lonza, Singapore) supplemented with 10% fetal bovine serum (FBS), 100 U/mL penicillin and 100 μg/mL streptomycin at 37 °C in 5% CO_2.

4.5.2 Synthesis of block copolymers

5-Methyl-5-allyoxycarbonyl-1,3-dioxan-2-one (MAC) and 5-methyl-5-propargyloxycarbonyl-1,3-dioxan-2-one (MPC) monomers were synthesized as reported,[30] recrystallized and freeze-dried. All polymerizations were carried out in a glove-box under nitrogen atmosphere.

PEG-P(MAC): MAC (100 mg, 0.5 mmol) was added to a reaction vial containing TU catalyst (9.25 mg, 0.025 mmol) dissolved in dry dichloromethane (1 mL). The mixture was subsequently charged with PEG (250 mg, 0.025 mmol, Mn 10000 g mol^{-1}, PDI 1.04) before adding DBU (3.8 μL, 0.025 mmol), and left to stir at room temperature for approximately 45 minutes. At the end of

the reaction, an excess of benzoic acid (5 mg, 0.04 mmol) was added to quench the catalyst. The crude polymer was then precipitated twice into cold ether and the supernatant decanted to obtain loose white powdery solids (77% yield). ^{1}H NMR (400 MHz, $CDCl_3$, δ): 5.93 – 5.82 (m, 12H, C*H*vinyl), 5.34 – 5.21 (m, 24H, CH_2-vinyl), 4.65 – 4.61 (m, 24H, OCH_2CHCH_2), 4.34 – 4.25 (m, 48H, OC(O)OCH_2), 3.68 – 3.59 (m, 909H, OCH_2CH_2O), 3.37 (s, 3H, OCH_3), 1.26 (s, 36H, CH_3).

PEG-P(MPC): MPC (99 mg, 0.5 mmol) was added to a reaction vial containing TU catalyst (9.25 mg, 0.025 mmol) dissolved in dry dichloromethane (1 mL). The mixture was subsequently charged with PEG (500 mg, 0.05 mmol, Mn 10000 g mol^{-1}, PDI 1.04) before adding DBU (3.8 μL, 0.025 mmol), and left to stir at room temperature for approximately 45 minutes. At the end of the reaction, an excess of benzoic acid (5 mg, 0.04 mmol) was added to quench the catalyst. The crude polymer was then precipitated twice into cold ether and the supernatant decanted to obtain a white powdery solid (89% yield). ^{1}H NMR (400 MHz, $CDCl_3$, δ): 4.73 – 4.70 (m, 14H, OCH_2C≡CH), 4.36 – 4.25 (m, 28H, OC(O)OCH_2), 3.68 – 3.59 (m, 909H, OCH_2CH_2O), 3.37 (s, 3H, OCH_3), 2.54 (t, 7H, C≡C*H*), 1.26 (s, 21H, CH_3).

4.5.3 Post polymerization functionalization of block copolymers

For post polymerization urea-functionalization of PEG-P(MAC), 1-(2-mercaptoethyl)-3-phenylurea (216 mg, 1.1 mmol) was dissolved in dry *N*,*N*-dimethylformamide (1 mL) before PEG-P(MAC) (200 mg, 0.22 mmol alkene) and 2,2-dimethoxy-2-phenylacetophenone (2.8 mg, 0.011 mmol) were added and mixed. The mixture was then irradiated at 254 mn using Spectrolinker™ XL-1500 UV Crosslinker (999 mJ cm^{-2}) for 2 hours. The mixture was purified by column chromatography on a Sephadex LH-20 column with methanol as eluent, yielding pure white crystalline solids (82% yield). ^{1}H NMR (400 MHz, DMSO-d_6, δ): 8.56 (s, 11H, PhN*H*), 7.37 (d, 25H, Ph*H*), 7.19 (t, 25H, Ph*H*), 6.87 (t, 12H, Ph*H*), 6.25 (t, 11H, CH_2N*H*), 4.29 – 4.16 (m, 50H,

OC(O)OCH_2), 4.16 – 4.09 (m, 25H, OCH_2CH_2CH_2S), 3.56 – 3.45 (m, 909H, OCH_2CH_2O), 3.27 – 3.20 (m, 23H, CH_2NHCO), 3.24 (s, 3H, OCH_3), 2.60 – 2.52 (m, 48H, CH_2SCH_2), 1.85 – 1.77 (m, 25H, O CH_2CH_2CH_2S)), 1.16 (s, 42H, CH_3).

For post polymerization acid-functionalization of PEG-P(MAC), PEG-P(MAC) (200 mg, 0.22 mmol alkene) was dissolved in dry *N*,*N*-dimethylformamide (1 mL) before 3-mercaptopropionic acid (57 μL, 0.66 mmol) and 2,2-dimethoxy-2-phenylacetophenone (2.8 mg, 0.011 mmol) were added and mixed. The mixture was then irradiated at 254 mn using Spectrolinker™ XL-1500 UV Crosslinker (999 mJ cm^{-2}) for 2 hours. The mixture was precipitated twice in cold ether and the supernatant decanted to obtain sticky white powdery solids (93% yield). ^{1}H NMR (400 MHz, $CDCl_3$, δ): 4.35 – 4.20 (m, 60H, OC(O)OCH_2, OCH_2CH_2CH_2S), 3.68 – 3.59 (m, 909H, OCH_2CH_2O), 3.37 (s, 3H, OCH_3), 2.81 – 2.74 (m, 20H, CH_2COOH), 2.68 – 2.57 (m, 40H, CH_2SCH_2), 2.00 – 1.88 (m, 20H, O CH_2CH_2CH_2S), 1.26 (s, 30H, CH_3).

For post polymerization acid-functionalization of PEG-P(MPC), PEG-P(MPC) (198 mg, 0.13 mmol alkyne) was dissolved in dry *N*,*N*-dimethylformamide (1 mL) before 3-mercaptopropionic acid (114 μL, 1.3 mmol) and 2,2-dimethoxy-2-phenylacetophenone (1.7 mg, 0.007 mmol) were added and mixed. The mixture was then irradiated at 254 nm using Spectrolinker™ XL-1500 UV Crosslinker (999 mJ cm^{-2}) for 2 hours. The mixture was precipitated twice in cold ether and the supernatant decanted to obtain sticky white powdery solids (93% yield). ^{1}H NMR (400 MHz, DMSO-d_6, δ): 4.36 – 4.13 (m, 42H, OC(O)OCH_2, OCH_2CH_2CH_2S), 3.57 – 3.46 (m, 909H, OCH_2CH_2O), 3.24 (s, 3H, OCH_3), 3.14 (s, 6H, OCH_2CH(CH_2)S), 2.79 – 2.67 (m, 30H, CH_2COOH), 2.67 – 2.57 (m, 36H, CH_2SCH_2), 1.19 (s, 18H, CH_3).

4.5.4 Critical micellization concentration (CMC) determination

The CMC values of polymers were determined in phosphate-buffered saline (PBS, pH 7.4) using pyrene as a probe, as reported previously.[31,37] Pyrene dissolved in acetone (10 μL, 6.16×10^{-5} M) was added into each glass vial. Acetone was evaporated at room temperature for 30 min. Polymer solutions in PBS (1 mL) with concentration ranging from 0.06 to 2000 mg L^{-1} was added into the glass vials. The final pyrene concentration in each vial was 6.16×10^{-7} M and the solutions were left overnight to equilibrate. Using a FluoroMax®-4 spectrometer (HORIBA Jobin Yvon), excitation spectra of the solutions were scanned from 300 to 360 nm with an emission wavelength of 395 nm, and both the excitation and emission bandwidths were set at 2.5 nm. The intensity ratios (I337/I334) were plotted against polymer concentrations. The CMC value was determined through the intersection of the tangent to the curve at the inflection and the tangent of the points at low polymer concentrations.

4.5.5 Characterization of polymers in the presence of reactive oxygen species

Hydrogen peroxide (H_2O_2) and sodium hypochlorite (NaOCl) were used as model reactive oxygen species. Polymer (15 mg) was dissolved in water and incubated with NaOCl, or H_2O_2 in different concentrations for 4 hours at 37 °C. After the treatments, the solutions were diluted with de-ionized (DI) water and rinsed using Vivaspin 15R before freeze-drying. The oxidized polymers were analyzed by ^{1}H NMR.

For dynamic light scattering experiments (Zetasizer Nano ZS, Malvern), a weighed amount of polymer was dissolved in DI water. Measurements were taken to ensure that stable hydrodynamic size and count rate readings were achieved before samples were challenged with oxidizing agents. Continuous measurements were immediately recorded until no observable changes were made.

4.5.6 Preparation and characterization of doxorubicin-loaded micelles

Doxorubicin was encapsulated into polymeric micelles through a sonication/membrane dialysis method as described in our previous studies.[23–25]

Particle size and zeta potential of freshly prepared doxorubicin-loaded micelles and blank micelle solutions (1 mg mL^{-1}) were measured using Zetasizer Nano ZS (Malvern Instrument Ltd., Malvern, UK) equipped with a He-Ne laser beam at 633 nm (scattering angle: 173°). Each measurement was repeated 5 times and an average value was obtained from three measurements. Size measurements were performed by multimodal analysis. Particle size of doxorubicin-loaded nanoparticles in PBS (pH 7.4, 1 mg mL^{-1}) containing 10% fetal bovine serum (FBS) was recorded as a function of time to study stability of the nanoparticles.

4.5.7 Kinetic stability study of doxorubicin-loaded micelles

Kinetic stability of doxorubicin-loaded micelles in DI water was examined using sodium dodecyl sulfate (SDS) as a destabilizing agent. Briefly, SDS aqueous solution was added to doxorubicin-loaded micelles (1 mg mL^{-1}) at a final concentration of 2.23 mg mL^{-1}, and mixed by pipetting. The change in scattered light intensity was recorded by DLS using Zetasizer Nano ZS (Malvern Instrument Ltd., Malvern, UK).

4.5.8 In vitro release study of doxorubicin-loaded micelles

The release rate of doxorubicin from doxorubicin-loaded micelles (1 mg/mL) was investigated in PBS (150 mM, pH 7.4) or acetate buffer (150 mM, pH, 5.0) with or without H_2O_2 (100 mM). The lyophilized doxorubicin-loaded micelles were resuspended in PBS buffer (pH7.4) at a concentration of 1 mg/ml and placed into a dialysis bag with MWCO of 1000 Da (Spectra/Por 7, Spectrum Laboratories Inc.). The bag was submerged into a bottle containing 30 mL of PBS buffer (pH 7.4) and placed in a shaking (100 rev min^{-1}) 37 °C water bath. At each time point, a 1

mL sample was taken from the bulk solution outside the dialysis bag and replaced with 1 mL of fresh PBS buffer. The absorbance of doxorubicin in the solution at 480 nm was measured with a UV-Vis spectrophotometer. The doxorubicin content was calculated using a calibration curve formed from a series of doxorubicin concentrations in PBS (pH 7.4). Calibration curves at the different time-points were constructed to account for decreasing extinction coefficient of doxorubicin in solution over time.

4.5.9 In vitro cytotoxicity study

Cytotoxicity studies against PC-3 cells with free doxorubicin, blank micelles and doxorubicin-loaded micelles were investigated by CellTiter-Blue assay (Promega, USA). PC-3 cells were seeded on 96-well plates at a density of 2500 cells per well and left overnight in a 37 °C, 5% CO2 incubator. Free doxorubicin, polymers and freeze-dried doxorubicin-loaded micelles were suspended in cell culture medium at a series of concentrations. 100 μL of prepared solution was used to substitute the medium in each well. Six replicates were tested for one concentration of each sample. The plates were incubated for 72 h. Subsequently, 100 μL of fresh growth medium and 20 μL of CellTiter-Blue reagent were added to replace the sample solution in each well. The plates were then maintained in the incubator for 4 h. The plates were shaken briefly and absorbance readings of each well were recorded with a microplate reader. The absorbance of resorufin in each well was calculated as that at 570 nm deducted by that of resazurin at 600 nm. Cell viability was formulated as a percentage of absorbance of the untreated cells control.

4.5.10 Cellular distribution and uptake of doxorubicin-loaded nanoparticles

The cellular distribution and uptake of doxorubicin in PC-3 cells was studied using a confocal laser scanning microscope and flow cytometry, respectively. PC-3 cells were seeded at a density of 5×10^4 cells per well onto a 4-well borosilicate cover glass chamber (NUNC). After

overnight culture, the medium was replaced with fresh medium containing free doxorubicin (2.5 mg L^{-1}) and doxorubicin-loaded nanoparticles (doxorubicin concentration: 2.5 mg L^{-1}) for 1, 4 or 24 h. The medium was removed and washed three times with PBS and then stained with Lysotracker™ Green (Life Technologies, 75 nM) and Hoechest 33258 (5 mg L^{-1}) for 20 min at 37 °C. The cells were washed again with PBS, fixed in 10% formalin solution for 15 min at room temperature, followed by washing twice with PBS and visualized by a confocal laser scanning microscope (CLSM, Carl Zeiss LSM 510 META inverted confocal microscope, Germany). Doxorubicin was excited at 532 nm and the emission signals were collected at 595 nm. Lysotracker™ Green was excited at 488 nm and the emission signals were collected at 532 nm. Hoechst dye was excited at 350 nm and the emission signals were collected at 480 nm. All observations were conducted under the same conditions.

To quantify the fluorescence intensity of doxorubicin per cell, the cells were seeded onto 12-well plate at a density of 10^6 cells per well, and maintained for 24 h at 37 °C, 5% CO_2. The cells were then treated with free doxorubicin (1 μg/mL) and doxorubicin-loaded micelles (doxorubicin concentration: 1 μg/mL) for 1h or 4 h. The cells were then washed with phosphate buffered saline, trypsinized and collected by centrifugation at 1500 rpm for 10 min. The cell pellet was resuspended in phosphate buffered saline. Cells were assessed for fluorescent intensity per cell and percentage of cells that internalized doxorubicin using flow cytometry. Percentage of the cells that internalized doxorubicin was obtained from the ratio of events with doxorubicin expression over the number of gated events. The total number of events was recorded as 10,000. Auto-fluorescence produced by the cells was taken into account by referencing the fluorescent intensity measurement of the treated cell sample to that given by PC-3 cells without any treatment.

The measurements were done with excitation and emission wavelengths of 532 and 595 nm respectively.

4.5.11 Biodistribution of nanoparticles

Biodistribution of the micellar nanoparticles in a mouse tumor xenograft model was investigated through non-invasive bioimaging. A near-infrared fluorophore, DiR, was loaded into the micelles using the same protocol described earlier. Briefly, polymer (10 mg) and DiR (0.3 mg) were dissolved in DMSO (2 mL) and the mixture was added dropwise into 10 mL of DI water under sonication for 10 min. The resulting solution was dialyzed against DI water for 48 h, and the water was changed after 3, 6, and 24 h. The loading level of DiR was determined by dissolving a known amount of lyophilized DiR-loaded micelles in DMSO and measuring its absorbance at 759 nm wavelength. The concentration of DiR in solution was also verified before injection.

The animal protocols were approved by the Institutional Animal Care and Use Committee, Biological Resource Center, Agency for Science, Technology and Research, Singapore. PC-3 cells (5 × 106) suspended in Matrigel (ratio 1:1) were injected subcutaneously (200 μL) into the right flank of male nude mice. Five weeks post-injection, when the tumor reached about 5 – 7 mm in diameter, the mice were treated with 8 mg kg-1 DiR-loaded mixed micelles via tail vein injection. Whole-body fluorescence images were taken using Xenogen IVIS 100 (Caliper Life Sciences, U.S.A.) with the ICG filter (excitation 710 – 760 nm, emission at 810 – 875 nm) at time points 0.5 h, 5 h, 24 h, 48 h, 4 days and 7 days post-administration. Anesthetized animals (n = 3 for micelle formulation and n = 2 for free DiR dye) were placed on a 37 °C heated plate during image acquisition. The exposure time was set to 2 s. The tumors and organs were removed from sacrificed mice at 7 days post-administration. Fluorescent images of the organs were taken immediately.

4.6 Scheme, Figures and Tables

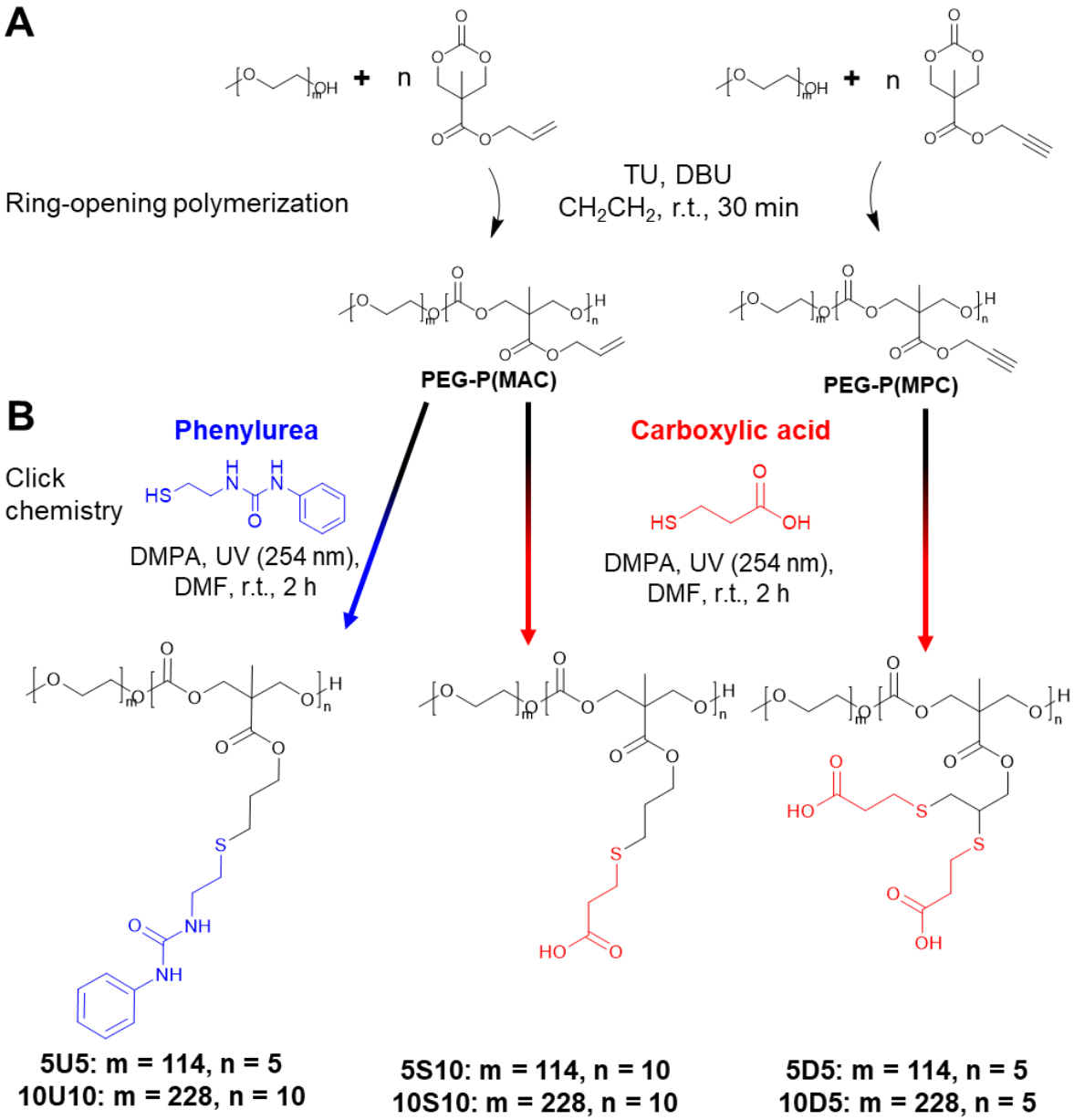

Scheme 4.1. Synthesis of diblock copolymers. A. Ring-opening polymerization with PEG (5 kDa or 10 kDa) as a macroinitiator to form polycarbonates bearing pendant alkene (PEG-P(MAC)) or alkyne (PEG-P(MPC)) functional groups. B. Post-polymerization modifications using thiol-ene and thiol-yne chemistry to form the final polymers with phenylurea groups or carboxylic acid groups.

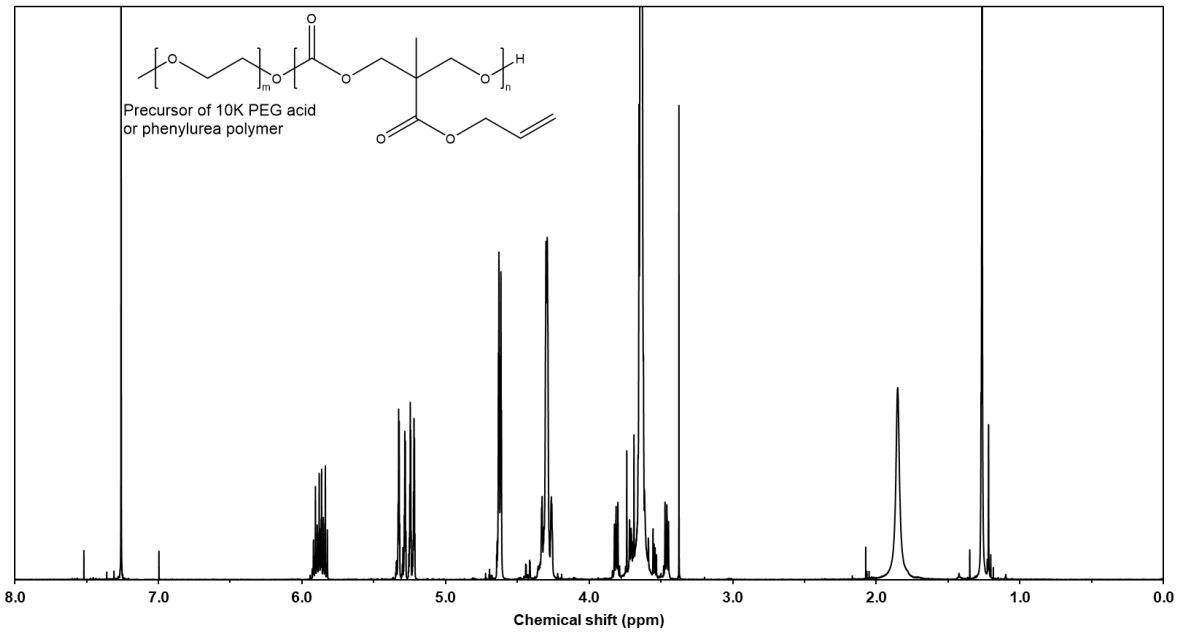

Figure 4.1. ^{1}H NMR spectrum of the 10 kDa PEG-*block*-polycarbonate with terminal alkene pendant group in $CDCl_3$. This polymer is the precursor for the final polymer functionalized with one carboxylic group or phenylurea group per carbonate monomer.

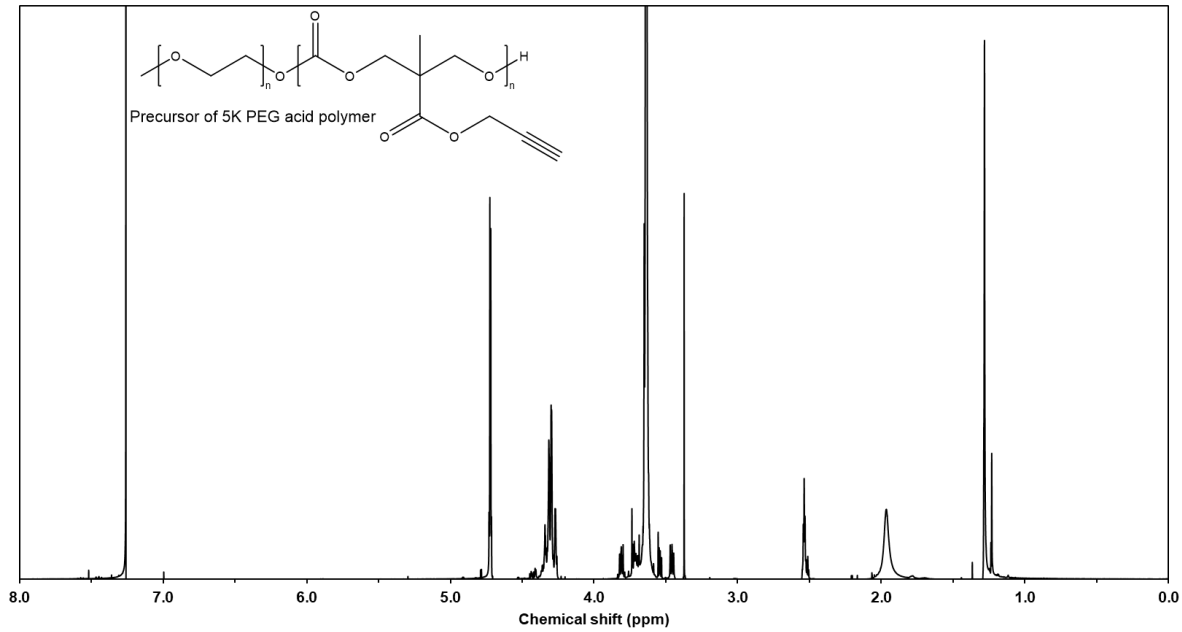

Figure 4.2. ^{1}H NMR spectrum of the 5 kDa PEG-*block*-polycarbonate with terminal alkyne pendant group in $CDCl_3$. This polymer is the precursor for the final polymer functionalized with two carboxylic groups per carbonate monomer.

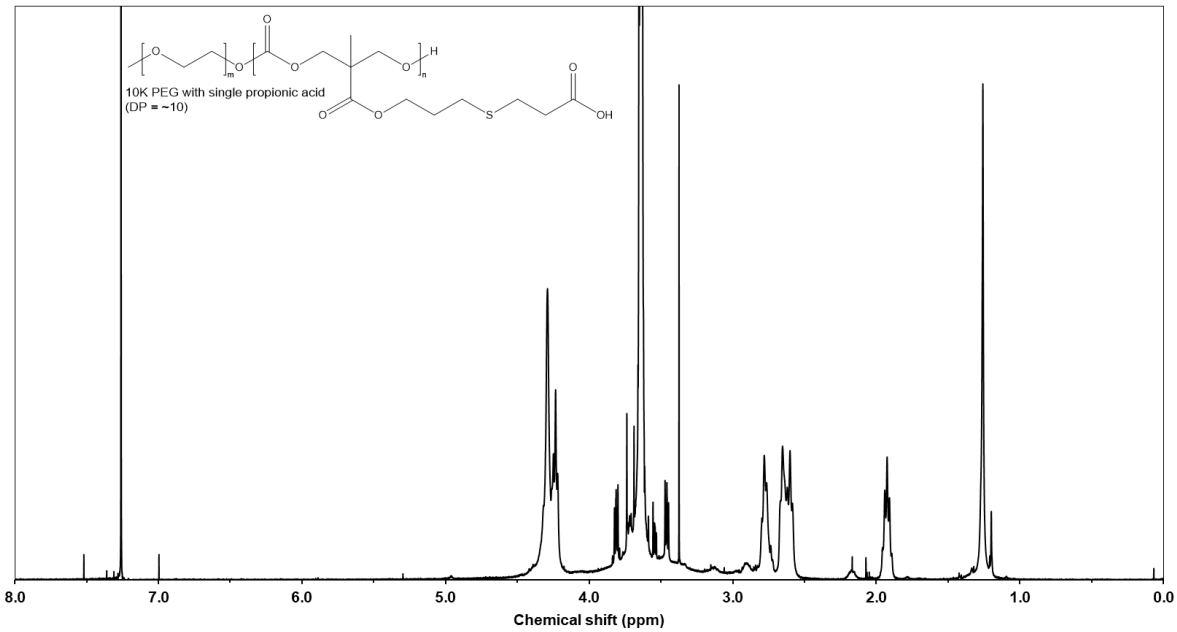

Figure 4.3. ^{1}H NMR spectrum of the 10 kDa PEG-*block*-polycarbonate functionalized with one propionic acid per carbonate monomer in $CDCl_3$.

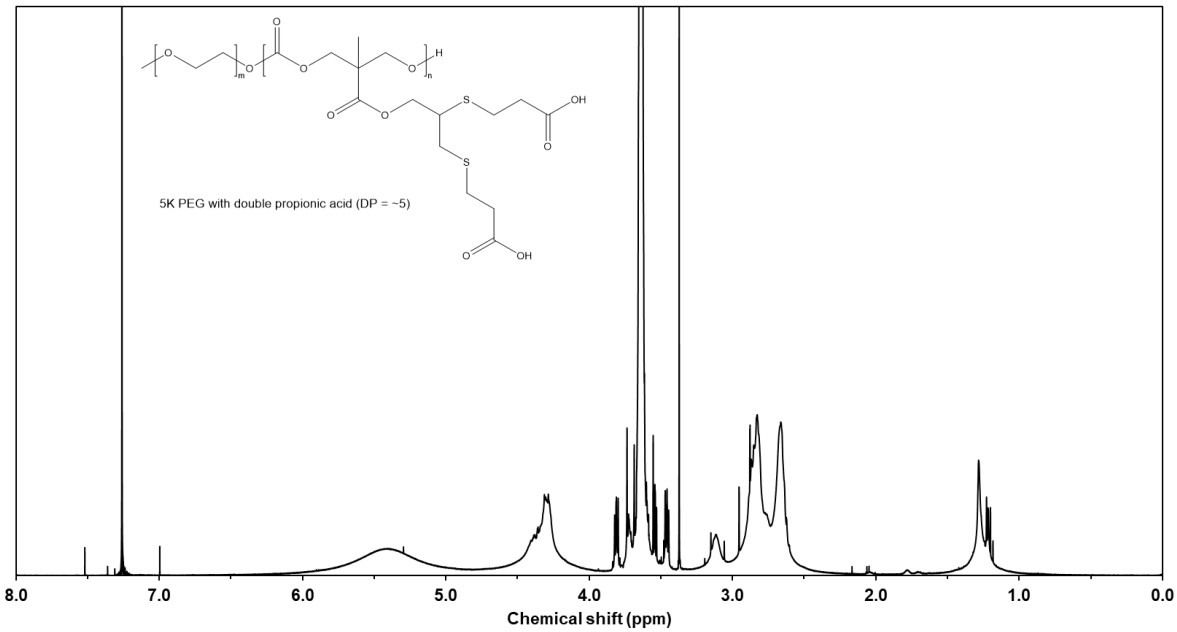

Figure 4.4. ^{1}H NMR spectrum of the 5 kDa PEG-*block*-polycarbonate functionalized with two propionic acids per carbonate monomer in $CDCl_3$.

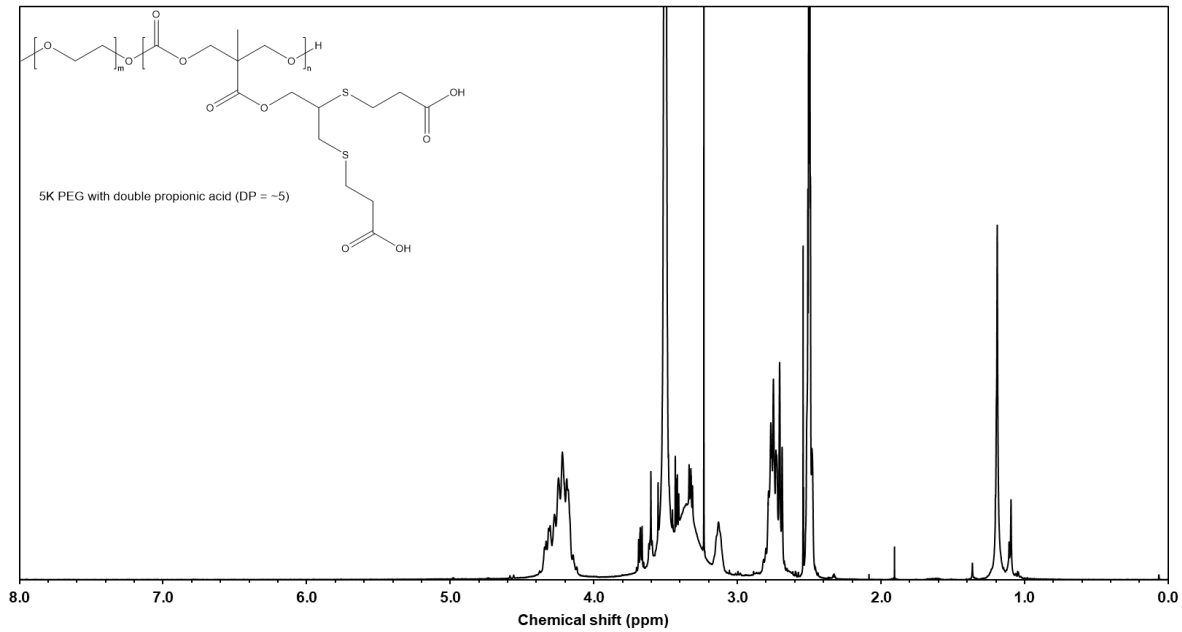

Figure 4.5. ^{1}H NMR spectrum of the 5 kDa PEG-*block*-polycarbonate functionalized with two propionic acids per carbonate monomer in DMSO-d_6.

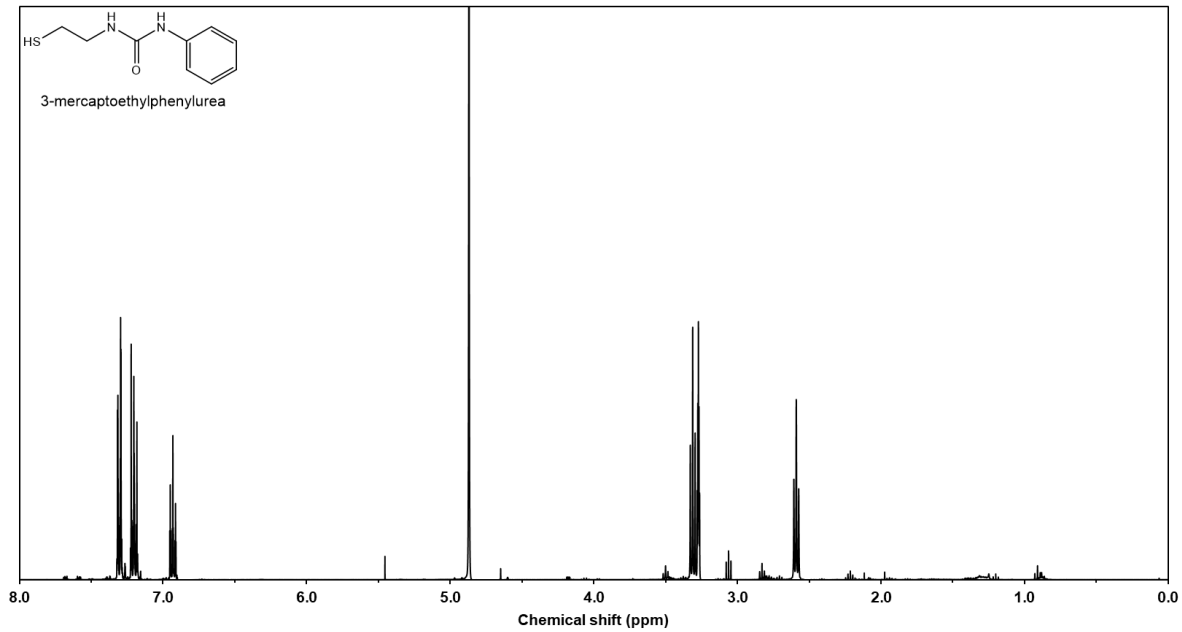

Figure 4.6. ^{1}H NMR spectrum of 3-mercaptoethylphenylurea in methanol-*d*$_4$.

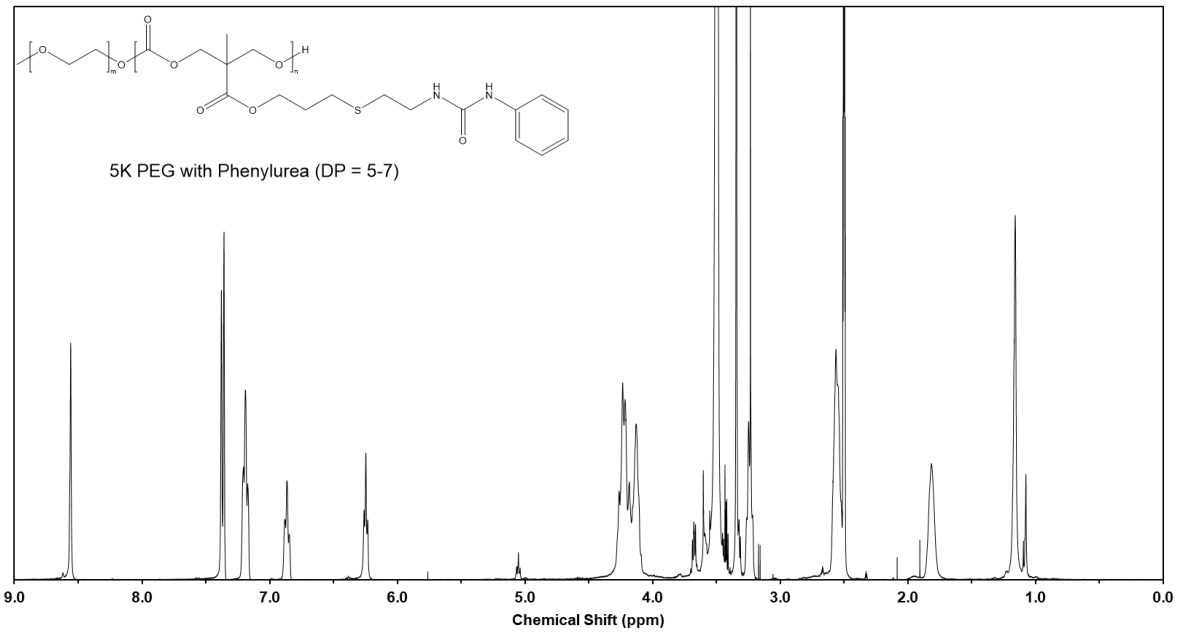

Figure 4.7. ^{1}H NMR spectrum of 5 kDa PEG-*block*-polycarbonate functionalized with one phenylurea per carbonate monomer in DMSO-d_6.

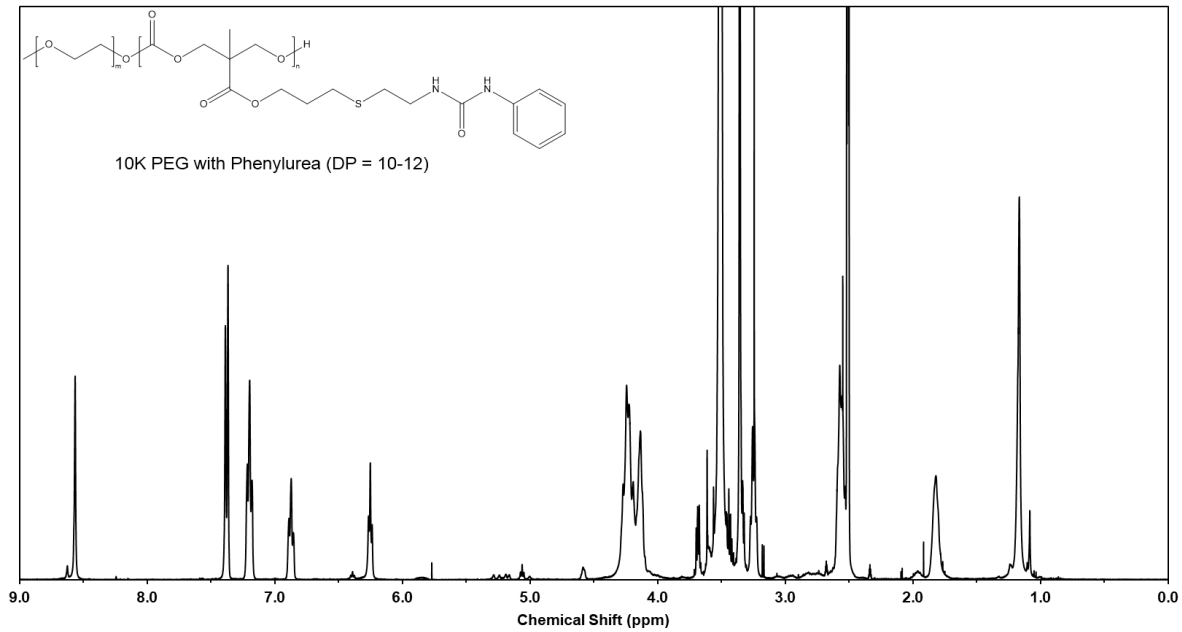

Figure 4.8. ^{1}H NMR spectrum of 10 kDa PEG-*block*-polycarbonate functionalized with one phenylurea per carbonate monomer in DMSO-d_6.

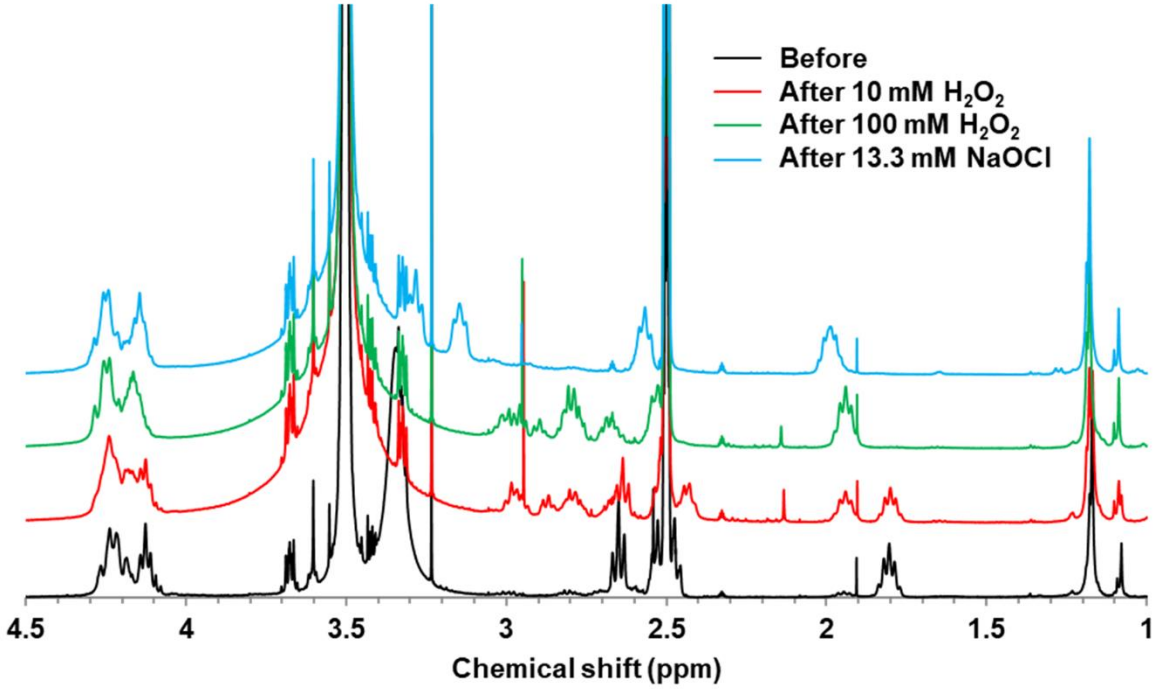

Figure 4.9. ^{1}H-NMR (in DMSO-d_6) of 10S10 used (in black) to examine the effect after the incubation with 10 mM (in red) and 100 mM H_2O_2 (in green) or 13.3 mM NaOCl (in blue) diluted in de-ionized water for 4 h at 37 °C.

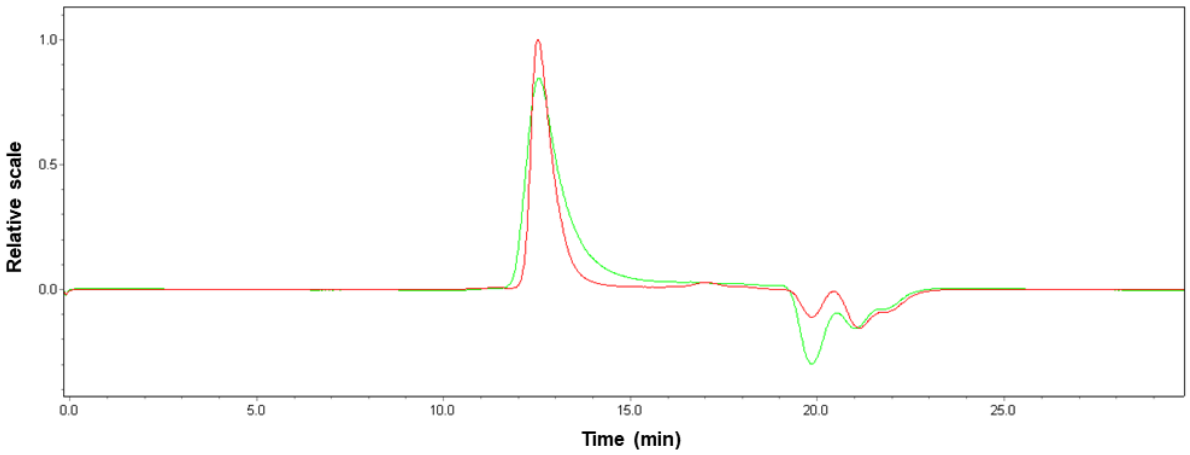

Figure 4.10. GPC traces of 10D5 before (red) and after (green) incubation with 440 mM H_2O_2 for 18 h.

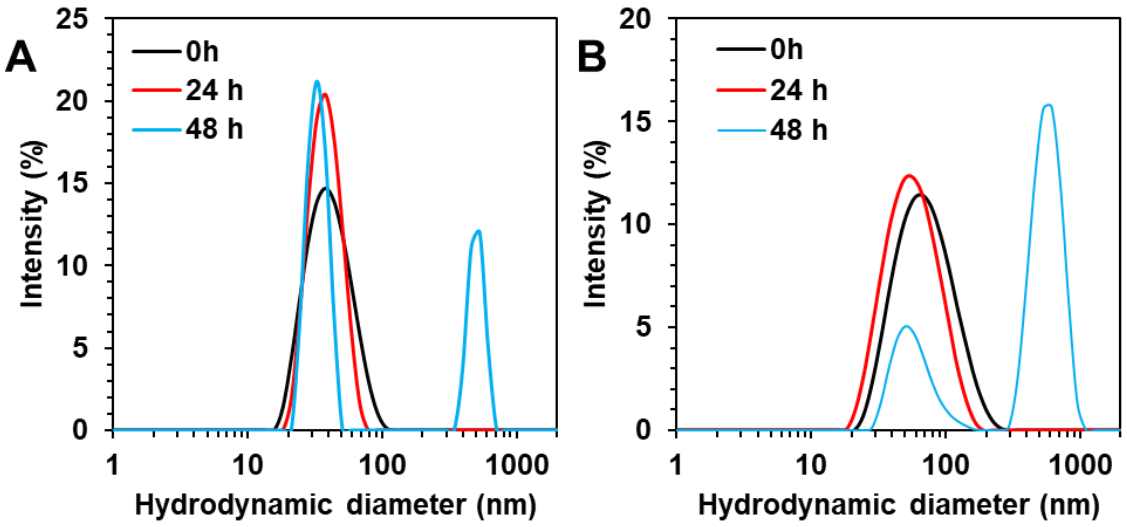

Figure 4.11. Oxidization effect on micelle hydrodynamic diameter. Change in the mean hydrodynamic diameter of (A) MM5D or (B) MM10S micelles after exposure to 100 mM H_2O_2 for 24 h and 48 h, respectively.

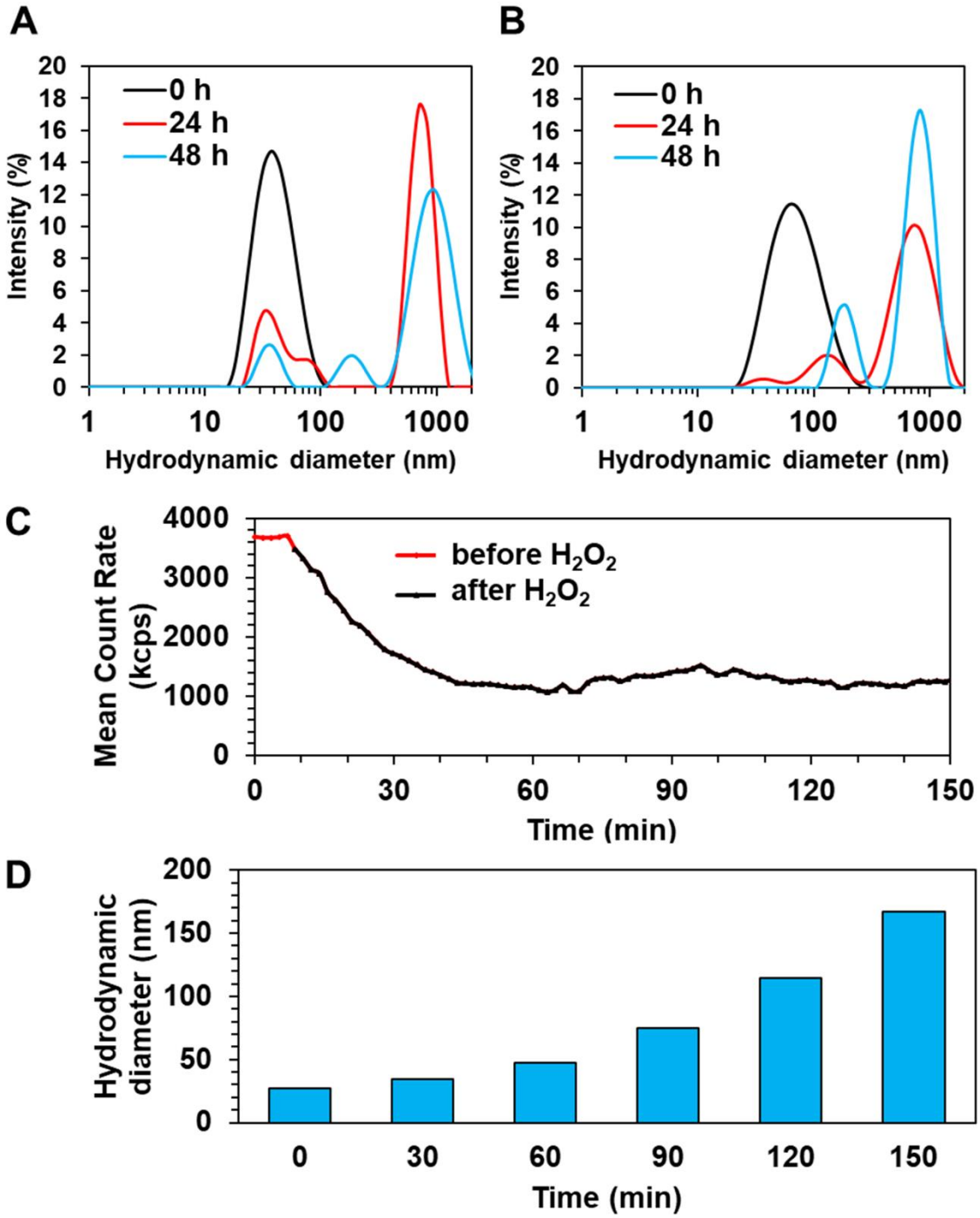

Figure 4.12. Oxidation effect on micelle hydrodynamic diameter. Change in the mean hydrodynamic diameter of (A) MM5D or (B) MM10S micelles after exposure to 100 mM H_2O_2 for 24 h and 48 h. (C) Mean count rate of the scattered light over 150 mins. (D) The corresponding change in hydrodynamic diameter over time. In (C) and (D), micelles formed with the carboxylic acid-functionalized polymer 10S10 was used with 440 mM H_2O_2.

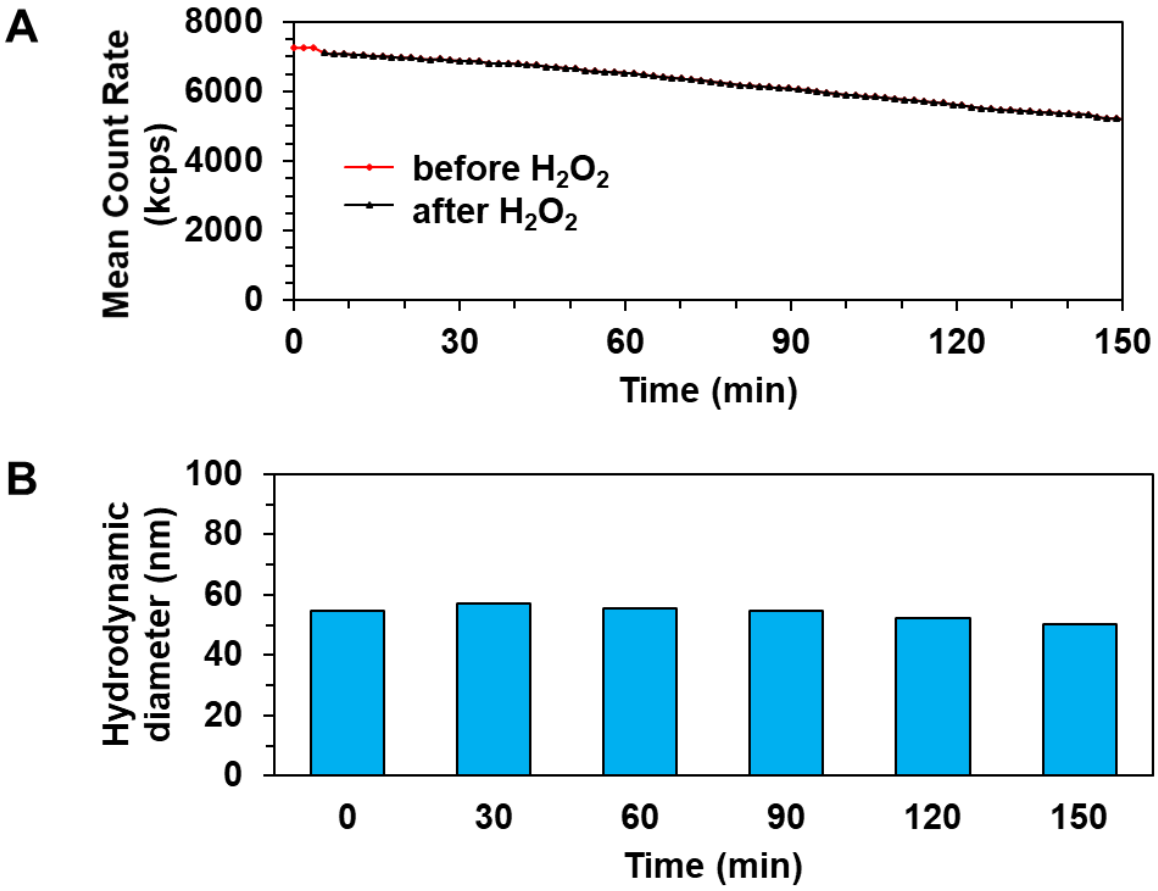

Figure 4.13. Oxidation effect on micelle hydrodynamic diameter. A. Mean count rate of the scattered light over 150 min. B. The corresponding change in hydrodynamic diameter over time. Polymer 10U10 was used with 440 mM H_2O_2.

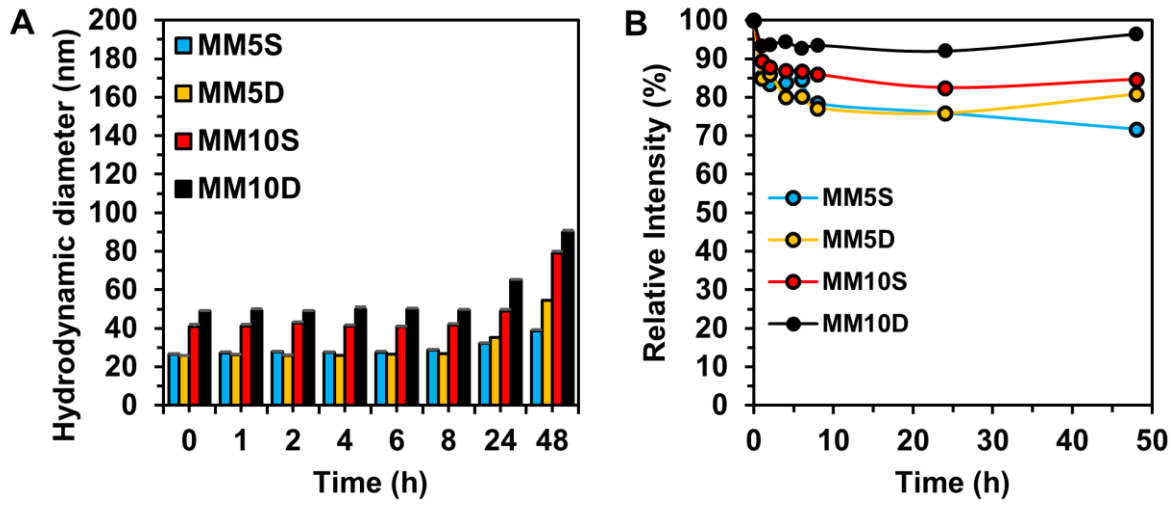

Figure 4.14. Stability of mixed micelles. A. Hydrodynamic diameters of doxorubicin-loaded micelles that were incubated in PBS (pH 7.4) supplemented with 10% serum. B. Scattered light intensity of doxorubicin-loaded micelles against time after being challenged with surfactant, sodium dodecyl sulfate. Relative intensity (%) is represented as the percentage of the scattered light intensity relative to the initial scattered light intensity.

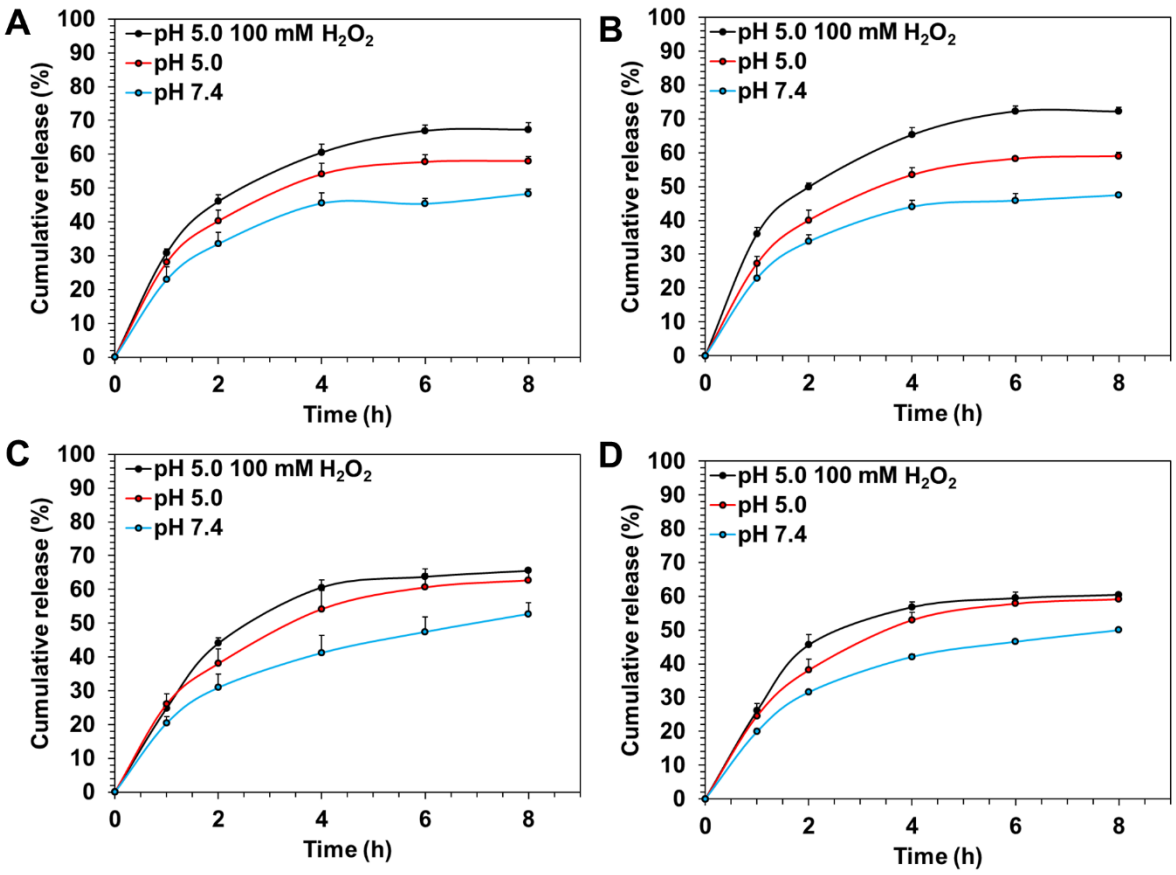

Figure 4.15. In vitro release profiles of DOX-loaded mixed micelles formed from (A) MM5S, (B) MM5D, (C) MM10S and (D) MM10D in buffers (at pH 5.0 or pH 7.4) at 37 °C. 100 mM H_2O_2 was added in pH 5.0 buffer to determine the combined effect of H_2O_2 and pH.

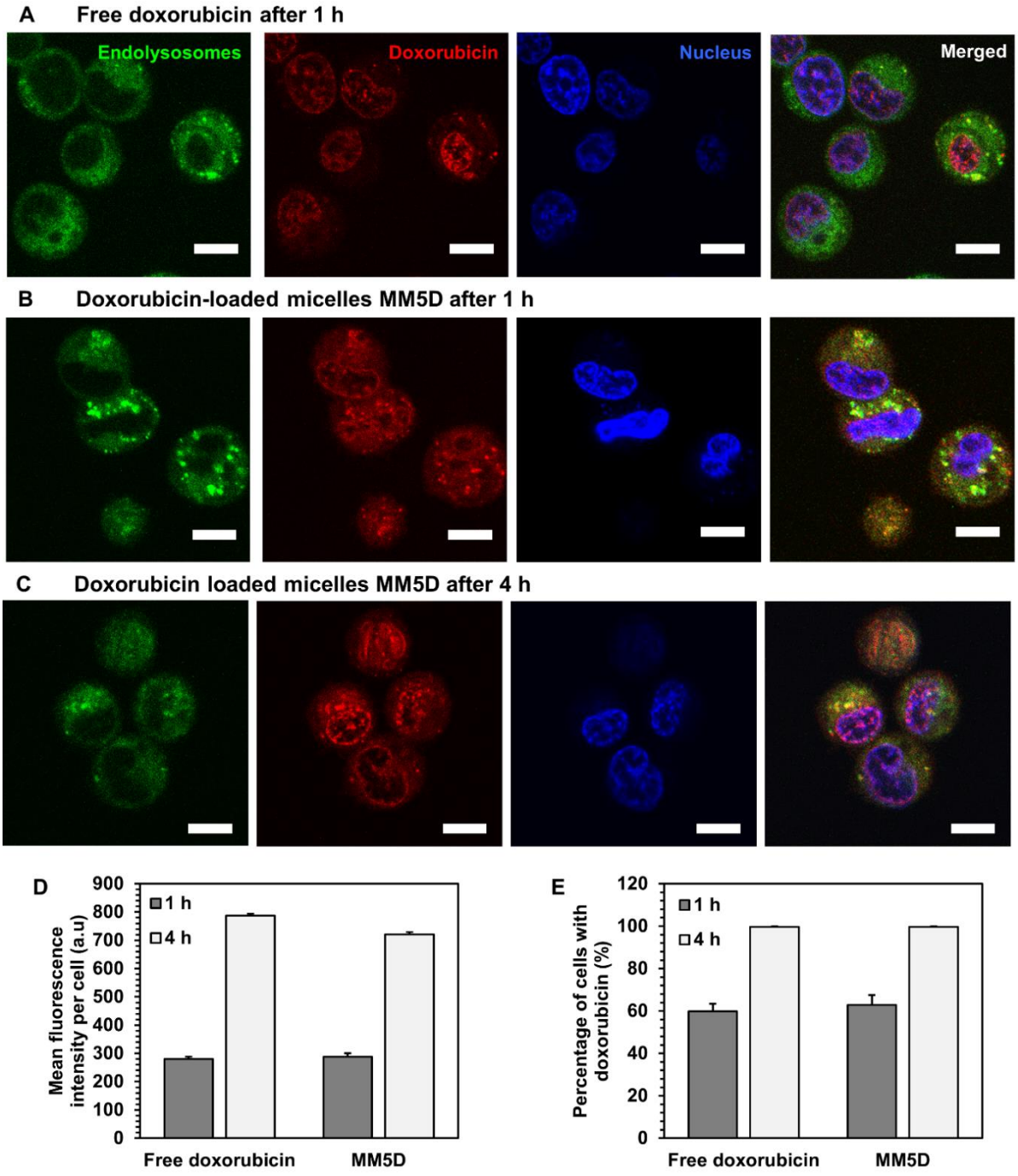

Figure 4.16. Intracellular distribution of (A) free doxorubicin in human prostate cancer PC-3 cells after incubation for 1 h at 37°C or doxorubicin-loaded micelles MM5D in PC-3 cells after incubation for (B) 1 h and (C) 4 h. Endosomes/lysosomes and nuclei were stained with LysoTracker®Green (green) and Hoechst dye (blue), respectively. Doxorubicin concentration: 10 μM. Scale bar represents 20 μm. D. Mean fluorescence intensity per PC-3 cell after incubation with free doxorubicin or doxorubicin-loaded micelles MM5D for 1 h and 4 h at 37°C. E. Percentage of PC-3 cells internalized with doxorubicin after incubation with free doxorubicin or doxorubicin-loaded micelles MM5D for 1 h and 4 h at 37 °C, respectively.

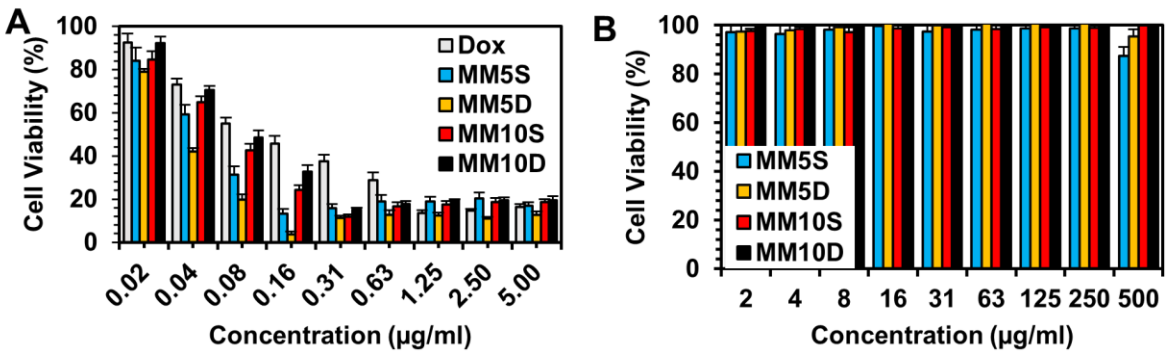

Figure 4.17. Viability of PC-3 cells after incubation with (A) free doxorubicin or doxorubicin-loaded mixed micelles and (B) blank mixed micelles as control for 72 h at 37°C.

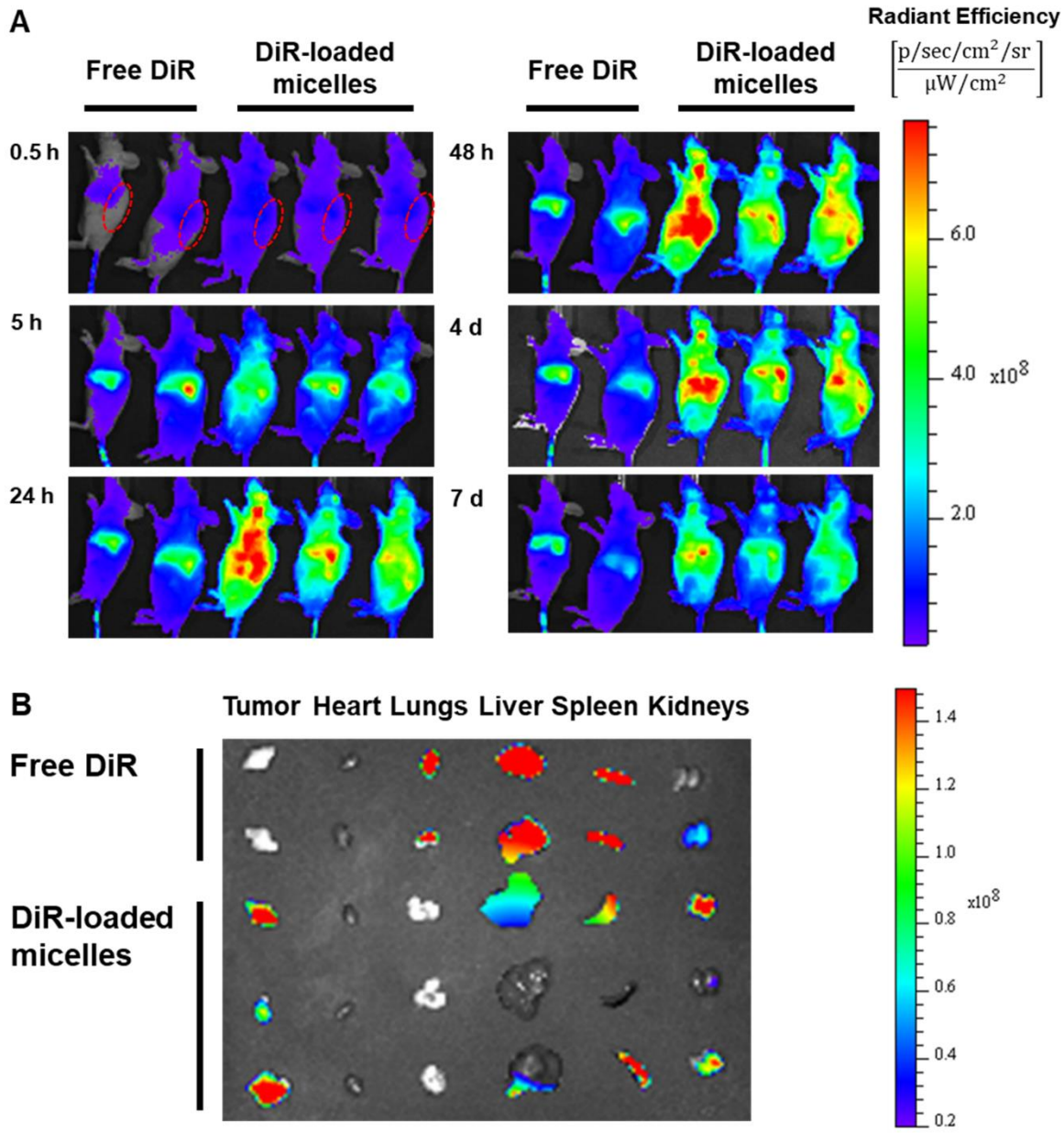

Figure 4.18. Biodistribution of free DiR and DiR-loaded MM5D micelles in nude mice bearing subcutaneous PC-3 tumors after tail-vein intravenous injection. A. Whole-body imaging at time points 0.5, 5, 24 h, 4 days and 7 days after injection. B. Tissue distribution at 7 days post injection. Scale bar represents radiant efficiency.

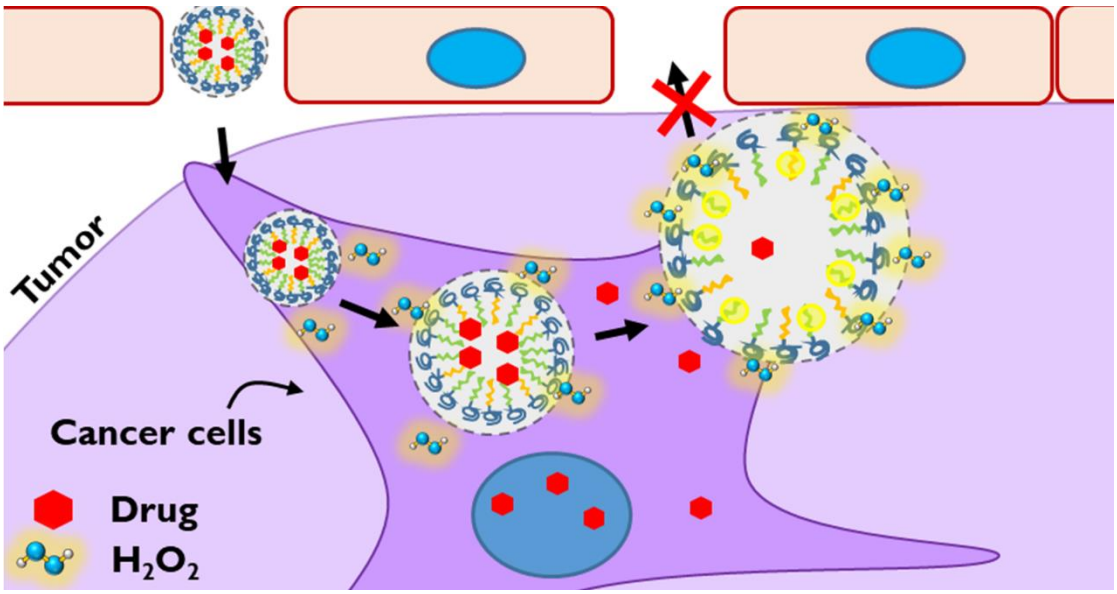

Figure 4.19. Transport of micelles encapsulating cytotoxic drugs to the highly oxidative tumor microenvironment. Drug-loaded micelles extravasate through the leaky tumor vasculature. Thioether groups of the polymeric micelles are oxidized by intracellular reactive oxygen species. In turn, the micelles swell and release the drugs within the cancer cells. The larger micelles are unable to return to the bloodstream and thus are retained within the tumor.

Table 4.1. Polymer characteristics and loading.

Polymer	PEG (m)	n	Diameter of blank micelles [nm]	Size of doxorubicin-loaded micelles [nm]	Loading level [%]	Encapsulation efficiency (%)
5KPEG(Acid)5	5K (114)	5	20 ± 0.2	215 ± 23 (61%) 25 ± 1 (34%)	22.7 ± 2	68 ± 6
5KPEG(Acid)10	5K (114)	10	18 ± 0.5	32 ± 1.3 (61%) 169 ± 26 (38%)	35.8 ± 5	108 ± 15
10KPEG(Acid)5	10K (227)	5	26 ± 0.9	38 ± 4 (50%) 183 ± 26 (46%)	16.2 ± 0.4	48 ± 1
10KPEG(Acid)10	10K (227)	10	33 ± 0.7	266 ± 28 (63%) 39 ± 4 (35%)	25.7 ± 2	77 ± 6
5KPEG(DiAcid)5	5K (114)	5	N. D.	677	34.4	103
10KPEG(DiAcid)5	10K (227)	5	N. D.	455	24.6	74

Table 4.2. Characteristics of blank mixed micelles and DOX-loaded mixed micelles.

Sample	Composition (molar ratio)	CMC [mg/L]	Hydrodynamic Diameter [nm] (PDI)	Zeta Potential [mV]	Drug loading [wt%]	Encapsulation efficiency (%)
MM5S	5S10:5U5 (1:0.5)	5.6	34 ± 2 (0.24 ± 0.01)	-6.5 ± 0.8	24 ± 1	73 ± 3
MM5D	5D5:5U5 (1:0.5)	4.3	49 ± 1 (0.18 ± 0.02)	-6.0 ± 0.3	27 ± 1	82 ± 3
MM10S	10S10:10U10 (1:0.5)	7.0	49 ± 3 (0.12 ± 0.02)	-3.7 ± 0.4	20.1 ± 0.2	60.9 ± 0.6
MM10D	10D5:10U10 (1:0.5)	7.5	63 ± 5 (0.16 ± 0.02)	-3.0 ± 0.2	23.6 ± 0.9	72 ± 2

Table 4.3. Extinction coefficient of doxorubicin at the absorbance wavelength of 480 nm at different pH ($mg^{-1}.ml.cm^{-1}$).

Time (h)	pH 7.4	pH 7.4, 100 mM H_2O_2	pH 5	pH 5, 100 mM H_2O_2
1	13.8	12.4	14.4	14.3
2	13.8	11.7	14.5	14.2
4	13.7	12.4	14.4	14.3
6	13.4	9.0	14.3	13.7
8	13.3	8.6	14.3	13.7
24	12.6	3.8	14.1	12.5

4.7 References

(1) Giodini, L.; Re, F. Lo; Campagnol, D.; Marangon, E.; Posocco, B.; Dreussi, E.; Toffoli, G. Nanocarriers in Cancer Clinical Practice: A Pharmacokinetic Issue. *Nanomedicine Nanotechnology, Biol. Med.* **2017**, *13*, 583–599.

(2) Stylianopoulos, T.; Jain, R. K. Design Considerations for Nanotherapeutics in Oncology. *Nanomedicine Nanotechnology, Biol. Med.* **2015**, *11*, 1893–1907.

(3) Podduturi, V. P.; Magaña, I. B.; O'Neal, D. P.; Derosa, P. A. Simulation of Transport and Extravasation of Nanoparticles in Tumors Which Exhibit Enhanced Permeability and Retention Effect. *Comput. Methods Programs Biomed.* **2013**, *112*, 58–68.

(4) Heldin, C. H.; Rubin, K.; Pietras, K.; Östman, A. High Interstitial Fluid Pressure - An Obstacle in Cancer Therapy. *Nat. Rev. Cancer* **2004**, *4*, 806–813.

(5) Florence, A. T. "Targeting" nanoparticles: The Constraints of Physical Laws and Physical Barriers. *J. Control. Release* **2012**, *164*, 115–124.

(6) Liu, X.; Chen, Y.; Li, H.; Huang, N.; Jin, Q.; Ren, K.; Ji, J. Enhanced Retention and Cellular Uptake of Nanoparticles in Tumors by Controlling Their Aggregation Behavior. *ACS Nano* **2013**, *7*, 6244–6257.

(7) Mittal, M.; Siddiqui, M. R.; Tran, K.; Reddy, S. P.; Malik, A. B. Reactive Oxygen Species in Inflammation and Tissue Injury. *Antioxid. Redox Signal.* **2014**, *20*, 1126–1167.

(8) Szatrowski, T. P.; Nathan, C. F. Production of Large Amounts of Hydrogen Peroxide by Human Tumor Cells. *Cancer Res.* **1991**, *51*, 794–798.

(9) Toyokuni, S.; Okamoto, K.; Yodoi, J.; Hiai, H. Persistent Oxidative Stress in Cancer. *FEBS Lett.* **1995**, *358*, 1–3.

(10) Kawanishi, S.; Hiraku, Y.; Pinlaor, S.; Ma, N. Oxidative and Nitrative DNA Damage in Animals and Patients with Inflammatory Diseases in Relation to Inflammation-Related Carcinogenesis. *Biol. Chem.* **2006**, *387*, 365–372.

(11) Liou, G.-Y.; Storz, P. Reactive Oxygen Species in Cancer. *Free Radic. Res.* **2010**, *44*, 479–496.

(12) Gupta, A.; Rosenberger, S. F.; Bowden, G. T. Increased ROS Levels Contribute to Elevated Transcription Factor and MAP Kinase Activities in Malignantly Progressed Mouse Keratinocyte Cell Lines. *Carcinogenesis* **1999**, *20*, 2063–2073.

(13) Nishikawa, M. Reactive Oxygen Species in Tumor Metastasis. *Cancer Lett.* **2008**, *266*, 53–59.

(14) Lim, S. D.; Sun, C.; Lambeth, J. D.; Marshall, F.; Amin, M.; Chung, L.; Petros, J. A.; Arnold, R. S. Increased Nox1 and Hydrogen Peroxide in Prostate Cancer. *Prostate* **2005**,

62, 200–207.

(15) Kumar, B.; Koul, S.; Khandrika, L.; Meacham, R. B.; Koul, H. K. Oxidative Stress Is Inherent in Prostate Cancer Cells and Is Required for Aggressive Phenotype. *Cancer Res.* **2008**, *68*.

(16) Wilson, D. S.; Dalmasso, G.; Wang, L.; Sitaraman, S. V.; Merlin, D.; Murthy, N. Orally Delivered Thioketal Nanoparticles Loaded with TNF-α-siRNA Target Inflammation and Inhibit Gene Expression in the Intestines. *Nat. Mater.* **2010**, *9*, 923–928.

(17) Shim, M. S.; Xia, Y. A Reactive Oxygen Species (ROS)-Responsive Polymer for Safe, Efficient, and Targeted Gene Delivery in Cancer Cells. *Angew. Chemie - Int. Ed.* **2013**, *52*, 6926–6929.

(18) Napoli, A.; Valentini, M.; Tirelli, N.; Müller, M.; Hubbell, J. A. Oxidation-Responsive Polymeric Vesicles. *Nat. Mater.* **2004**, *3*, 183–189.

(19) Allen, B. L.; Johnson, J. D.; Walker, J. P. Encapsulation and Enzyme-Mediated Release of Molecular Cargo in Polysulfide Nanoparticles. *ACS Nano* **2011**, *5*, 5263–5272.

(20) Jeanmaire, D.; Laliturai, J.; Almalik, A.; Carampin, P.; Richard d'Arcy; Lallana, E.; Evans, R.; Winpenny, R. E. P.; Tirelli, N. Chemical Specificity in REDOX-Responsive Materials: The Diverse Effects of Different Reactive Oxygen Species (ROS) on Polysulfide Nanoparticles. *Polym. Chem.* **2014**, *5*, 1393.

(21) Carampin, P.; Lallana, E.; Laliturai, J.; Carroccio, S. C.; Puglisi, C.; Tirelli, N. Oxidant-Dependent REDOX Responsiveness of Polysulfides. *Macromol. Chem. Phys.* **2012**, *213*, 2052–2061.

(22) Eloi, J. C.; Rider, D. A.; Cambridge, G.; Whittell, G. R.; Winnik, M. A.; Manners, I. Stimulus-Responsive Self-Assembly: Reversible, Redox-Controlled Micellization of Polyferrocenylsilane Diblock Copolymers. *J. Am. Chem. Soc.* **2011**, *133*, 8903–8913.

(23) Yang, C.; Tan, J. P. K.; Cheng, W.; Attia, A. B. E.; Ting, C. T. Y.; Nelson, A.; Hedrick, J. L.; Yang, Y. Y. Supramolecular Nanostructures Designed for High Cargo Loading Capacity and Kinetic Stability. *Nano Today* **2010**, *5*, 515–523.

(24) Ebrahim Attia, A. B.; Yang, C.; Tan, J. P. K.; Gao, S.; Williams, D. F.; Hedrick, J. L.; Yang, Y.-Y. The Effect of Kinetic Stability on Biodistribution and Anti-Tumor Efficacy of Drug-Loaded Biodegradable Polymeric Micelles. *Biomaterials* **2013**, *34*, 3132–3140.

(25) Attia, A. B. E.; Oh, P.; Yang, C.; Tan, J. P. K.; Rao, N.; Hedrick, J. L.; Yang, Y. Y.; Ge, R. Insights into EPR Effect versus Lectin-Mediated Targeted Delivery: Biodegradable Polycarbonate Micellar Nanoparticles with and without Galactose Surface Decoration. *Small* **2014**, *10*, 4281–4286.

(26) Liu, S. Q.; Wiradharma, N.; Gao, S. J.; Tong, Y. W.; Yang, Y. Y. Bio-Functional Micelles Self-Assembled from a Folate-Conjugated Block Copolymer for Targeted Intracellular

Delivery of Anticancer Drugs. *Biomaterials* **2007**, *28*, 1423–1433.

(27) Bareford, L. M.; Swaan, P. W. Endocytic Mechanisms for Targeted Drug Delivery. *Adv. Drug Deliv. Rev.* **2007**, *59*, 748–758.

(28) Austin, C. D.; Wen, X.; Gazzard, L.; Nelson, C.; Scheller, R. H.; Scales, S. J. Oxidizing Potential of Endosomes and Lysosomes Limits Intracellular Cleavage of Disulfide-Based Antibody-Drug Conjugates. *Proc. Natl. Acad. Sci.* **2005**, *102*, 17987–17992.

(29) Reuter, S.; Gupta, S. C.; Chaturvedi, M. M.; Aggarwal, B. B. Oxidative Stress, Inflammation, and Cancer: How Are They Linked? *Free Radic. Biol. Med.* **2010**, *49*, 1603–1616.

(30) Hu, X.; Chen, X.; Liu, S.; Shi, Q.; Jing, X. Novel Aliphatic Poly(ester-Carbonate) with Pendant Allyl Ester Groups and Its Folic Acid Functionalization. *J. Polym. Sci. Part A Polym. Chem.* **2008**, *46*, 1852–1861.

(31) Yang, C.; Ebrahim Attia, A. B.; Tan, J. P. K.; Ke, X.; Gao, S.; Hedrick, J. L.; Yang, Y. Y. The Role of Non-Covalent Interactions in Anticancer Drug Loading and Kinetic Stability of Polymeric Micelles. *Biomaterials* **2012**, *33*, 2971–2979.

(32) Li, S.-D.; Huang, L. Pharmacokinetics and Biodistribution of Nanoparticles. *Mol. Pharm.* **2008**, *5*, 496–504.

(33) Levchenko, T. S.; Rammohan, R.; Lukyanov, A. N.; Whiteman, K. R.; Torchilin, V. P. Liposome Clearance in Mice: The Effect of a Separate and Combined Presence of Surface Charge and Polymer Coating. *Int. J. Pharm.* **2002**, *240*, 95–102.

(34) Winterbourn, C. C. Reconciling the Chemistry and Biology of Reactive Oxygen Species. *Nat. Chem. Biol.* **2008**, *4*, 278–286.

(35) Hoshi, T.; Heinemann, S. H. Regulation of Cell Function by Methionine Oxidation and Reduction. *J. Physiol.* **2001**, *531*, 1–11.

(36) Schöneich, C. Methionine Oxidation by Reactive Oxygen Species: Reaction Mechanisms and Relevance to Alzheimer's Disease. *Biochim. Biophys. Acta - Proteins Proteomics* **2005**, *1703*, 111–119.

(37) Ebrahim Attia, A. B.; Yang, C.; Tan, J. P. K.; Gao, S.; Williams, D. F.; Hedrick, J. L.; Yang, Y. Y. The Effect of Kinetic Stability on Biodistribution and Anti-Tumor Efficacy of Drug-Loaded Biodegradable Polymeric Micelles. *Biomaterials* **2013**, *34*, 3132–3140.

CHAPTER 5: Controlling the Oxidation of Peroxide-Reporting Chromophore with Pore Diameter of Silica Microparticles in an Inorganic-Organic Hybrid Material

Acknowledgements

The manuscript for this chapter is under peer-review.

Yongbeom Seo for performing the SEM and TEM data acquisition at the Frederick Seitz Materials Research Laboratory Central Facilities at the University of Illinois. Sang-Hyon Chu for performing the nitrogen gas adsorption studies at Advanced Materials and Processing Branch, NASA Langley Research Center.

5.1 Introduction

Hydrogen peroxide (H_2O_2) is a chemical widely used for bleaching and disinfection in manufacturing and clinical treatments. For instance, paper and pulp industry utilizes H_2O_2 to bleach and deink new and recycled paper. The wastewater treatment and food processing industry also increasingly utilize H_2O_2 as a disinfectant due to the simplicity of application and low cost. For efficacious removal of bacteria, high concentrations of H_2O_2 of up to 16 M are often used.[1] In the medical industry, H_2O_2 is used to disinfect surgical and dentistry instruments. Fairly high concentrations of H_2O_2 (1 M) are also used as an antiseptic to clean the infected wound during surgery.

After these treatments, these industries implement routine laboratory tests to monitor residual H_2O_2. For water that is used in the food industry, the residual H_2O_2 can induce oxidation and changes the texture and composition of food.[2–4] If applied on wounds, the H_2O_2 remained on

the tissues could cause accidental cell death. The resulting accumulation of cellular debris obstructs tissue regeneration.[5–8] Previous studies reported millimolar concentrations of H_2O_2 delays wound healing by decreasing connective tissue formation.[9]

As a result, there have been several efforts to produce sensitive sensors that alert users of elevated H_2O_2 levels with fluorescence.[10,11] Alternatively, the H_2O_2 level can also be measured electrochemically with electrodes capable of reducing H_2O_2.[12] While this level of sensitivity is important in a biological system with an innate regulatory system, these sensors may be unsuitable for the detection of micro- to milli-molar levels, commonly found in the large-scale industries and clinical treatments. Additionally, sensors that depend on fluorescence or electrochemical signals reduces the portability and versatility for a wide range of industries.

To this end, this study presents a 3,3',5,5'-tetramethylbenzidine (TMB)/horseradish peroxidase-loaded patch that can alert H_2O_2 levels by generating different intensity of a visible blue color (**Scheme 5.1**). We hypothesized that the water-insoluble TMB immobilized within mesoporous silica particles of proper pore diameter and structure would act as a colorimetric indicator through the H_2O_2-mediated oxidation within a cross-linked alginate patch. We examined this hypothesis by incorporating TMB into mesoporous silica microparticles with 2 or 7 nm-diameter cylindrical pores or immobilizing TMB on non-porous silica particles at different temperatures. Pore diameter imparts the control of available surface area and molecular diffusion. We observed a range of colorimetric response when TMB was oxidized by H_2O_2. We further incorporated the TMB-silica particles into the alginate patch with interconnected micropores and examined the extent to which the microstructure of the alginate matrix modulates the intensity and stability of a positive color resulting from the oxidation reaction. Alginate was used as a model

polymer that forms a microporous patch. Overall, the results of this study would serve to integrate a color-based sensor into an amenable three-dimensional matrix for a wide range of applications.

5.2 Results

5.2.1 Synthesis of mesoporous silica particles with controlled pore diameters

The reduction of TEOS led to non-porous silica nanoparticles with an average diameter of 500 nm, measured from SEM micrographs (**Figure 5.1A**). Separately, mesoporous silica particles with different pore diameters were synthesized by the sol-gel polymerization of TEOS in the presence of either cationic cetyltrimethylammonium bromide (CTAB) or triblock copolymer $PEO_{20}PPO_{70}PEO_{20}$, Pluronic-123. Under basic conditions, the use of CTAB led to spherical particles with an average pore diameter of 2 nm, as confirmed with SEM and TEM images (**Figure 5.1B**). In contrast, the use of Pluronic-123 under acidic conditions led to rod-shaped particles with an axial length of 2 μm and average pore diameter of 7 nm (**Figure 5.1C**). These controlled pore diameters and particle shapes affect the available surface area for molecular adsorption (**Table 5.1**).

5.2.2 TMB loading into the mesoporous silica particles

The resulting silica particles were used to study the extent to which the pore diameter of particles influences the loading efficiency of TMB, coupled with other factors including solvent quality and temperature. Following the removal of surfactants by ultra-sonication in ethanol, the dried mesoporous silica particles were wet by the same volume of TMB dissolved in the organic solvents such as acetonitrile, ethyl acetate, and ethanol (**Figure 5.2A**). These three solvents were chosen based on their moderate evaporation rates and differences in polarity and surface tension.

TMB could be dissolved in acetonitrile or ethyl acetate at concentration of 50 mg/mL while it was soluble in ethanol at 5 mg/mL.

The incipient wetness impregnation process described in **Figure 5.2A** drove the TMB solution to move into pores of mesoporous silica particles via capillary action.[13] Subsequent solvent removal by evaporation resulted in TMB solids adsorbed on the external and pore wall surface. The adsorption efficiency of TMB was quantified by first measuring the mass of TMB on the silica particles with UV absorbance at 285 nm and, secondly, dividing the measured mass by the mass of TMB added during the impregnation process. Interestingly, for the mesoporous silica particles with an average pore diameter of 7 nm, the adsorption efficiency of TMB dissolved in acetonitrile or ethyl acetate was 3-fold higher than that of TMB dissolved in ethanol (**Figure 5.2B**).

With the TMB dissolved in ethyl acetate, the adsorption efficiency of TMB in the mesoporous particles was higher than that in non-porous silica particles (**Figure 5.2C**). The pore diameter of mesoporous silica particles minimally influenced the adsorption efficiency of TMB. The same results were obtained with the TMB dissolved in acetonitrile (**Figure 5.3A**). Separately, increasing the impregnation temperature from 4 to 60 $^{\circ}$C made moderate decrease of the adsorption efficiency of TMB (**Figure 5.2D**). The same results were obtained with the TMB dissolved in acetonitrile (**Figure 5.3B**).

In contrast, the adsorption efficiency of TMB dissolved in ethanol was 2-fold higher in mesoporous silica particle with an average pore diameter of 2 nm than in non-porous silica or mesoporous silica particle with an average pore diameter of 7 nm (**Figure 5.4A**). Also, with the non-porous (**Figure 5.4B**) or mesoporous silica particles with pore diameter of 7 nm (**Figure 5.4C**), increasing the process temperature from 4 to 60 °C decreased the adsorption efficiency of TMB dissolved in ethanol considerably. Increasing the process temperature did not affect the

adsorption efficiency of TMB for the mesoporous silica particles with pore diameter of 2 nm (**Figure 5.4D**).

Nitrogen adsorption isotherm analysis showed features of type IV isotherms with hysteresis (**Figure 5.5**). This result confirmed that the two types of silica particles had mesoporous structures and the pore diameter distribution showed that each particle had pore diameters of 2 nm and 7 nm, respectively (**Figure 5.6** and **Table 2.1**). After TMB adsorption, the pore volume and specific surface area of mesoporous silica with 2-nm pore diameter dramatically decreased from 0.1 cm^3 g^{-1} to 0.04 cm^3 g^{-1} and 811 m^2 g^{-1} to 50 m^2 g^{-1}, respectively (**Figure 5.6A**). This result indicates that most of the pores in the silica particle were blocked by the TMB molecules. In contrast, the silica particles with 7 nm-diameter mesopores allowed the entry of TMB molecules into pores due to the larger pore diameter, as marked by the small decrease in the pore diameter to 6 nm (**Figure 5.6B**) and final pore volume of 0.49 cm^3 g^{-1} and specific surface area of 274 m^2 g^{-1} after the TMB adsorption.

5.2.3 Analysis of oxidation reaction of TMB within silica particles

Next, we examined the extent to which the pore structure of the silica particles and the solvent quality affected the H_2O_2-induced oxidation reaction of TMB within the silica particles by exposing the TMB-silica particles to H_2O_2 and horseradish peroxidase (HRP). With this set-up, TMB underwent both one-electron and two-electron oxidations (**Figure 5.7A**). In the presence of H_2O_2 and low concentration of HRP (0.2 U/mL) relative to the number of TMB molecules, TMB reacts to form a blue charge-transfer complex. In the presence of H_2O_2 and higher concentration of HRP (1 U/mL), the reaction results in the yellow diimine.

Keeping the concentration of H_2O_2 and HRP at 50 μM and 0.2 U/mL, respectively, the different pore structures of the silica particles resulted in different extent of TMB oxidation. With

TMB dissolved in ethyl acetate, the TMB-silica particles with 7 nm-pore diameter formed blue charge-transfer complexes (**Figure 5.7B-i**), the TMB-silica particles with 2 nm-pore diameter formed a mixture of blue charge-transfer complexes and yellow diimines (**Figure 5.7B-ii**) and the TMB-silica particles without nanopores formed yellow diimines (**Figure 5.7B-iii**).

According to the UV-Vis light spectroscopy, the absorption peaks of the blue complex and the yellow diimine on the silica particles appeared at 650 nm and 450 nm, respectively (**Figure 5.7C**). Concentrations of the blue complex and the yellow diimine were quantified with the intensity of the UV-visible light absorption peaks. Then, the molar fractions of the unreacted TMB, the blue charge transfer complex and yellow diimine were calculated with the determined concentrations.

When using ethyl acetate as a solvent for adsorption of TMB, the porous structure of the silica particles affected the fraction of unreacted TMB minimally (**Figure 5.8A**). The fraction of unreacted TMB was 0.05, indicating most of the TMB molecules on or in the silica particles were oxidized by H_2O_2. Increasing the pore diameter of the mesoporous silica particles from 2 to 7 nm resulted in the slight increase in the fraction of blue complex (**Figure 5.8B**) and reduced the number of yellow diimine (**Figure 5.8C**). Consequently, the ratio of blue complex to yellow diimine was increased moderately with increasing pore diameter from 2 to 7 nm (**Figure 5.8D**). In contrast, the ratio of blue complex to yellow diimine obtained with mesoporous silica was 1.4-fold higher than that obtained with non-porous silica. Similar results were obtained with silica particles loaded with TMB by using acetonitrile as solvent (**Figure 5.9**).

The dependency of the reactivity of TMB on the nanostructure of silica particles was diminished when using ethanol as a solvent for TMB adsorption. There were minimal differences of the fractions of unreacted TMB (**Figure 5.10A**), blue complex (**Figure 5.10B**), yellow diimine

(**Figure 5.10C**), and the ratio of blue complex to yellow diimine (**Figure 5.10D**) between conditions controlled by the porous structure of silica particles. In addition, the overall ratio of blue complex to yellow diimine was lower than when ethyl acetate and acetonitrile were used as the solvent of TMB.

Concentrations of HRP also modulated the reactivity of TMB immobilized in the mesoporous silica particles and subsequent color intensity of the silica suspension. According to the quantification of blue complex and yellow diimine with UV-Vis absorption peaks, decreasing the concentration of HRP from 0.2 to 0.02 U/mL increased the fraction of unreacted TMB and blue complex by 1.4 and 1.2-folds, respectively. The fraction of yellow diimine was also reduced. Overall, decreasing the HRP concentration resulted in the two-fold increase in the ratio of blue complex to yellow diimine (**Figure 5.11**).

5.2.4 Assembly of alginate patches with TMB-loaded silica particles

Non-porous and mesoporous silica particles adsorbed with TMB were loaded into an alginate patch to examine an extent to which the microporous matrix changes the color upon exposure to H_2O_2. Ethyl acetate was used as the adsorption solvent of TMB in this study because this good solvent of TMB served to increase the ratio of blue complex to yellow diimine as well as the adsorption efficiency of TMB. The patch was prepared by sequentially mixing the TMB-silica particles with pre-gel alginate solution dissolved with horseradish peroxidase, activating the cross-linking reaction to form a gel, freezing at -20 °C and finally lyophilizing the frozen gel to create interconnected micropores (**Figure 5.12**). For the control experiment, the hydrogel was also loaded with the same amount of free TMB.

When 20 µL of 5 mM H_2O_2 solution was added onto the patches, patches encapsulated with TMB-loaded silica particles produced a more intense purple color than the patches

encapsulated with TMB-loaded non-porous silica particles (**Figure 5.13A-i**). The patch encapsulated with free TMB did not show noticeable blue color. According to the quantification of color intensity of the patches, the difference of color intensity between conditions was maximal after 5 minutes of exposure to the H_2O_2 solution (**Figure 5.13A-ii**). Additionally, the dark purple color remained stable for at least 1 week (**Figure 5.14**).

To determine the effect of micropores, a control experiment was conducted with hydrogels encapsulated with TMB-silica particles. When 20 µL of 5 mM H_2O_2 solution was added onto the hydrogels, hydrogels encapsulated with TMB-mesoporous silica particles produced a more intense blue color than the hydrogels encapsulated with TMB-non-porous silica particles (**Figure 5.13B-i**). The hydrogels encapsulated with free TMB did not show noticeable blue color. According to the quantification of the color intensities of the hydrogels, the difference of color intensity between conditions reached a maximum after 5 minutes of exposure to the H_2O_2 solution (**Figure 5.13B-ii**). After 5 minutes, the pale blue color from the hydrogel encapsulated with TMB-non-porous silica particles faded over time. The color was not visible after 20 minutes. In contrast, the hydrogel which was encapsulated with the TMB-mesoporous silica particles exhibited the highest color intensity after 10 minutes. Then, the blue color was persistently visible over 20 minutes.

The sensitivity of the microporous alginate patches to H_2O_2 was examined by varying the H_2O_2 concentration from 25 to 5,000 µM. The matrix generated the vivid blue color at 50 µM H_2O_2. The color intensity linearly increased with the H_2O_2 concentration until H_2O_2 concentration reached 200 µM. There was linear increase of the color intensity when the H_2O_2 concentration was increased from 25 to 200 µM (**Figure 5.15**). Furthermore, the sensitivity of this concentration range could be tuned by increasing the TMB loading (**Figure 5.16**).

To study the kinetics of the HRP-mediated TMB oxidation reaction within the patches, the initial oxidation reaction rates were measured with varying H_2O_2 or TMB concentrations. The oxidation rates increased with increasing H_2O_2 concentration at the given TMB concentrations (**Figure 5.17A**). Similarly, the reaction rates also increased with increasing TMB concentration at the given H_2O_2 concentrations (**Figure 5.17B**). These reaction rates were fitted to the Michaelis-Menten model (Eq. S2) and, in turn, to quantify the Michaelis-Menten constant (K_m) and the maximum reaction rate (V_{max}). K_m represents the H_2O_2 or TMB concentration where the reaction rate is equal to half of the maximal reaction rate. Therefore, K_m is an inverse measure of the affinity of TMB or H_2O_2 to HRP.

The reaction kinetics within the patch was evaluated by quantifying the apparent K_m for H_2O_2 and TMB (**Figure 5.17** and **Table 2.2**). The reaction rate versus H_2O_2 (**Figure 5.17A-i**) or TMB (**Figure 5.17B-i**) concentrations were fitted to the Michaelis-Menten model. Separately, double reciprocal plots of reaction rate versus H_2O_2 (**Figure 5.17A-ii**) or TMB (**Figure 5.17B-ii**) concentrations were fitted to the Lineweaver-Burk model where the gradient of the lines corresponds to K_m/V_{max} while the y-intercept represents $1/V_{max}$ (Eq. S3). The values of K_m and V_{max} quantified from the Lineweaver-Burk model were similar to those calculated by using the Michaelis-Menten model (**Table 2.2**). The K_m for H_2O_2 decreased by half while V_{max} increased by 1.1-fold when the concentration of TMB was increased by five-folds. On the other hand, there was minimal decrease in K_m for TMB but a two-fold increase in V_{max} when the concentration of H_2O_2 was increased by four-folds.

5.3 Discussion

This study demonstrated that loading efficiency of TMB into mesoporous silica particles is mediated by the quality of solvents for TMB. In particular, TMB dissolved in ethanol exhibited

the lower loading efficiency than TMB dissolved in acetonitrile or ethyl acetate. Ethanol, a polar protic solvent, can donate and accept hydrogen bonds with the silanol groups of the silica particles. Therefore, it is likely that ethanol competes with the TMB molecules for adsorption sites and slows the transport of TMB molecules into pore of the silica particles. Additionally, the stronger adsorption of ethanol molecules on the silica surface than acetonitrile or ethyl acetate likely inhibit the surface adsorption of TMB[14–16]. In contrast, aprotic solvents including acetonitrile and ethyl acetate act as good solvents for TMB. Therefore, we suggest that these solvents facilitate the transport of TMB molecules into pore of silica particles. The low affinity of solvents to silica particle surface would also be a significant factor to increase the loading efficiency of TMB onto or into silica particles.

Acetonitrile and ethyl acetate made minimal difference in the loading efficiency of TMB in the mesoporous silica particles, although acetonitrile is a more polar solvent than ethyl acetate. Partition coefficients of acetonitrile and ethyl acetate are -0.33 and 0.73, respectively. Although it is expected that more polar solvents would decrease the interactions of TMB with silica surfaces, our results show that the differences in polarity between acetonitrile and ethyl acetate may not be a significant factor in the adsorption of TMB onto silica surfaces. Similarly, we observed that while acetonitrile has a lower surface tension than ethyl acetate, the differences does not contribute significantly to the adsorption of TMB within the mesopores. Therefore, ethyl acetate was chosen because it is generally recognized as safe for use in personal care products.[17] This study also found that temperature can mediate the adsorption efficiency of TMB because the adsorption is both an exothermic and a negative entropic process.[16] Therefore, the higher temperature is less favorable to adsorption.

More interestingly, the nanostructure of mesoporous silica particles influenced the balance between the blue complex and the yellow diimine of oxidized TMB upon exposure to HRP and H_2O_2. The ratio of blue complex to yellow diimine formed is inversely related to the TMB oxidation type. As such, we postulated that rod-shaped silica particles with 7-nm pore diameter and 2 μm axial length increased the time for HRP and H_2O_2 molecules to travel from the surface to the center of the silica particle. Therefore, the rod-shaped mesoporous silica particles limited the TMB oxidation to the one-electron oxidation, as characterized with the blue complex. In contrast, the TMB molecules on the non-porous silica particles undergo the two-electron oxidation as characterized with formation of the yellow diimine. This is attributed to the larger accessibility of TMB molecules to the HRP and H_2O_2 than those in the mesoporous particles. The mesoporous silica with 2 nm-pore diameter displayed an intermediate formation of blue complexes and yellow diimine due to the accumulation of TMB molecules on the particle surface than within the pore channels. From these results, TMB was loaded into mesoporous silica particles with 7 nm-pore diameter using the optimal conditions for the subsequent studies in an alginate patch.

The alginate patches encapsulated with TMB-loaded mesoporous silica particles produced a positive blue color to indicate detrimental concentrations of H_2O_2. The microporous patch generated the higher intensity of color than the hydrogel free of micropores due to lower dilution effect from the water content. These results highlight that the water content in the alginate matrix plays a vital role in increasing the yield of one-electron oxidation of TMB and stabilizing the resulting positive blue color. After the addition of H_2O_2 solution, the microporous patches and hydrogels were exposed to ambient air to test the stability of the color formed. The enhanced stability of the blue color with the microporous matrix was attributed to the containment of the blue charge-transfer complex supported by the silica particle. The series of approximately parallel

lines obtained in the double reciprocal plots of reaction rate versus H_2O_2 or TMB concentration are characteristic of a ping-pong mechanism.[18] These parallel curves imply that HRP in the patch first binds with H_2O_2, and undergo an oxidation reaction before oxidizing TMB in the silica particles.

Overall, the resulting alginate hydrogel patch, from the formation of micropores, could produce the strong visible color at neutral pH within minutes and attain the highest intensity within 5 minutes of exposure to H_2O_2. The patch could detect 50 μM H_2O_2 even without the use of heavy metals, or extreme pH and temperature. No additional reagents are required as the sensing system is embedded within the alginate patch. Furthermore, the liquid hydrogel precursor allows the sensor patch to be molded into different shapes for various applications. This alginate hydrogel patch detects concentrations corresponding to those found in the residual H_2O_2 from the disinfection of the wound site during surgery (5 mM)[9] (**Scheme 2.1**). Past studies coated cellulose film with a layer of mesoporous silica to increase the surface area for anchorage of TMB.[19] In comparison, the alginate patch loaded with TMB-mesoporous silica particles generated higher positive blue color than the previous film, likely because the three-dimensional hydrogel patch significantly increases the loading amount of TMB than the two-dimensional film.

5.4 Conclusions

In conclusion, this study demonstrated a hydrogel patch that indicates the H_2O_2 level with visible color. The patch utilized the 3,3',5,5'-tetramethylbenzidine (TMB) as a source to generate the positive color via oxidation reaction catalyzed by horseradish peroxidase (HRP). By adsorbing TMB onto mesoporous silica particles, it was possible to disperse and immobilize TMB in the hydrogel and facilitate oxidation reaction to form a visible blue color. Upon exposure to the mixture of H_2O_2 and HRP, the TMB-silica particles generated intense blue color from the

production of blue charge-transfer complexes. In particular, the rod-shaped mesoporous silica particle with 7-nm pore diameter created the maximal intensity of blue color by limiting second oxidation reaction leading to the yellow diimine. The alginate patch loaded with these TMB-mesoporous silica particles generated the higher intensity of blue color upon exposure to H_2O_2 than the hydrated, micropore-free hydrogel. The detectable H_2O_2 concentration ranges from 25 to 5,000 μM. We propose that the design principles demonstrated in this study should be applicable to other strategies to incorporate enzyme-assisted and water-insoluble dyes into a wide array of hydrogel-based sensors.

5.5 Experimental methods

All materials were purchased from Sigma-Aldrich unless otherwise noted.

5.5.1 Synthesis of mesoporous silica microparticles with 2 nm pore diameter

Mesoporous silica microparticles with 2 nm pore diameter were synthesized by using a combination of previously reported methods.[20,21] Cetyltrimethylammonium bromide (0.5 g) was added to 96 mL of distilled water under stirring. After the solution turned clear, 34 mL of ethanol was added and then 10 mL of aqueous ammonia solution was added to the system. The mixture was mixed for 5 min. Then, 2.0 mL of tetraethyl orthosilicate (TEOS) was poured into the solution immediately under stirring. Stirring was continued for 3 hrs at room temperature. The solid product was recovered by filtration and dried at room temperature overnight. To remove TEOS from the pores, 5 mL ethanol per 100 mg solid was added and the resulting slurry was placed in an ultrasonic bath (40 kHz, Fisher FS-60) for 30 min at room temperature. The final product was recovered by vacuum filtration and was washed several times with ethanol and dried.

5.5.2 Synthesis of mesoporous silica microparticles with 7 nm pore diameter

Mesoporous silica microparticles with 7 nm pore diameter were synthesized by using a combination of previously reported methods.[22,23] Pluronic P123 [$EO_{20}PO_{70}EO_{20}$ (EO = ethylene oxide, PO = propylene oxide, Mn ~5,800 g/mol] (2 g) was dissolved in a mixture of 62.5 mL of deionized water and 12 mL of HCl (37%), followed by the addition of TEOS (4.12 g). The mixture was stirred at 40 °C for 2 hrs. The cloudy dispersion was then statically aged at 90 °C for 24 hrs. The precipitated product was isolated by vacuum filtration and was washed several times with hot distilled water and finally air-dried over 2 days. To remove Pluronic P123 entrapped in the pore channels, 50 mL methanol per 100 mg solid was added and the resulting slurry was placed in an ultrasonic bath for 20 min at room temperature. The final product recovered by vacuum filtration was washed with methanol and dried.

5.5.3 Synthesis of non-porous silica microparticles

Non-porous silica microparticles were prepared according to a modified Stöber method. Ethanol (73.8 mL), ammonium hydroxide (9.8 mL), distilled water (10.8 mL) were mixed at room temperature. TEOS (5.6 mL) was added all at once into the mixture. Cloudy mixture turned clear within 1 hr. The mixture was stirred for another 21 hrs. Particles were collected by centrifuge (4,000 rpm, 1 h) and washed with ethanol 4 times and water until the pH of the suspension became 7. The final product was dried by lyophilization.

5.5.4 Characterization of silica particles

Silica particles were suspended in acetone (1 mg/mL). Then, 10 µL of the suspension was transferred onto a carbon 200 mesh copper TEM grid (EMS) and left to dry in air overnight. TEM micrographs were captured using JEOL 2100 with an acceleration voltage of 200 kV. SEM micrographs were captured using Hitachi S-4800 at operating at 2.0 kV. Nitrogen gas adsorption–

desorption isotherms were obtained at 77 K with Quantachrome NOVA 2200e surface area and pore size analyzer. Before analysis, the sample was outgassed at 423 K under vacuum for 16 h. The specific surface area was calculated with the Brunauer–Emmett–Teller equation. The pore volume and diameter distribution were calculated from the adsorption curve by the Barrett–Joyner–Halenda method.

5.5.5 Quantification of TMB adsorbed on silica particles

3,3',5,5'-Tetramethylbenzidine (TMB) (TCI America) was dissolved in ethyl acetate or acetonitrile at 50 mg/mL or ethanol at 5 mg/mL. 0.6 mL of TMB solution was mixed with 220 mg of silica particles for 10 min at room temperature. To determine the adsorption efficiency, 2 mg of silica particles adsorbed with TMB was suspended in 1 mL PBS (pH 7). Particles were then centrifuged at 10,000 rpm for 30 min. The UV absorption spectra of the supernatant were obtained using UV-visible spectrophotometer (TECAN Infinite M200 Pro). Three replicates were used per condition.

5.5.6 Analysis of the oxidation reaction of TMB in silica particles with horseradish peroxidase (HRP) and H_2O_2

Silica particles loaded with TMB (2 mg), denoted as TMB-silica particles, were washed once with PBS. H_2O_2-diluted in PBS (50 µM) and HRP solution (0.2 U/mL) were mixed with the silica particles using a vortex mixer. UV-Vis absorbance scans from 250 – 650 nm of the oxidized suspension were obtained immediately after the reaction. Three replicates were used per condition.

5.5.7 Encapsulation of TMB-silica particles and HRP in the alginate patches

Alginate (100 mg, 0.5 mmol uronic acid, FMC Biopolymer Inc) was dissolved overnight in 0.1 M MES buffer (pH 6) at a concentration of 2.5%. Hydroxybenzotriazole (0.25 mmol), adipic

acid dihydrazide (0.01 mmol), TMB or TMB-loaded silica particles (same TMB concentration 10 mM) HRP (1 mL, 1 U/mL) were added sequentially under continuous stirring. 1-Ethyl-3-(3-dimethylaminopropyl)carbodiimide (0.25 mmol dissolved in 0.1 mL MES buffer) was then added, mixed quickly and poured between glass plates with 1 mm spacer. Gels disks with 10 mm diameter were punched out and left in 30 mL of PBS to swell overnight. To make microporous alginate foams loaded with TMB and HRP, gel disks were frozen at -20 °C and lyophilized under vacuum. The resulting micropores were confirmed with Leica DMi1 inverted microscope attached with Leica DFC295 digital microscope color camera.

5.5.8 Evaluation of colored response in the presence of H_2O_2

Hydrogel disks were placed on a filter paper and 20 µL of H_2O_2-PBS mixture (25 to 5,000 µM) was added on top of each disk. Images of the disks were captured immediately. For the quantification of reaction rates, images were captured every 10s in the first minute of reaction. Each condition was repeated with at least five replicates each time. Optical images were captured with Leica S6 E stereomicroscope attached with Leica EC4 HD color microscope camera and the color intensities were quantified using the ImageJ software.

5.5.9 Statistical Analysis

The results were presented as mean ± standard deviation. Three samples were analyzed per condition unless otherwise specified. Student's t-tests with unequal or equal variance were used to compare differences between pairs of experimental populations. One-way ANOVA tests (OriginLab) followed by Tukey's post-hoc test were used to compare differences between more than two experimental populations using a single factor. Data were considered significant for $p < 0.05$.

5.6 Scheme, Figures, Tables and Equations

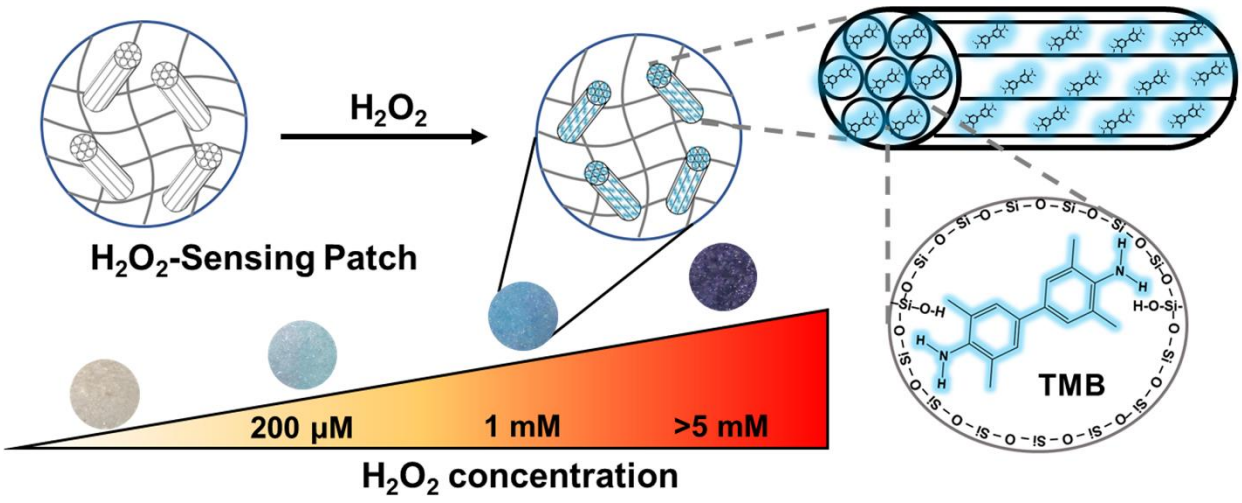

Scheme 5.1. H_2O_2-responsive colorimetric patch. The 3,3',5,5'-tetramethylbenzidine (TMB)-loaded nanoporous silica microparticles are encapsulated into an alginate patch with controlled microporous structure. Upon exposure to H_2O_2 TMB is oxidized to produce colored complexes. The color intensity is orchestrated by the pore structure of silica particles and the alginate matrix.

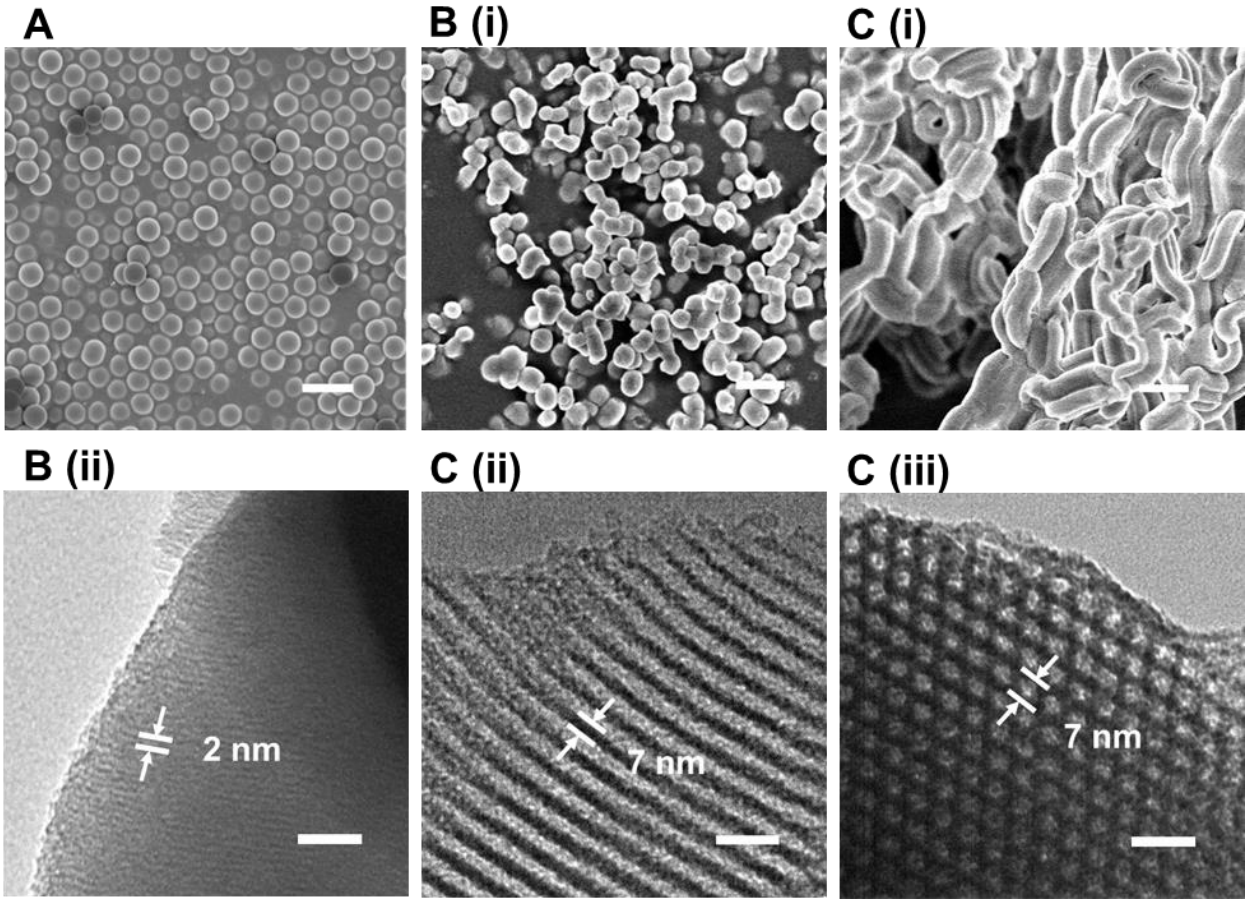

Figure 5.1. Micrographs of (A) spherical, non-porous silica particles, (B) spherical, mesoporous silica particles with 2 nm-diameter pores, and (C) rod-shaped, mesoporous silica particles with 7 nm-diameter pores. The micrographs on the first row were captured by SEM and those on the second row were captured by TEM. Scale bars in micrographs on the first row and those on the second row represent 1 μm and 20 nm, respectively. *Data was obtained together with Yongbeom Seo.*

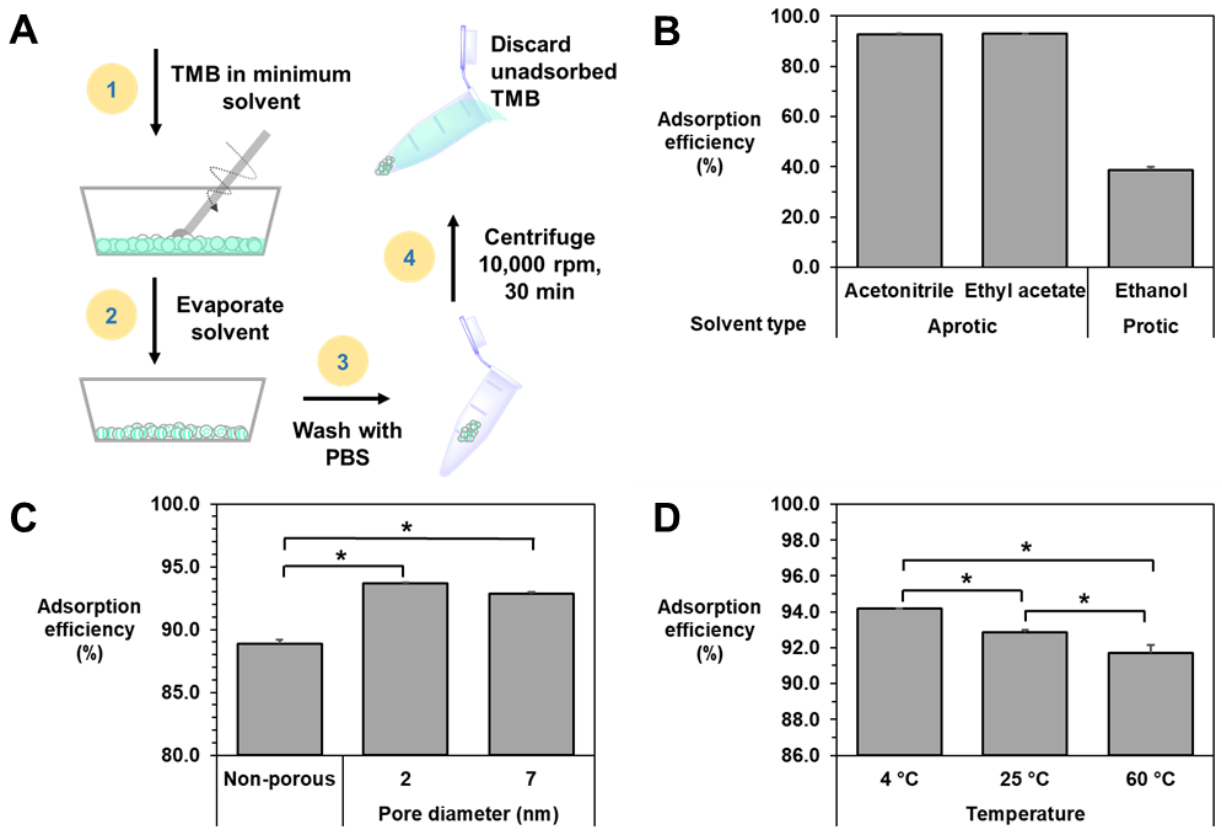

Figure 5.2. Analysis of the adsorption efficiency of TMB on or in the silica particles. (A) Schematic depicting the incipient wetness impregnation process to load TMB on or in the silica particles. (B) Effects of solvents on the adsorption efficiency of TMB in the mesoporous silica with pores of 7 nm-diameter. (C) Effects of the porous structure of silica particles on the adsorption efficiency of TMB. Ethyl acetate was used as a solvent of TMB. (D) Effects of the temperature on the adsorption efficiency of TMB in the mesoporous silica particles with pores of 7 nm-diameter. Ethyl acetate was used as a solvent of TMB. In (C) and (D), * represents the statistical significance of the difference of values between conditions indicated with line (*$p < 0.05$).

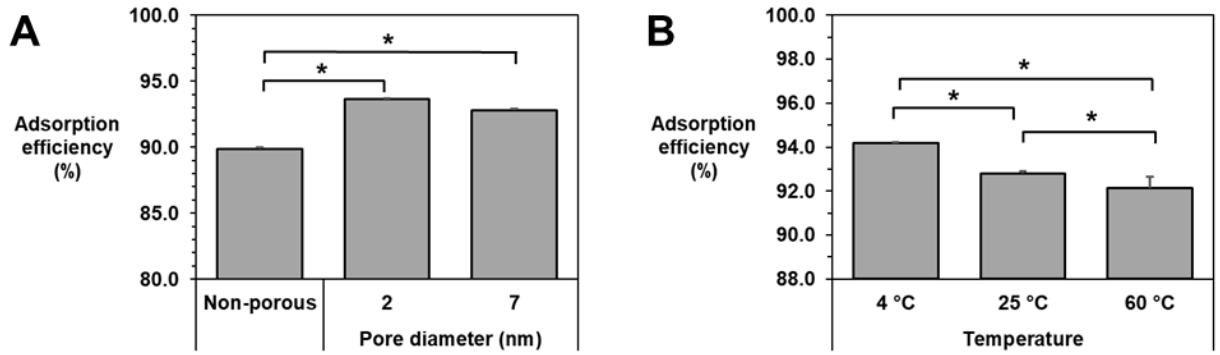

Figure 5.3. Analysis of the adsorption efficiency of TMB on or in the silica particles. Acetonitrile was used as a solvent of TMB (A) Effects of the porous structure of silica particles on the adsorption efficiency of TMB. (B) Effects of the temperature on the adsorption efficiency of TMB in the mesoporous silica particles with pores of 7 nm-diameter. * represents the statistical significance of the difference of values between conditions indicated with the line (*$p < 0.05$).

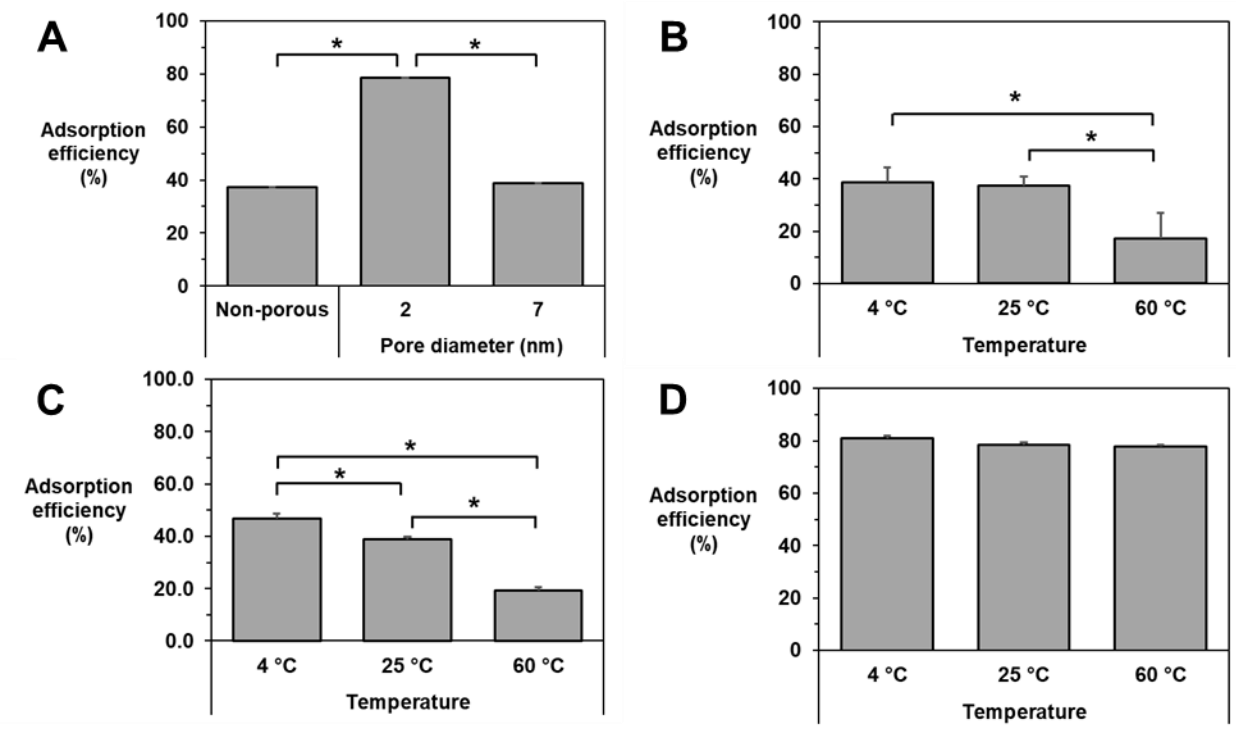

Figure 5.4. Analysis of the adsorption efficiency of TMB on or in the silica particles. Ethanol was used as a solvent of TMB. (A) Effects of the porous structure of silica particles on the adsorption efficiency of TMB. (B) Effects of the temperature on the adsorption efficiency of TMB on non-porous silica particles, (C) in the mesoporous silica particles with pores of 7 nm-diameter and (D) in the mesoporous silica particles with pores of 2 nm-diameter * represents the statistical significance of the difference of values between conditions indicated with the line (*$p < 0.05$).

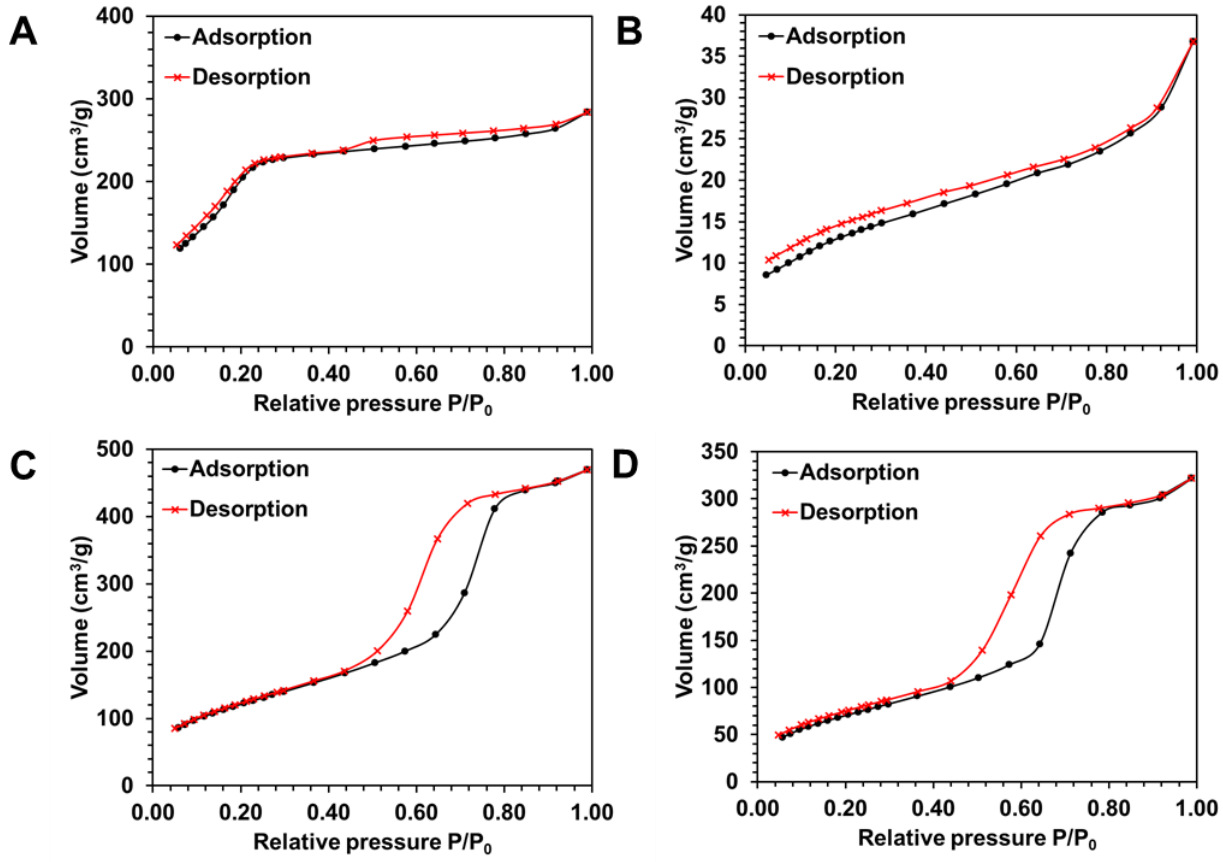

Figure 5.5. Nitrogen gas adsorption–desorption isotherms of mesoporous silica with pore diameter of 2 nm (A) before and (B) after TMB adsorption. Mesoporous silica with pore diameter of 7 nm (C) before and (D) after TMB adsorption. The adsorption and desorption curves are marked in black and red, respectively. Ethyl acetate was used as a solvent for TMB. *Data was provided by Sang-Hyon Chu.*

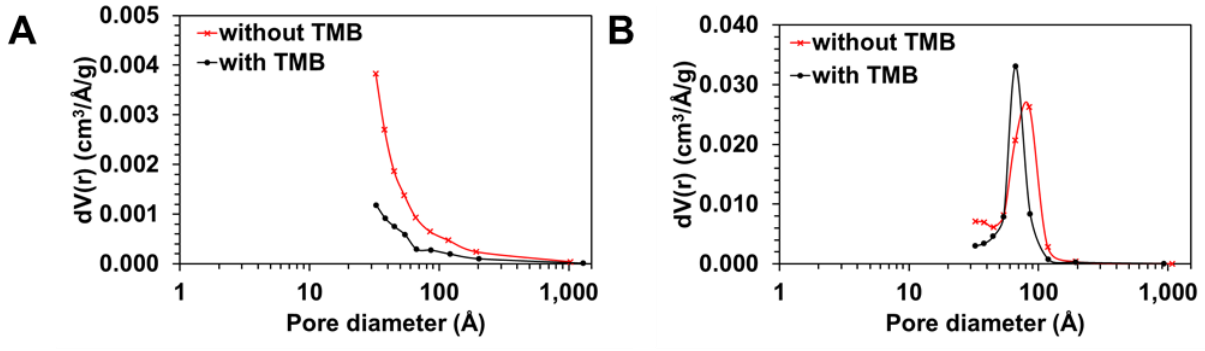

Figure 5.6. Pore diameter distribution of (A) mesoporous silica with 2 nm pore diameter and (B) mesoporous silica with 7 nm pore diameter, with or without TMB marked by in black and red, respectively. Ethyl acetate was used as a solvent for TMB.

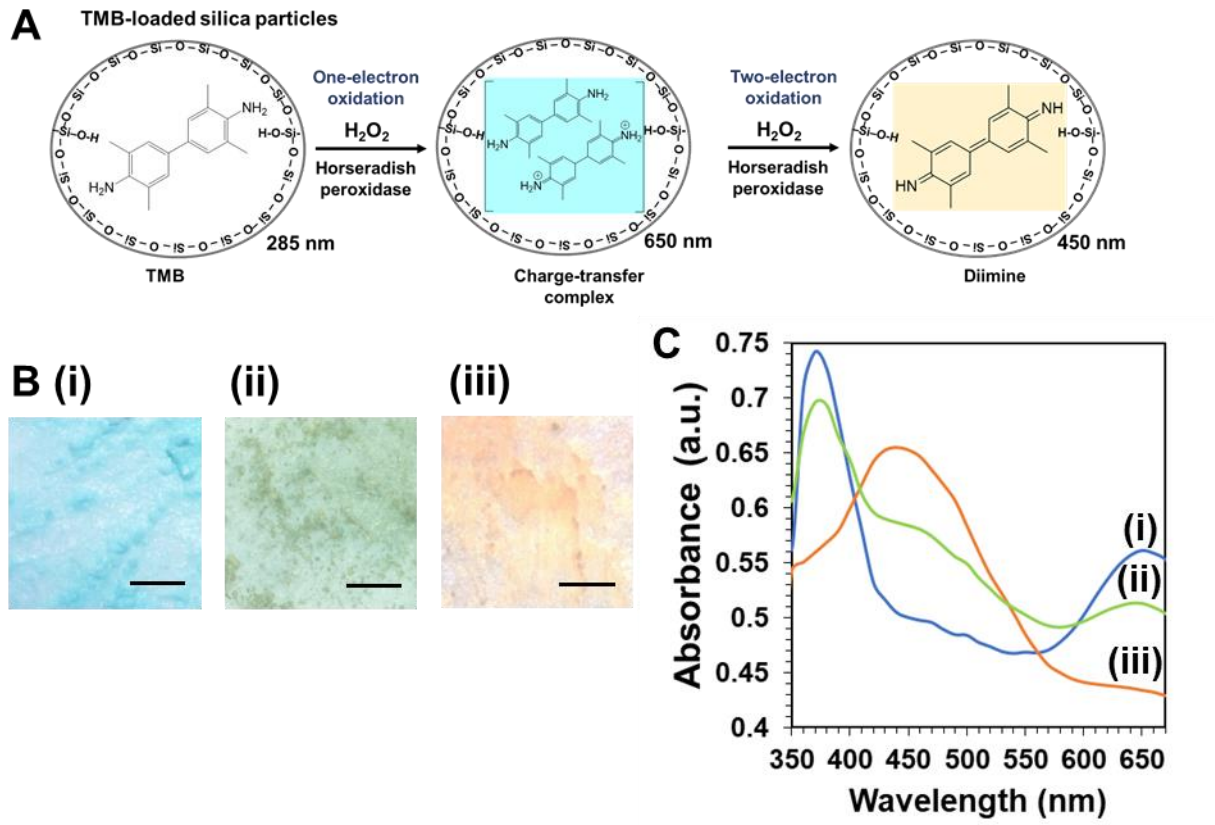

Figure 5.7. Analysis of colored products resulting from oxidation of TMB by H_2O_2 and horseradish peroxidase (HRP). (A) Schematic depicting the sequential oxidation reaction. Upon oxidation by H_2O_2 catalyzed by HRP, TMB forms a blue charge-transfer complex. Upon another oxidation step by H_2O_2 catalyzed by HRP, the blue charge-transfer complex forms a yellow diimine as the final product. Absorbance values of the compounds are denoted on the bottom right corners. (B) Optical micrographs of the different TMB-loaded silica particles after the oxidation reaction with 50 µM of H_2O_2 and 0.2 U/mL HRP. The silica particles were loaded with TMB using ethyl acetate as the solvent. (i) Suspension of TMB-loaded (i) mesoporous silica particles with 7 nm-pore diameter, (ii) mesoporous silica particles with 2 nm-pore diameter, (iii) non-porous silica particles. Scale bar represents 2 mm. (C) UV-Vis absorption spectra of the respective suspended silica particles shown in (B). Curves represent the spectra of (i) blue charge-transfer complexes, (ii) mixture of blue complexes and yellow diimine, and (iii) yellow diimine formed on the silica particles.

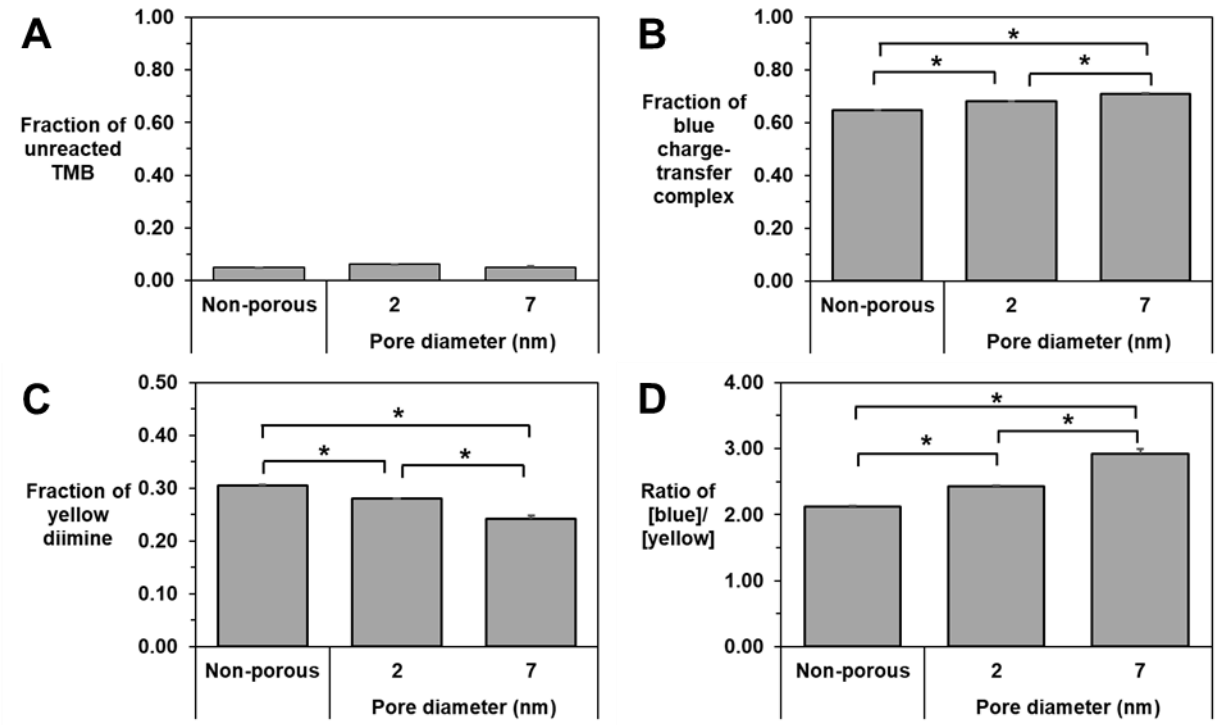

Figure 5.8. Quantitative analysis of the oxidation of TMB loaded on non-porous silica particles or mesoporous silica particles. Ethyl acetate was used as a solvent of TMB. (A) Fraction of unreacted TMB after oxidation with H_2O_2. Fractions of (B) blue charge-transfer complex and (C) yellow diimine formed from the oxidation of TMB. (D) Ratio of blue complexes to yellow diimine. * represents the statistical significance of the difference of values between conditions indicated with line ($*p < 0.05$).

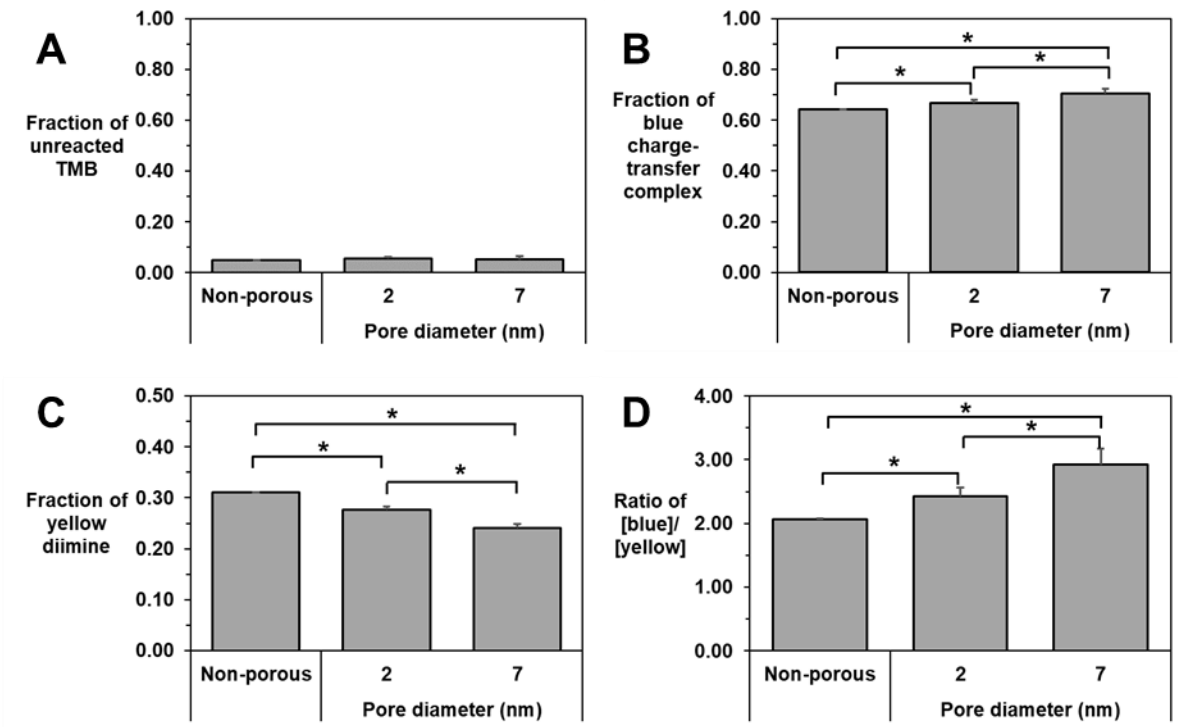

Figure 5.9. Quantitative analysis of the oxidation of TMB loaded on non-porous silica particles or mesoporous silica particles. Acetonitrile was used as a solvent of TMB. (A) Fraction of unreacted TMB after oxidation with H_2O_2. Fractions of (B) blue complexes and (C) yellow diimine formed from the oxidation of TMB. (D) Ratio of blue complexes to yellow diimines. * indicates the statistical significance of the difference of values between conditions indicated with line (*$p < 0.05$).

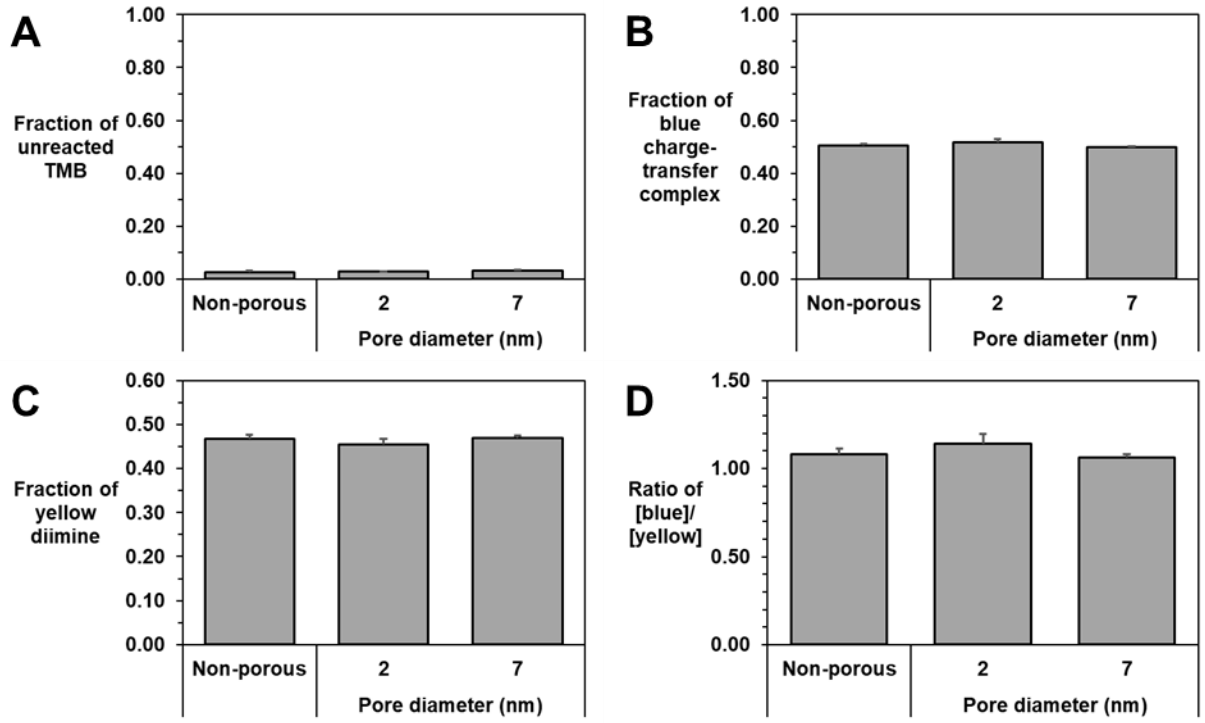

Figure 5.10. Quantitative analysis of the oxidation of TMB-loaded on non-porous silica particles and mesoporous silica particles. Ethanol was used as a solvent of TMB. (A) Fraction of unreacted TMB after oxidation with H_2O_2. Fractions of (B) blue complexes and (C) yellow diimine formed from the oxidation of TMB. (D) Ratio of blue complexes to yellow diimine. * indicates the statistical significance of the difference of values between conditions indicated with line ($*p < 0.05$).

.

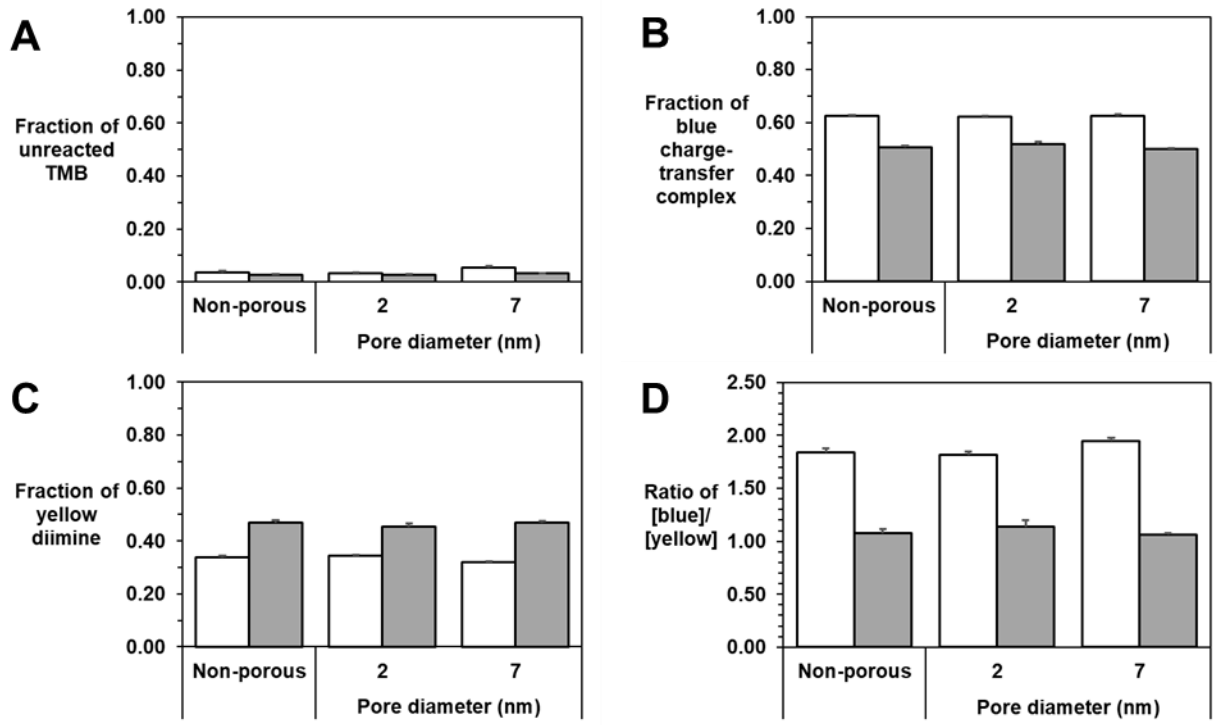

Figure 5.11. Quantitative analysis of the oxidation of TMB immobilized on non-porous silica particles and mesoporous silica particles. The oxidation level was also tuned by the concentration of horseradish peroxidase. The open and filled bars represent the 0.02 U/mL and 0.2 U/mL horseradish peroxidase, respectively. The TMB was dissolved in ethanol. (A) Fraction of unreacted TMB after oxidation with H_2O_2. Fraction of (B) blue complexes and (C) yellow diimines formed from the oxidation of TMB. (D) Ratio of blue complexes to yellow diimine. * indicates the statistical significance of the difference of values between conditions indicated with line (*$p < 0.05$).

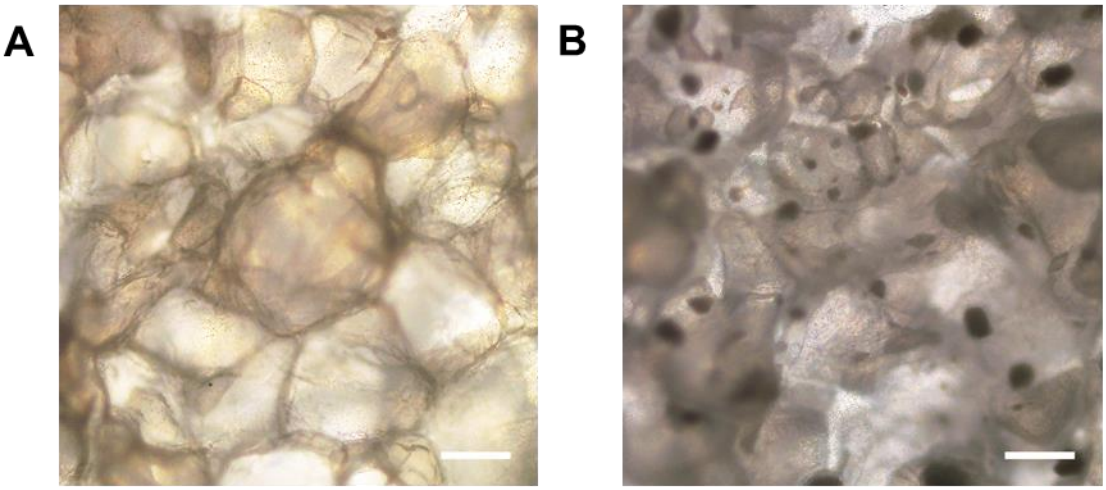

Figure 5.12. Optical images of micropores in the lyophilized, microporous alginate matrix. The matrix was loaded with (A) free TMB and (B) rod-shaped mesoporous silica microparticles with pore diameter of 7 nm. In (B), dark objects are the mesoporous silica particles. Scale bars represent 100 μm.

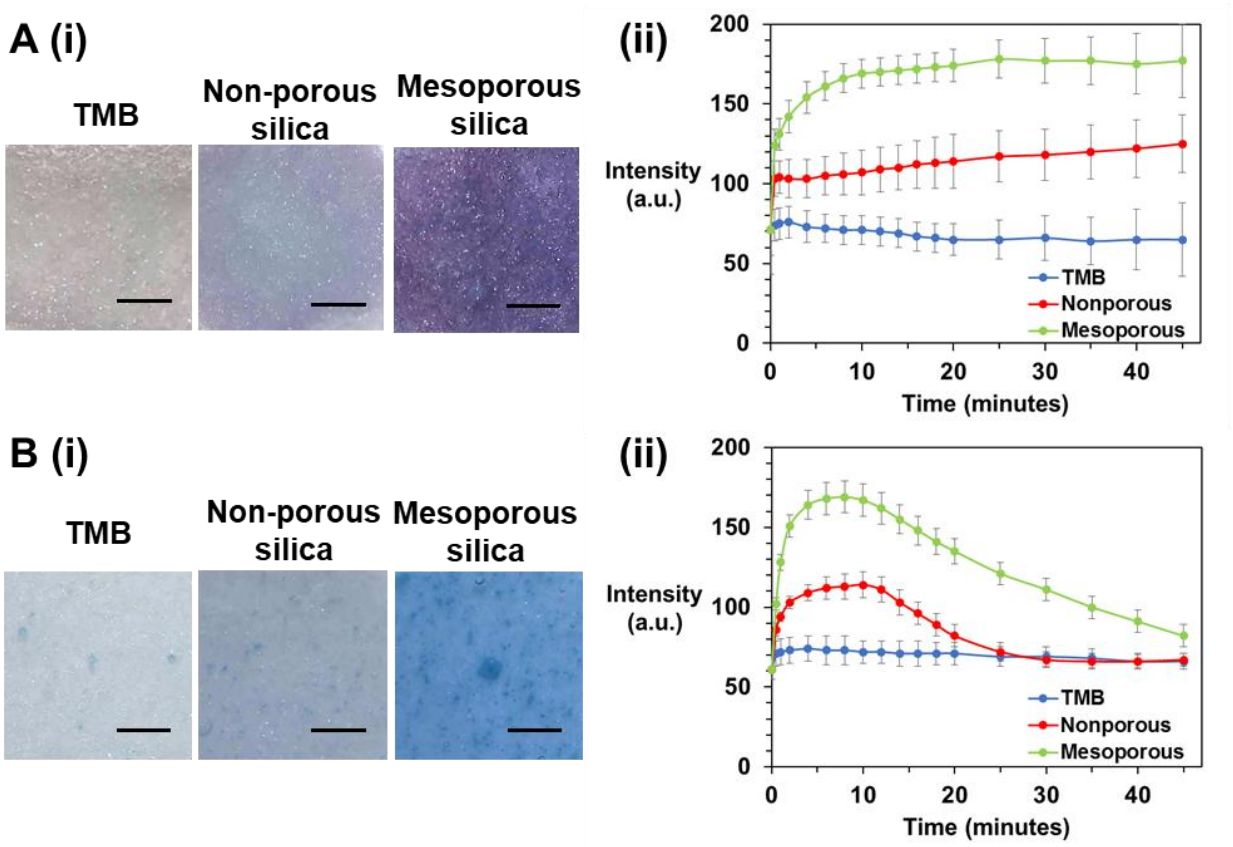

Figure 5.13. Effects of the porous structure of silica microparticles and water content in the alginate matrix on the intensity of blue color generated by the oxidation of TMB**.** (A-i) Optical micrographs of microporous patches encapsulated with free TMB, TMB-loaded non-porous silica particles, and TMB-loaded mesoporous silica microparticles after reaction time of 4 min. The H_2O_2 added was kept constant at 20 µL of 5 mM H_2O_2. Scale bar represents 2 mm. (A-ii) Change of the average blue color intensity from patches over time. Error bars denote standard deviations. (B-i) Optical micrographs of hydrogels encapsulated with free TMB, TMB-loaded non-porous silica particles, and TMB-loaded mesoporous silica microparticles after reaction time of 4 min. The H_2O_2 added was kept constant at 20 µL of 5 mM H_2O_2. Scale bar represents 2 mm. (B-ii) Change of the average blue color intensity from hydrogels over time. Error bars denote standard deviations. In (ii), blue, red, and green curves represent the hydrogel encapsulated with free TMB, TMB-loaded non-porous silica particles, and TMB-loaded mesoporous silica microparticles, respectively. The concentrations of free TMB and TMB-loaded in silica particles were kept the same at 2 mg per 100 mg alginate.

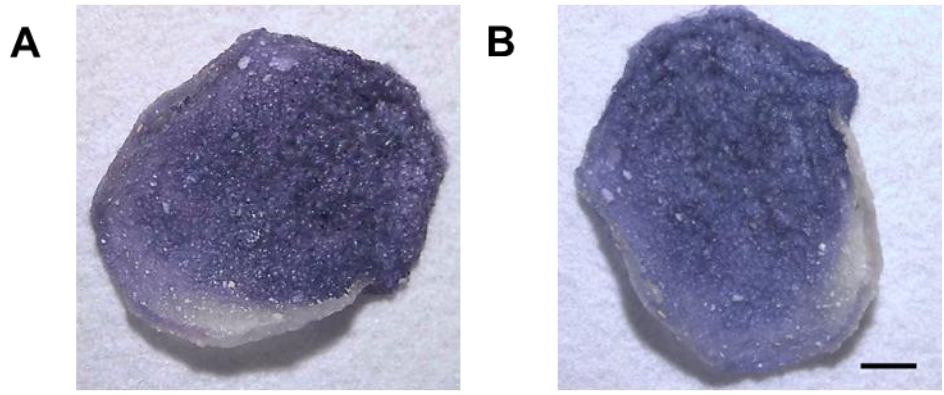

Figure 5.14. Images of the microporous alginate patches encapsulated with TMB-loaded mesoporous silica particles. The images were captured after addition of 5 mM H_2O_2 solution to the microporous patches. The pore diameter of the mesoporous silica microparticles was kept constant at 7 nm. The images show the comparison of the same disk 1 hour after the addition of H_2O_2 (A) and 1 week (B). Scale bar represents 2 mm.

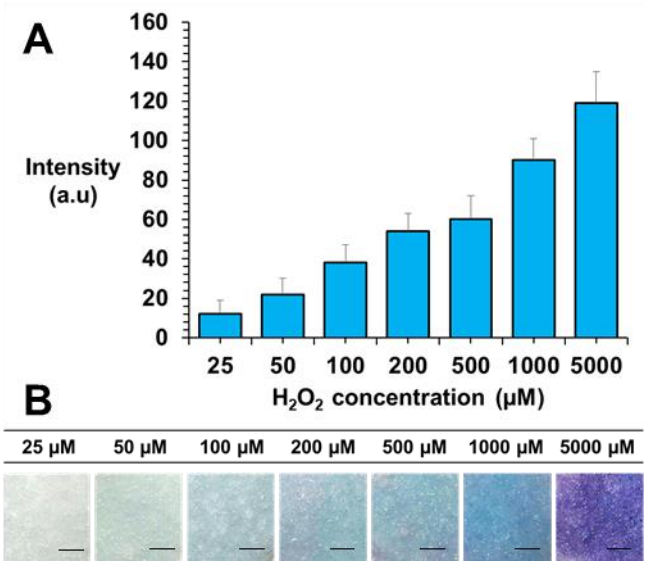

Figure 5.15. Effects of H_2O_2 concentration on the intensity of blue color from the microporous alginate patches encapsulated with TMB-loaded mesoporous silica particles. (A) Keeping the volume of H_2O_2 added constant at 20 µL, the color intensity was increased with increasing H_2O_2 concentration from 25 to 1000 µM. Error bars denote standard deviations. (B) Optical images of the patches with increasing H_2O_2 concentration. Rod-shaped mesoporous silica particle with pore diameter of 7 nm was used in this study. The concentration of TMB-loaded in mesoporous silica particles in the gel was kept constant at 2 mg per 100 mg alginate. Scale bar represents 2 mm.

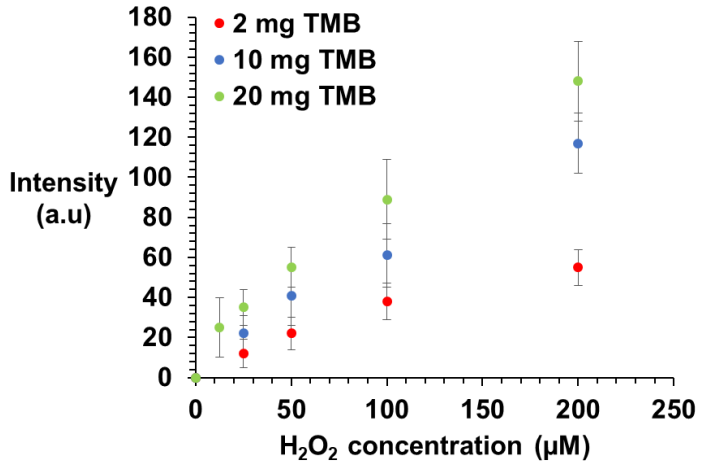

Figure 5.16. Effects of H_2O_2 concentration on the intensity of blue color from the microporous alginate patches encapsulated with TMB-silica particles. Keeping the volume of H_2O_2 added constant at 20 μL, the color intensity was increased with increasing H_2O_2 concentration from 25 to 200 μM. Rod-shaped mesoporous silica particle with pore diameter of 7 nm was used in this study. The sensitivity of the patches to H_2O_2 was increased by increasing the original TMB loading mass from 2 mg to 10 mg or 20 mg, marked by the circles in red, blue and green, respectively.

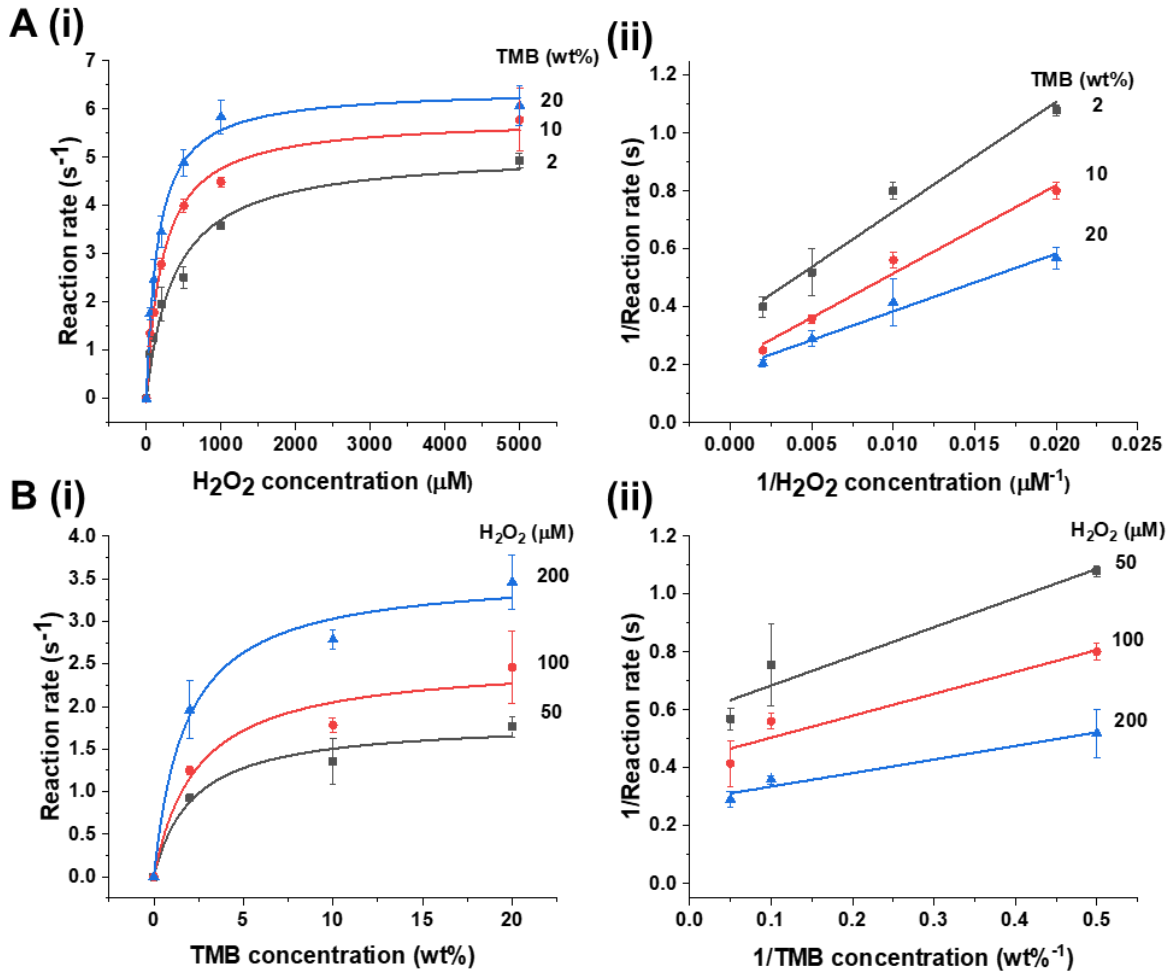

Figure 5.17. Kinetics of TMB oxidation by HRP in the alginate patches loaded with rod-shaped mesoporous silica particle with 7 nm-diameter pores. (A) Oxidation kinetics modulated by the H_2O_2 concentration at constant TMB concentrations of 2, 10 and 20 wt%. (A-i) Oxidation reaction rate plot. (A-ii) Plots of the 1/oxidation reaction rate versus $1/H_2O_2$ concentration. (B) Oxidation kinetics modulated by the TMB concentration at constant H_2O_2 concentrations of 50, 100 and 200 μM. (B-i) Oxidation reaction rate plot. (B-ii) Plots of the 1/oxidation reaction rate versus 1/TMB concentration. In (A) and (B), the concentration of TMB-mesoporous silica particles in the gel was kept constant at 10 wt%. The data points in (A-i) and (B-i) were fitted by the Michaelis-Menten model, represented by solid curves. Separately, the data points in (A-ii) and (B-ii) were fitted by the Lineweaver-Burk model, represented by the solid lines.

Table 5.1. The table shows pore diameter, pore volume and specific surface area.

Entry	Type	Pore diameter (nm) by TEM	Pore diameter[a] (nm)	Pore volume[a] ($cm^3\ g^{-1}$) without/with TMB	Specific surface area[b] ($m^2\ g^{-1}$) without/with TMB
1	**Mesoporous**	2	3.2/3.3	0.10/0.04	811/50
2	**Mesoporous**	7	8.5/6.6	0.67/0.49	450/274

[a] The pore diameter and pore volume were calculated using the adsorption curve using the Barrett-Joyner-Halenda method.

[b] The specific surface area was calculated with the Brunauer–Emmett–Teller (BET) equation.

Table 5.2. Kinetic parameters K_m and V_{max} for H_2O_2 and TMB for HRP-mediated oxidation in the patches.

		Michaelis-Menten Model		Lineweaver-Burk Model	
	Concentration (wt%)	**K_m (μM)**	**V_{max} (s^{-1})**	**K_m (μM)**	**V_{max} (s^{-1})**
TMB	2	379 ± 74	5.1 ± 0.3	332 ± 4	4.7 ± 0.6
	10	219 ± 25	5.8 ± 0.2	169 ± 3	5.3 ± 0.4
	20	153 ± 14	6.4 ± 0.2	129 ± 1	6.0 ± 0.4
	Concentration (μM)	**K_m (wt%)**	**V_{max} (s^{-1})**	**K_m (wt%)**	**V_{max} (s^{-1})**
H_2O_2	50	2.2 ± 0.9	1.8 ± 0.2	1.7 ± 0.2	1.7 ± 0.2
	100	2.4 ± 1	2.5 ± 0.3	1.8 ± 0.2	2.3 ± 0.4
	200	1.8 ± 0.6	3.6 ± 0.3	1.9 ± 0.1	3.5± 0.3

Equation 5.1

Equations to calculate the molar fraction of unreacted TMB, blue charge-transfer complex and yellow diimine after the oxidation reaction

$$\text{Molar concentration of blue charge-transfer complex} = \frac{A_{650}}{\varepsilon(\text{blue charge-transfer complex at 650 nm})}$$

Where A_{650} represents the magnitude of UV-visible light absorption at 650 nm and ε (blue charge-transfer complex at 650 nm) represents the molar absorption coefficient of blue charge-transfer complex at 650 nm.

$$\text{Molar fraction of blue charge-transfer complex} = \frac{\text{molar mass of blue charge-transfer complex}}{\text{molar mass of unreacted TMB} + \text{blue charge-transfer complex} + \text{yellow diimine}}$$

Equation 5.2

Michaelis-Menten equation

$$\text{Reaction rate}, V_0 = \frac{V_{max}[H_2O_2]}{[H_2O_2] + K_m}$$

$$\text{Reaction rate}, V_0 = \frac{V_{max}[TMB]}{[TMB] + K_m}$$

Equation 5.3

Lineweaver-Burk equation

$$\frac{1}{V_0} = \frac{K_M}{V_{max}}\frac{1}{[H_2O_2]} + \frac{1}{V_{max}}$$

$$\frac{1}{V_0} = \frac{K_M}{V_{max}}\frac{1}{[TMB]} + \frac{1}{V_{max}}$$

5.7 References

(1) Linley, E.; Denyer, S. P.; McDonnell, G.; Simons, C.; Maillard, J. Y. Use of Hydrogen Peroxide as a Biocide: New Consideration of Its Mechanisms of Biocidal Action. *J. Antimicrob. Chemother.* **2012**, *67*, 1589–1596.

(2) Özkan, M.; Yemenicioğlu, A.; Cemeroğlu, B. Degradation of Various Fruit Juice Anthocyanins by Hydrogen Peroxide. *Food Res. Int.* **2005**, *38*, 1015–1021.

(3) Lillard, H. S.; Thomson, J. E. Efficacy of Hydrogen Peroxide as a Bactericide in Poultry Chiller Water. *J. Food Sci.* **1983**, *48*, 125–126.

(4) McWatters, K. H.; Hashim, I. B.; Walker, S. L.; Doyle, M. P.; Rimal, A. P. Acceptability of Lettuce Treated with Lactic Acid and Hydrogen Peroxide Antibacterial Solution. *J. Food Qual.* **2001**, *25*, 223–242.

(5) Schafer, M.; Werner, S. Oxidative Stress in Normal and Impaired Wound Repair. *Pharmacol. Res.* **2008**, *58*, 165–171.

(6) O'Toole, E. A.; Goel, M.; Woodley, D. T. Hydrogen Peroxide Inhibits Human Keratinocyte Migration. *Dermatologic Surg.* **1996**, *22*, 525–529.

(7) Senel, O.; Cetinkale, O.; Ozbay, G.; Ahçioğlu, F.; Bulan, R. Oxygen Free Radicals Impair Wound Healing in Ischemic Rat Skin. *Ann. Plast. Surg.* **1997**, *39*, 516–523.

(8) Rasik, A. M.; Shukla, A. Antioxidant Status in Delayed Healing Type of Wounds. *Int. J. Exp. Pathol.* **2001**, *81*, 257–263.

(9) Loo, A. E. K.; Wong, Y. T.; Ho, R.; Wasser, M.; Du, T.; Ng, W. T.; Halliwell, B. Effects of Hydrogen Peroxide on Wound Healing in Mice in Relation to Oxidative Damage. *PLoS One* **2012**, *7*, e49215.

(10) Wen, F.; Dong, Y.; Feng, L.; Wang, S.; Zhang, S.; Zhang, X. Horseradish Peroxidase Functionalized Fluorescent Gold Nanoclusters for Hydrogen Peroxide Sensing. *Anal. Chem.* **2011**, *83*, 1193–1196.

(11) Dickinson, B. C.; Huynh, C.; Chang, C. J. A Palette of Fluorescent Probes with Varying Emission Colors for Imaging Hydrogen Peroxide Signaling in Living Cells. *J. Am. Chem. Soc.* **2010**, *132*, 5906–5915.

(12) Bas, S. Z.; Cummins, C.; Borah, D.; Ozmen, M.; Morris, M. A. Electrochemical Sensing of Hydrogen Peroxide Using Block Copolymer Templated Iron Oxide Nanopatterns. *Anal. Chem.* **2018**, *90*, 1122–1128.

(13) Munnik, P.; De Jongh, P. E.; De Jong, K. P. Recent Developments in the Synthesis of Supported Catalysts. *Chem. Rev.* **2015**, *115*, 6687–6718.

(14) Roy, D.; Liu, S.; Woods, B. L.; Siler, A. R.; Fourkas, J. T.; Weeks, J. D.; Walker, R. A.

Nonpolar Adsorption at the Silica/Methanol Interface: Surface Mediated Polarity and Solvent Density across a Strongly Associating Solid/Liquid Boundary. *J. Phys. Chem. C* **2013**, *117*, 27052–27061.

(15) Xiong, Y.; Cao, T.; Chen, Q.; Li, Z.; Yang, Y.; Xu, S.; Yuan, S.; Sjoblom, J.; Xu, Z. Adsorption of a Polyaromatic Compound on Silica Surfaces from Organic Solvents Studied by Molecular Dynamics Simulation and AFM Imaging. *J. Phys. Chem. C* **2017**, *121*, 5020–5028.

(16) Wu, D.; Guo, X.; Sun, H.; Navrotsky, A. Energy Landscape of Water and Ethanol on Silica Surfaces. *J. Phys. Chem. C* **2015**, *119*, 15428–15433.

(17) Kakran, M.; Antipina, M. N. Emulsion-Based Techniques for Encapsulation in Biomedicine, Food and Personal Care. *Curr. Opin. Pharmacol.* **2014**, *18*, 47–55.

(18) Porter, D. J. T.; Bright, H. J. The Mechanism of Oxidation of Nitroalkanes by Horseradish-Peroxidase. *J. Biol. Chem.* **1983**, *258*, 9913–9924.

(19) Jiang, Y.; Wang, W.; Li, X.; Wang, X.; Zhou, J.; Mu, X. Enzyme-Mimetic Catalyst-Modified Nanoporous SiO2 -Cellulose Hybrid Composites with High Specific Surface Area for Rapid H2O2 Detection. *ACS Appl. Mater. Interfaces* **2013**, *5*, 1913–1916.

(20) Meléndez-Ortiz, H. I.; García-Cerda, L. A.; Olivares-Maldonado, Y.; Castruita, G.; Mercado-Silva, J. A.; Perera-Mercado, Y. A. Preparation of Spherical MCM-41 Molecular Sieve at Room Temperature: Influence of the Synthesis Conditions in the Structural Properties. *Ceram. Int.* **2012**, *38*, 6353–6358.

(21) Jabariyan, S.; Zanjanchi, M. A. A Simple and Fast Sonication Procedure to Remove Surfactant Templates from Mesoporous MCM-41. *Ultrason. Sonochem.* **2012**, *19*, 1087–1093.

(22) Sadeghzadeh, S. M. Ultrasound-Promoted Green Approach for the Synthesis of Thiazoloquinolines Using Gold(Iii) Dipyridine Complex Immobilized on SBA-15 as Nano Catalysts at Room Temperature. *RSC Adv.* **2015**, *5*, 68947–68952.

(23) Pirez, C.; Wilson, K.; Lee, A. F.; Clark, J. H.; Choi, M.; Fajula, F.; Wilson, K. An Energy-Efficient Route to the Rapid Synthesis of Organically-Modified SBA-15 via Ultrasonic Template Removal. *Green Chem.* **2014**, *16*, 197–202.

CHAPTER 6: Conclusions and Future Directions

6.1 Conclusions

This dissertation described design strategies to utilize inflammatory molecules to control reactions at the nanoscale. Specifically, TNFα and H_2O_2 were combined with different aspects of nanoparticle design to discover new ways to enhance therapeutic drugs and diagnostics.

Firstly, the liposome surface was modified to present hyaluronic acid to bind onto the cellular membrane of adipose-derived stem cells. Adipose-derived stem cells carrying the liposomes were stimulated in situ by the gradual release of the loaded cytokine TNFα. This treatment to an ischemic leg enhanced the recovery of blood perfusion and the affected muscles.

Next, the hydrophobic-to-hydrophilic phase change was triggered by H_2O_2 in diblock copolymers functionalized with a micelle-swelling thioether group. The on demand release and swelling using the reactive oxygen species found in the tumor microenvironment increased the accumulation of drug molecules in the tumors of an aggressive form of prostate cancer.

Finally, the porosity of mesoporous materials was investigated for their adsorption capacity and implications the oxidation reaction for a H_2O_2 level reporter chromophore. Additionally, we demonstrated the potential to create a hybrid material that harnesses the high surface area of the mesoporous materials and the versatility to be molded into several shapes of a cross-linked hydrogel.

Overall, the results from these research projects serve to better understand the design principles for engineering nanoparticles with pathological biomolecules. The technologies developed were demonstrated in models that have a large impact on the world, such as debilitating medical conditions, specifically cancer and ischemia and the use of H_2O_2. The key findings could be used as a guide for future developments for deeper understanding of these real-world problems.

6.2 Future directions

The inflammatory microenvironment is abundant with pro-inflammatory signaling molecules and reactive species. The results from this dissertation are a mere few examples of several possible ways to utilize these potent signaling molecules for enhanced nanoparticle design. The research projects mentioned could be extended with these suggested directions.

In Chapter 3, the interaction between the nanoparticle and cell surface was solely dependent on hyaluronic acid and CD44 ligand-receptor electrostatic attraction. Reinforcement of the nanoparticle-cell binding will be critical if the shear stress exerted by fluid flow of the surrounding media is larger than the nanoparticle-cell binding force. To increase stability of the physical interaction between the nanoparticle and cell surface, additional ligands may be added on the nanoparticle surface. Mesenchymal stem cells from the adipose tissue also express high levels of receptors for fibronectin, integrin αV/β1.[1] Therefore, the liposomes could be modified to present the tripeptide recognition sequence, arginine-glycine-aspartic acid (RGD).[2] RGD peptides presented on nanoparticles results in multiple interactions with integrins on a cell membrane. The immobilization of RGD peptides increases the density of RGD peptides and hence increases the strength of nanoparticle-cell binding.[3] Alternatively, injectable hydrogels may be used to encapsulate the cells. The hydrogel needs to have a moderate shear thinning property for the hydrogel to be administered through a syringe and needle. The layer of hydrogel near the walls should undergo shear thinning to form a fluid and act as a lubricant. At the same time, the rest of the hydrogel remains intact. The retained structural integrity of the hydrogel protects the cells from shear by linear flow.[4] Therefore, studies focused on determining the impact of flow on the behavior cells is essential to determine if the engineered cells retained their function from the syringe to the place of transplantation.

In Chapter 4, the swelling behavior of nanoparticles was demonstrated in a cancer model. The objective was to reduce the outward diffusion of nanoparticles back into the blood vessels. However, this application is not limited to cancer. Other diseases including bacterial and viral infections also lead to increased permeability of the endothelium.[5–7] The microenvironment during the fight between the immune cells and invading bacteria is also oxidizing as immune cells release reactive oxygen species to kill the pathogens. Thus, the reactive oxygen species-responsive micelles could be used to deliver antibiotics. The swelling mechanism increases the specificity of the antibiotics release. It will be advantageous if this strategy reduces the dose required and avoid the non-specific killing of commensal beneficial bacterial found in the gut.

In Chapter 5, the chromophore was used to detect the presence of H_2O_2 that was used to remove microbes. However, aerobic cells including bacteria and fungi produce an enzyme called catalase that neutralizes reactive oxygen species such as H_2O_2 by decomposing H_2O_2 to water and oxygen gas. Therefore, higher concentrations of H_2O_2 would be necessary to overcome this protective mechanism. A bacterial detector could complement the current sensor to determine if the H_2O_2 treatment was effective. To do so, a liposome formed from 10,12-pentacosadiynoic acid could be functionalized with an antibody towards *Legionella pneumophila*, a water borne bacteria that is a health risk if aerosolized in a shower or air conditioning system. The crosslinked polydiacetylenes produces a visible blue color in solution.[8] Upon binding of bacteria to the conjugated antibodies, the crosslinks undergo a conformational change.[9] The more disordered and less coplanar structure results in a visible red color. This bacteria-responsive vesicle could be easily mixed into the current nanoporous and microporous hydrogel system.[10] However, the hydrogen peroxide sensor will have to be modified to present the yellow diimine as a positive signal to

complement the bacterial system which presents a blue color as a negative signal. In all, the development of both sensors promote the use of H_2O_2 as a green antimicrobial treatment.

6.3 References

(1) Goessler, U. R.; Bugert, P.; Bieback, K.; Stern-Straeter, J.; Bran, G.; Hormann, K.; Riedel, F. Integrin Expression in Stem Cells from Bone Marrow and Adipose Tissue during Chondrogenic Differentiation. *Int. J. Mol. Med.* **2008**, *21*, 271–279.

(2) Plow, E. F.; Haas, T. A.; Zhang, L.; Loftus, J.; Smith, J. W. Ligand Binding to Integrins. *J. Biol. Chem.* **2000**, *275*, 21785–21788.

(3) Montet, X.; Funovics, M.; Montet-Abou, K.; Weissleder, R.; Josephson, L. Multivalent Effects of RGD Peptides Obtained by Nanoparticle Display. *J. Med. Chem.* **2006**, *49*, 6087–6093.

(4) Aguado, B. A.; Mulyasasmita, W.; Su, J.; Lampe, K. J.; Heilshorn, S. C. Improving Viability of Stem Cells During Syringe Needle Flow Through the Design of Hydrogel Cell Carriers. *Tissue Eng. Part A* **2012**, *18*, 806–815.

(5) Coureuil, M.; Lécuyer, H.; Bourdoulous, S.; Nassif, X. A Journey into the Brain: Insight into How Bacterial Pathogens Cross Blood-Brain Barriers. *Nat. Rev. Microbiol.* **2017**, *15*, 149–159.

(6) Puerta-Guardo, H.; Glasner, D. R.; Harris, E. Dengue Virus NS1 Disrupts the Endothelial Glycocalyx, Leading to Hyperpermeability. *PLoS Pathog.* **2016**, *12*, e1005738.

(7) Kumar, P.; Shen, Q.; Pivetti, C. D.; Lee, E. S.; Wu, M. H.; Yuan, S. Y. Molecular Mechanisms of Endothelial Hyperpermeability: Implications in Inflammation. *Expert Rev. Mol. Med.* **2009**, *11*, e19.

(8) Vigneshvar, S.; Sudhakumari, C. C.; Senthilkumaran, B.; Prakash, H. Recent Advances in Biosensor Technology for Potential Applications – An Overview. *Front. Bioeng. Biotechnol.* **2016**, *4*, 11.

(9) Tao, H.; Marelli, B.; Yang, M.; An, B.; Onses, M. S.; Rogers, J. A.; Kaplan, D. L.; Omenetto, F. G. Inkjet Printing of Regenerated Silk Fibroin: From Printable Forms to Printable Functions. *Adv. Mater.* **2015**, *27*, 4273–4279.

(10) Wang, D.-E.; Wang, Y.; Tian, C.; Zhang, L.; Han, X.; Tu, Q.; Yuan, M.; Chen, S.; Wang, J. Polydiacetylene Liposome-Encapsulated Alginate Hydrogel Beads for Pb 2+ Detection with Enhanced Sensitivity. *J. Mater. Chem. A* **2015**, *3*, 21690–21698.